Distinct neurogenic pathways shape the diversification and mosaic organization of cortical output channels

Shreyas M. Suryanarayana[1,5], Xu An[1,5], Yongjun Qian[1,2], Shengli Zhao[1], Hemanth Mohan[1,3], Z. Josh Huang[1,4*]

[1] Department of Neurobiology, Duke University Medical Center, Durham, NC, USA

[2] Current affiliation: College of Future technology, Peking-Tsinghua Center for Life Sciences, IDG/McGovern Institute for Brain Research, Beijing Advanced Center of RNA Biology, Peking University, China

[3] Current affiliation:Department of Neurobiology and Anatomy, McGovern Medical School at UTHealth Houston, Texas, USA

[4] Department of Biomedical Engineering, Durham, NC, USA

[5] Co-first Authors

*Correspondence: josh.huang@duke.edu;shreyas.suryanarayana@duke.edu;

Summary

The cerebral cortex broadcasts its output to subcortical regions through the projections of diverse extratelencephalic neurons (ETs) derived from either direct (dNG-ET^d) or indirect (iNG-ET^i) neurogenesis, but the differential contributions of these neurogenic pathways to cortical output organization remain unknown. Establishing a lineage-based viral targeting strategy in mice, we uncover that ET^i massively amplifies and diversifies ET^d projections across the cortex. Whereas ET^d primarily targets the forebrain and midbrain, ET^i dominates the hindbrain (e.g., brainstem/spinal action centers, lemniscal sensory stations), hypothalamic, and neuromodulatory regions with cortical area-specific projections. Numerous corticofugal subpopulations derive solely from iNG-ET^i. Area-specific spinal projections of ET^i but not ET^d emerge from the postnatal pruning of an initial cortex-wide population. In the motor cortex, ET^d or ET^i activation induced distinct movements: either head-trunk, or additionally, coordinated orofacial-forelimb movements, respectively. Thus, two foundational neurogenic pathways with distinct evolutionary history differentially shape the area-specific diversification of cortical output channels.

Introduction

The cerebral cortex is the crowning achievement of vertebrate evolution and contains a vast network of nerve cells underlying high-level brain functions from sensory processing to cognition and motor control [1–4]. Glutamatergic projection neurons (PN) constitute up to 80% of cortical neurons and comprise several major classes characterized by their laminar location, projection patterns, and gene expression profiles [5–7]. Whereas the intratelencephalic (IT) neurons project within the cerebral hemisphere and mediate intra-cortical processing streams, the extratelencephalic (ET) neurons constitute a massive and area specific efferent system that broadcast cortical output to myriad subcortical regions throughout the central nervous system [6,8–10]. Decades of studies have uncovered daunting diversity in ET projection patterns within and across cortical areas and across mammalian species [10–15]. Nevertheless, the same diverse set of ET neurons are reliably generated in each animal to carry out species-typic behavioral functions, suggesting a robust and stringent developmental genetic program. However, the development origins and processes that shape ET projection diversity and their area specific profiles remain poorly understood.

All PNs, including ETs, are generated from radial glia progenitors (RG) lining the embryonic cerebral ventricle through two fundamental forms of neurogenesis. In direct neurogenesis (dNG), a RG undergoes asymmetric division to self-renew and generate one neuronal progeny[4,16,17]; in indirect neurogenesis (iNG), RG first produces an intermediate progenitor (IP), which then undergoes symmetric division to generate two neurons[18–24]. Across the developing mammalian neural tube, dNG is ubiquitous from spinal segments to the forebrain and contributes to the development of the entire central nervous system, while iNG is largely restricted to the telencephalon that gives rise to the cerebral hemisphere[18,25]. Across vertebrate evolution, while dNG originated before the dawn of vertebrates and has been conserved ever since, iNG emerged largely since amniotes (but see [26,27]) and has expanded tremendously in mammals, and is thought to drive the evolutionary innovation of a 6-layered isocortex[20,23,25,28,29]. While the amplification of neuronal production through IP is inherent to iNG, whether and how dNG and iNG differentially contribute to the diversification and organization of ET-mediated cortical output channels is unclear.

Using a genetic strategy to distinguish and fate map dNG and iNG, we previously found that whereas dNG generates all major PN classes, iNG differentially amplifies and diversifies PNs within each class [17]. In particular, dNG and iNG generate ET^d and ET^i, respectively, which are completely intermixed in layers 5 and 6 and appear indistinguishable in gross somato-dendritic morphology[17,30]. However, whether ET^d and ET^i differ in axon projection patterns - a crucial determinant of their connectivity and circuit function, remains unknown.

Here, we first establish a novel lineage-based genetic method that enables differential viral targeting of ET^d and ET^i in the same individual mice. Through systematic antero- and retrograde tracing, we show that iNG-ET^i massively amplifies and diversifies the dNG-ET^d projections across the cortex. While ET^d projections are largely restricted to forebrain and midbrain structures, ET^i neurons greatly amplify and diversify these projections and overwhelmingly dominate the innervation of hindbrain and spinal cord in an area-specific pattern. In particular, ETs^i in motor areas dominate projections to brainstem and spinal action diversification and execution centers, in sensory areas expand projections to sensory processing stations along lemniscal pathways, in higher order areas extend projections to other pallial structures and to hypothalamic and neuromodulatory centers. Corticofugal subpopulations in multiple areas are

derived from only ET^i but not ET^d, indicating the generation of novel projection types by iNG. During an early postnatal period, ET^i but not ET^d neurons across the cortex undergo exuberant axon overgrowth to the spinal cord followed by massive pruning, sculpting areal-specific spinal projections seen in mature cortex. Optogenetic activation reveals functional distinction between ET^d and ET^i in the motor cortex: while the formal induced movements of head and trunk, the latter additionally elicited coordinated orofacial and forelimb movements that resemble feeding. Together, these results demonstrate that two foundational neurogenic pathways with distinct evolutionary history prime the area-specific diversification and mosaic organization of cortical output channels that shape the central nervous system architecture.

Results

A genetic strategy enabling differential viral access to ET^d and ET^i in the same animal

To fully uncover the anatomical distinctions between ET^d and ET^i, we designed a novel genetic strategy that allows for differential viral targeting of these two subpopulations based on their lineage distinction that resolves a common molecular marker (**Figure 1A**). The zinc finger transcription factor *Fezf2* is broadly expressed in the majority of postmitotic ETs including both ET^d and ET^i [17,31,32], yet the T-box transcription factor *Tbr2* is selectively expressed in embryonic IPs that generate all PN^i, including ET^i but not ET^d [17]. Thus, we built a *FezF2-tTA-CreER (FezF2-TC)* knockin allele driving the conditional expression of two tandemly arranged cassettes: a tTA cassette flanked by Frt sequences followed by a CreER cassette (**Figure 1A**). We confirmed that *FezF2-TC* reliably captures endogenous *FezF2* expression pattern by *in situ* detection of *FezF2* mRNA in labelled ET neurons (**Figure S1A-C**). When combined with a *Tbr2-Flp* knockin allele [17], dNG-derived ETs^d, which do not express *Tbr2-Flp* during development, constitutively express tTA but not CreER; on the other hand, iNG and IP-derived ETs^i, in which developmental expression of *Tbr2-Flp* removes the tTA cassette, constitutively express CreER (**Figure 1A**). Thus, this genetic strategy converts developmentally transient lineage signals in neurogenesis to permanent “genetic handles” that allow differential viral targeting of postmitotic ET^d and ET^i neurons in the same individual mice.

Indeed, retro-orbital co-injection of tTA-driven *AAV-TRE-GFP* and Cre-driven *AAV-FLEX-RFP* in *FezF2-TC;Tbr2-Flp* double transgenic mice resulted in reliable differential labeling of ETs^d and ETs^i respectively, across the cortex (**Figure 1B**). As negative controls, we verified that *AAV-FLEX-RFP* showed no leaky expression in the cortex (**Figure S1H-I**), and *AAV-TRE-GFP* showed minimal leaky expression that was restricted to somatic but not axonal labelling, even after immunofluorescence amplification (**Figure S1D-G**).

To further validate our strategy, we compared the numbers and relative ratios of AAV-based ET^d and ET^i labeling with those of a previously validated intersection-subtraction reporter allele (IS)-based labeling [17]. *AAV-TRE-GFP* and *AAV-FLEX-RFP* co-injection in motor, barrel, and visual cortex in *FezF2-TC;Tbr2Flp* mice yielded very similar labeling of ET^d and ET^i (**Figure 1C-C3**) in equivalent areas in *FezF2-CreER;Tbr2-Flp;IS2* mice (**Figure S1J-M**). In both approaches, the number of ET^i neurons was significantly more than ET^d for motor and barrel cortices (**Figure 1K-L**), and there was no significant difference for the visual cortex although there were more ET^i neurons (**Figure 1M**). Although viral labeling captured greater number of ET^d and ET^i neurons in *FezF2-TC;Tbr2Flp* as compared to the IS2 reporter strategy, likely due to higher sensitivity of AAV labelling, there were no significant

differences in their proportion, which ranged from 20-30% for ET^d (mean: 24.5%) and 70-80%for ET^i (mean:75.5%) for all three areas from either approach (**Figure S1N-N2**). Thus, ETs^d and ETs^i are generated across different cortical areas with an overall ratio of approximately 1:3, indicating differential amplification by iNG. Together, these results validate our novel strategy for differential AAV targeting of ET^d and ET^i in the same animal.

Amplification, diversification and innovation of ET projection types by iNG

While ETs^d and ETs^i are distributed across different regions of the isocortex[17], whether and how they differ in their projection targets is unknown. We first addressed this question by retrograde labelling from four subcortical targets – the superior colliculus (SC), pontine nuclei (PONS), medulla (Med) and the spinal cord (SpC) (**Figure 2A-D**). Given that the two retro-AAVs (*AAV-TRE-RFP* and *AAV-FLEX-GFP* that label ET^d and ET^i, respectively) are co-injected in the same location of the same animal, this method allows us to compare the distribution and relative proportion of ET^d and ET^i across the isocortex. Brains were analyzed by both confocal (n = 2, each target area, **Figure 2E-H**) and lightsheet microscopy (n = 2-3 each target area, **Figure 2A-D**, **S2E**, **Video S1-S4**). Indeed, retroAAV injections from the 4 target sites labeled intermixed layer 5 ET^d and ET^i that were distributed across the isocortex (**Figure 2A-D**, **S2A-D**).

Considering the overall proportions of ET^i and ET^d neurons across isocortex, the amplification of ET^i cell number over ET^d is approximately 3:1 (**Figure S1N-N2**). If ET^i and ET^d neurons broadly project to the same sets of subcortical targets, we would broadly expect a similar degree of 3:1 *amplification* of ET^i over ET^d projection at these targets. However, retrograde labeling revealed a substantially disproportionate increase in L5 ET^i over ET^d proportion from all four injection sites (**Figure 2I-L**): the ET^i/ ET^d ratio ranged from 12.5:1 for collicular-projecting, 25:1 for pontine-projecting, 33:1 for medullary-projecting, to 40:1 for spinal-projecting neurons. As each ET neuron often projects to different combinations of these targets, this result indicates a substantial *diversification* of projection patterns for ET^i over $ET^{d,}$, especially those to the more distal targets assessed. Moreover, while both ET^i and ET^d neurons were mostly co-labeled and intermixed across areas, though at different ratios, by colliculus injection, there were multiple areas (e.g., SSp-n, AUDpo, ORBv, ILA) where only ET^i but not ET^d neurons were labeled by injection to the PONS, Med, and SpC (**Figure 2M-O**). This result indicates the presence of novel distally-projecting ET types in these areas generated only through iNG, which we consider as *innovation* by iNG (**Figure 2P**). Notably, these novel area-specific ET^i projection types were largely found in sensory and higher order areas rather than motor areas (**Figure 2M-O**). This result suggests that in addition to the diversification of ET projection types from the frontal and motor areas, iNG generates novel projection types in some non-motor areas that grant them direct access to the motor centers and other areas in the PONS, Med and SpC.

Although the 4 injection sites represent only a small subset of ET targets, the results together demonstrate that, compared with dNG, iNG not only amplifies but also diversifies projection classes, and additionally generates novel ET projection types. To reveal the precise and comprehensive projection patterns of ET^d and ET^i in specific areas, we then carried out a set of anterograde labeling across eight isocortical areas encompassing motor, sensory, and higher order areas.

ET^i in motor areas expands projections to action diversification and execution circuits

For the motor areas, we chose the rostral forelimb orofacial area (RFO [33]) and the caudal forelimb area (CFA[11,34–36]) in the primary motor cortex (MOp) and an area in the secondary motor cortex (MOs) recently implicated in a forelimb-reach-to-grasp behavior (RGD) [37](**Figure 3A-C**, **S3A, S4A, S5A**). In all three areas, *AAV-TRE-GFP* and *AAV-FLEX-RFP* labelled ET^d and ET^i in deep layers, with approximately 1:3 ratio (**Figure S3A1-A2, S4A1-A2, S5A1-A2**). Our goal here is to quantitatively compare the relative strength of ET^i and ET^d projections across major subcortical targets. While confocal microscopy gave high resolution view of subsets of targets (n = 2 for each area, **Figures S3A-G, S4A-G, S5A-G**), light-sheet microscopy enabled us to capture the entire projections to all targets in the whole brain (n = 2 for each area, **Figure 2A-C, S3I, S4I, S5I, Video S5-S7**). We generated 3D renderings of projections and fraction occupation heatmaps for all downstream targets (listed in **Table S1**) for the 3 injection areas (**Figure 3A-C, 3D-F**).

To quantify the relative projection strength of ET^i and ET^d using light-sheet microscopy datasets, we measured the percent occupancy in selected target structures using ET^d or ET^i axon fluorescence signals. This measurement is not in terms of fluorescence intensity, which is not directly comparable between tdTomato (ET^i) and GFP (ET^d), and could be an underestimate of ET^i projection strength. An equivalent ratio of ET^i over ET^d projection strength to that of their cell body ratio at injection site (e.g., 3:1) would suggest a simple amplification by ET^i. On the other hand, a disproportional increase of ET^i proportions at different target regions would suggest a diversification or innovation of ET^i projections. Thus, in addition to assessing the relative increase of ET^i over ET^d projections at each target, we compared them across different target regions of interest and ran post-hoc comparisons between these regions with the thalamus to reveal specific target regions with a disproportional increase of ET^i projections. The thalamus was chosen for comparison as a forebrain region which receives substantial ET^d as well as ET^i projections.

While both ET^d and ET^i targeted the thalamus (**Figure S3B, S4B, S5B**), ET^i had significantly more projections from all three areas (**Figure S3B1-B3, S4B1-B3, S5B1-B3**). Notably, *FezF2* expressing ET neurons include both PT (pyramidal-tract like, mostly in L5b but also L6) and some CT (cortico-thalamic in L6) populations; thus, the labeled thalamic projections derive from both populations (See Discussion, **Figure S3B, S4B, S5B**).

As a broad category, projections to the brainstem areas (i.e. PT type projections that include MB, PONS, Med, SpC) from all three motor areas were significantly amplified in ET^i over ET^d (**Figure S3B1-B3, S4B1-B3, S5B1-B3**). Within the thalamus, the three motor areas showed differences in ET^d vs ET^i projection to first order (FO) and higher order (HO) nuclei. RFO and MOs had similar ET^d and ET^i projections to FO but more ET^i projections to HO (**Figure S3C1-C3, S5C1-C3**). CFA had stronger ET^i projections to both FO and HO (**Figure S4C1-C3**).

At the level of basal ganglia (BG), ET^i had a major enhancement of projections over ET^d to all BG nuclei from all three areas (**Figure S3D1-D3, S4D1-D3, S5D1-D3, Figure 3G-I**) indicating vastly expanded control by ET^i over action selection circuits [38,39].

In the MB, ET^i had significantly more projections than ET^d from all three areas (**Figure S3E1-E3, S4E1-E3, S5E1-E3**); this was also true for projections to the PONS and Med (**Figure S3F1-F3, S3G1-G3, S4F1-F3, S4G1-G3, S5F1-F3, S5G1-G3)**. When the relative increase of ET^i over ET^d was compared across target regions, there were significant differences (p value for RFO:$p < 0.05$; CFA:$p < 0.0001$; MOs:$p < 0.01$, Kruskal–Wallis test). Post-hoc comparisons revealed that for all three areas, increase of ET^i over ET^d to the Med and BG and additionally to PONS were more pronounced compared to that in

thalamus (**Figure S3H, S4H, S5H**). This result suggests that Med-projecting ET from RFO and PONS- and Med- projecting ET from the CFA and MOs are largely generated by iNG.

Thus, across motor areas, while both ET^d and ET^i target forebrain and midbrain areas, the bulk of corticofugal projections to more distal targets are predominantly generated by iNG-ET^i to innervate action selection, diversification and execution centers in the BG, hindbrain and SpC, (**Figure 3G-I**). This expansion by iNG-ET^i thus creates the anatomical substrate for monosynaptic control of motor centers in the BS and SpC by motor areas of the isocortex.

ET^i in sensory areas expands subcortical projections to ascending sensory pathways

We targeted three sensory areas for anterograde tracing – the visual cortex (VIS), auditory cortex (AUD) and barrel cortex (BAR) (n=2 [confocal, **Figure S6A-E, S7A-G, S8A-G**], n = 2 [lightsheet, **Figure S6G, S7I, S8I, Video S8-S10**] for each area, **Figure 4A-C *top*, S6A, S7A, S8A**). The VIS injection labelled neurons in layers 5 and 6 with more ET^i (**Figure S6A1-A2, S7A1-A2, S8A1-A2**). In AUD and BAR areas, there were more ET^i labelled in layer 5; while in layer 6a/6b, more ET^d or near equal numbers of ET^d and ET^i were labelled (**Figure S7A1-A2, S8A1-A2**). The larger number of ET^d in layer 6a/6b are likely CT neurons, which are mostly derived from dNG[17]. We generated 3D renderings of projections and heatmaps for all three injection areas (**Figure 4A-C, 4D-F**).

From VIS and AUD, there was significantly more ET^i than ET^d projections to both the thalamus and brainstem areas (**Figure S6B1-B3, S7B1-B3, S8B1-B3**). Within the thalamus, there was no significant difference between ET^d and ET^i projections to FO while ET^i had significantly more projections to HO (**Figure S6C1-C3, S7C1-C3, S8C1-C3**). The dense projections of ET^d to FO may include a significant CT component while those of ET^i to both FO and HO could largely derive from PT.

For AUD and BAR areas, we compared ET projections to major sensory processing stations along their respective ascending lemniscal pathways. ET^i but not ET^d heavily targeted lemniscal centers, suggesting that iNG confers sensory cortical access to lemniscal sensory processing centers (**Figure S7D1-D3, S8D1-D3**).

When examining VIS corticofugal projections, we noticed that in some prethalamic nuclei such as the ventral lateral geniculate (LGv), the ET projections were almost entirely ET^i (**Figure S6C**). Notably, LGv is expanded in nocturnal mammals such as rodents and is similar in size to the LGd [40].

Regarding ET projections to the MB, projections from all three areas were dominated by ET^i (**Figure S6D1-D3, S7E1-E3, S8E1-E3**). There were generally more ET^i than ET^d projections to PONS and Med (**Figure S6E1-E3, S7F1-F3, S8G1-G3, S8F1-F3, S8G1-G3**). Notably, the relative increase of ET^i over ET^d for VIS was not different between target regions indicating a similar increase of ET^i projections across subcortical structures (**Figure S6F**). In contrast, the increase of ET^i over ET^d from AUD for the lemniscal centers and PONS was larger than that in the thalamus (**Figure S7H**); this was true across the BS for BAR (**Figure S8H**).

Thus, in sensory areas, iNG-ET^i elaborates projections to HO thalamus, prethalamus and sensory lemniscal centers, while also incorporating motor like features to BAR with elaborated projections to hindbrain. In contrast, ET^d heavily targets FO thalamus, with projections also to the midbrain and weak projections to lemniscal centers, PONS and Med (**Figure 4G-I**).

ET^i in higher order areas diversifies projections to pallial, hypothalamic and neuromodulatory structures

We further compared ET^i and ET^d projections in two higher order areas of the isocortex, the prefrontal (PFC) and posterior parietal areas (PAR) (n=2 for confocal, [**Figure S9A-J, S10A-G**], n = 2 for Lightsheet, **Figure 5A-B, S9L,S10I,Video S11-S12**] for each area**.** The injection at each area labelled neurons with more ET^i than ET^d (**Figure S9A-A2, S10A-A2**).

From the PFC, both ET^i and ET^d targeted the thalamus heavily while there were stronger ET^i projections over ET^d to the brainstem regions (**Figure S9B1-B3**). In contrast, from PAR,there were more ET^i projections over ET^d to both thalamus and BS, similar to what was observed in motor areas (**Figure S10B1-B3**). This result suggests higher numbers of PT neurons in PAR sending collaterals to thalamus.

Comparing projections to FO and HO thalamus, from PFC ET^d had stronger projection to FO than ET^i, while ET^i had stronger projection to HO. From PAR, ET^i had stronger projections to both FO and HO (**Figure S9C1-C3, S10C1-C3**). The PAR projections to FO and HO were similar to proportions of ET^i and ET^d projections from motor areas (**Figure S10C1-C3**). Given this similarity and since the PAR is known to have roles in motor behavior[41,42], we further examined BG and found again that the projections were predominantly ET^i **(Figure S10D-D3)**.

The PFC is known to target multiple non-isocortical pallial areas [43]. We found that the majority of these projections were ET^i (**Figure S9D1-D3**), suggesting a massive elaboration of inter-pallial interaction by iNG- ET^i. Some other forebrain areas like the epithalamus received similar PFC ET^d and ET^i projections (**Figure S9E1-E3**). Notably, ET^i projections dominated the hypothalamus (**Figure S9F1-F3**). This highlights selective expansion of projections by distinct neurogenic pathways in anatomically/developmentally close and related structures.

Another important observation was the heavy ET^i over ET^d projections to different neuromodulatory centers across the brain from PFC (**Figure S9G1-G3**), indicating the expansion of higher order cortical control of neuromodulation. PFC and PAR projections to the MB and PONS were largely ET^i (**Figure S9H-H3, S9I-I3, S10J-J3, S10E-E3, S10F-F3, S10G-G3**).

Taken together and considering the relative increase of ET^i over ET^d among different target regions and the thalamus, ET^i in higher order areas selectively expands projections to neuromodulatory centers, hypothalamus and also dominates interactions with other pallial areas while incorporating motor area like features with significant expansions to hindbrain and SpC (**Figure S9K, S10H, Figure 5E-F**).

Selective axon pruning in ET^i but not ET^d during early postnatal development shapes the areal distribution of ET^i

The area specific ET projection patterns to multiple subcortical regions are established by a multi-step developmental process that involves progressive (axon guidance, synapse formation) as well as regressive (axon pruning, synapse elimination) events [44,45]. In particular, axon pruning has been demonstrated for corticofugal neurons from multiple cortical areas during early postnatal period [46], with a prominent role in shaping the arealization of descending pathways [47]. We therefore examined whether axon pruning may differentially sculpt the projection patterns and arealization of ET^d and ET^i. As substantial pruning of mouse corticospinal axons occurs during the first postnatal week, we injected

retroAAVs in the cervical spinal cord (cSpC) of P4 mice and examined cortex-wide ET^d and ET^i labelling pattern at P40 (P4-P40), and compared it with those labeled from adult (P28) cSpC injection (P28-P40) (n = 2, confocal, **Figure 6C-D**; n = 2, lightsheet, **Figure 6A-B, S11D, Video S13**).

In contrast to the P28-P40 ET labeling pattern that is highly restricted to a few areas (MOp, MOs, SSp, **Figure 6E**), P4 cSpC injection labeled a significantly larger number of ET neurons across the anterior-posterior extent of cortex (**Figure 6F**), consistent with previous findings[47,46]. Strikingly, this vast expansion of P4-P40 ET labeling consisted of almost exclusively ET^i (**Figure 6G-I**). In contrast, P4-P40 labeled a small number of ET^d neurons that remained restricted to the same few areas as those in P28-P40 labeling (**Figure 6E-I**). This result suggests that across the early postnatal cortex, ET^i, but not ET^d, initially undergo exuberant axon growth to the spinal cord; and the massive cortex-wide pruning of ET neuron axons that sculpts their subsequent areal specific patterns is restricted to ET^i. In contrast, most ET^d neurons across the developing cortex do not project to the spinal cord, and the mature pattern of ET^d-spinal projection in specific areas (e.g. MOp, MOs and SSp) is likely achieved by area-specific properties of axon growth and guidance.

Notably, ET neurons reside in both L5 and L6, and many L6 ET neurons project to more proximal subcortical targets than the spinal cord. In this context, we found that P4 cSpC injection labeled many L6 ET^i but not ET^d in MOs and SSs (**Figure 6J-K**). This result suggests that the corticofugal projection pattern of L6 ET^i, but not ET^d, is also shaped by the pruning of their axon arbors that initially reached the spinal cord.

Surprisingly, we found that P4 cSpC injection further labeled iNG- but not dNG-derived neurons in many pallial areas outside of the isocortex (**Figure S11A-C, S11E-G**). The largest number were found in the hippocampal formation (**Figure S11C, S11E**) but also in other regions including piriform cortex (**Figure S11A**) and amygdala (**Figure S11B**). As controls, cSpC injection at P1, when ET axons have not reached the spinal cord, resulted in very sparse labelling of ET^d and ET^i in cortical structures at P40 (n = 2, **Figure S11G**). Further, sSpC injection of a generic retro-AAV into wild type mice at P6 labeled neurons in both the isocortex and other pallial areas, confirming our results using *FezF2TCTbr2Flp* mice and Cre and tTA dependent retro-AAvs (n = 2, **Figure S11I**). All together, these results suggest that an initial exuberant axon growth, many reaching the SpC, followed by extensive axon pruning, is a general feature of ET^i but not ET^d across the pallial/cortical structures to establish their areal specific subcortical projection patterns.

Functional distinctions of ET^d and ET^i in the motor cortex

To uncover the functional significance of the projection differences between ET^d and ET^i, we carried out differential optogenetic stimulation of ET^d and ET^i in the same animal in head-fixed as well as free-moving conditions using *the FezF2-TC-Tbr2 mice* (**Figure 7A,7C,7J-J3**). We injected *AAV-TRE-ChRmine-oScarlet* on the left RFO and *AAV-FLEX-ChRmine-oScarlet* on the right RFO (**Figure 7C**). The injections robustly captured ET^d and ET^i (**Figure 7C**) which could be optogenetically activated sequentially in the same mouse. As a control, we also performed similar activation of all ET neurons (ET^{all}) using *FezF2-CreER;Ai32* mice[33,48] (**Figure 7B)**.

In the rostral forelimb-orofacial area (RFO), activation of ET^{all} in the head-fixed condition induces contralateral forelimb adduction to the body midline with hand supination and digit closing and jaw opening (**Figure 7D-I; Video S14;** also see[34]). Strikingly, sequential optogenetic activation of ET^d and

ET^i in the left and right RFO in head-fixed condition induced highly distinct movements. Whereas ET^d activation induced only minor or no oral movement and no forelimb movements (**Figure 7D-I**; **Video S14; ET^d:n = 4)**, ET^i activation induced prominent and coordinated forelimb and oral movements (**Figure 7D-I**; **Video S14; ET^i: n = 6**). These movements elicited upon ET^i activation resembled that of ET^{all} activation (**Figure 7D-I; Video S14; ET^{all}:n = 6**)

In the free-moving condition, ET^{all} activation in the RFO induced movements which involve a shoulder adduction that raises the contralateral hand toward the body midline with associated hand supination and digit flexion. In addition, a concurrent ipsiversive head turning and lowering, and bringing the snout toward the raised hand is induced (**Figure 7J-J3; Video S14;ET^{all}:n = 4;** also see[34]). These movements resemble ethological feeding behaviour[33]. Interestingly, ET^d stimulation in RFO induced head lowering and associated body/trunk movement but with no forelimb movement. In sharp contrast, RFO ET^i stimulation induced the fully coordinated head-to-hand as well as hand-to-mouth movements that are similar to those induced by ET^{all} stimulation and resemble ethological feeding **(Figure 7J-M; Video S14;ET^d:n = 5;ET^i: n = 5)**.

Together, these results suggest that ET^d mainly regulate midline axis movements involving proximal body parts such as head, trunk consistent with their projection targets, while ET^i additionally and directly control distal body parts such as the forelimb and hand, thereby coordinating complex and dexterous movements. These data thus show that ET^i amplify and diversify ET^d motor cortex functions, consistent with their projection differences to brainstem and spinal to action diversification and execution circuits that mediate oral-manual movements.

Discussion

The mammalian cerebral cortex contains a vast neural network comprising dozens of functional areas, which together integrate sensory information with cognitive and internal state signals to orchestrate behavior. The computational outcome of the cortex is broadcast to multiple subcortical regions by diverse subpopulations of ET neurons across different cortical areas. Decades of studies demonstrate that ET projection patterns vary substantially within as well as across cortical areas and across mammalian species [5,8–10,49,50]. It has remained an enigma whether this daunting and seemingly unresolvable heterogeneity is stochastic, reflects a continuum, or can be meaningfully classified into ground truth subpopulations relevant to the developmental process and systems level organization and function. Here we dissect the diversity and organization of ET neurons based on a fundamental distinction in their developmental origin – dNG and iNG, which differ not only in progenitor types (RG vs IP) and cell division patterns (asymmetric vs symmetric) but also in evolutionary history. A key experimental entry point is our design of a genetic strategy that converts developmentally transient lineage signals in neurogenesis to permanent “genetic handles” that allow differential viral targeting of postmitotic ET^d and ET^i in the same individual mice. We found that ET^d projections are largely restricted to forebrain and midbrain structures, while ET^i differentially amplifies and diversifies these projections in an area-specific way across brain systems, and overwhelmingly dominates the innervation of hindbrain and spinal cord (**Figure 8**). Notably, corticofugal subpopulations in multiple areas are derived from only ET^i but not ET^d, indicating the generation of novel projection types by iNG. Furthermore, areal-specific ET^i, but not ET^d, spinal projection pattern is sculpted from the exuberant overgrowth and subsequent massive pruning of an initial cortex-wide population during early postnatal period. Consistent with their differences in projection patterns, optogenetic activation of ET^d and ET^i in the motor cortex reveal corresponding functional distinctions: while ET^d induced movements of head and trunk, ET^i additionally

elicited coordinated orofacial and forelimb movements that resemble feeding. Together, these results uncover that two foundational neurogenic pathways with distinct evolutionary history differentially shape the area-specific organization and functional diversification of cortical output channels (**Figure 8**).

A developmental and evolutionary (i.e. evo-devo) perspective is uniquely powerful in interpreting and understanding the stark differences between ET^d and ET^i projection patterns and provides deep insights into the basic organization of the cortical output system. In early vertebrates, the ancient pallium already evolved a blueprint of projections to downstream motor centers [51], with several cardinal cell types [52] and basic connectivity[53], but the overall behavioral repertoire was limited and the involvement of pallium in motor control was rudimentary [1,54]. Motor centers in the midbrain tectum (superior colliculus) [55], tegmentum and the well conserved BG in the forebrain [56], played key roles in motor control and behavior (**Figure 8**) [57]. With the emergence of amniotes (reptiles and mammals), the "higher order" orchestration of motor control has gradually shifted to the cortical pallium [58,59], culminating in the mammalian isocortex. In parallel, with the evolution of limbs, hands and digits, command centers for specialized movements have expanded in the midbrain, BS, and SpC [60–62]. The mammalian isocortex in particular, has seen a massive elaboration of efferent projections, which grant increasing monosynaptic control of downstream motor centers including the SpC [8,31]. Importantly, this momentous "shift" of high-level motor control to the isocortex is mediated by the vastly expanded and diversified ET corticofugal projections and is correlated with the evolutionary expansion of iNG (**Figure 8**). While the amplification of neuronal production to expand cortical size is inherent to iNG, a major question is whether and how dNG and iNG differentially contribute to the diversification and organization of neuron types, in particular ET neurons that mediate cortical output channels driving behavior. Our basic premise is that the mouse dNG-ET^d reflects the mammalian instantiation of the evolutionarily more ancient system that has been conserved (albeit updated) across vertebrates, while iNG-ET^i represents the mammalian expansion and innovation.

Across different cortical areas and functional systems, ET^d and ET^i projections from the motor areas present strong interpretations for their functional distinction in the context of motor control systems [1,63,64]. In particular, the rostral forelimb orofacial area (RFO) coordinates orofacial and forelimb actions in food manipulation, in part via ET neurons [33,36,41,65,66]. Consistent with the subcortical projection differences between RFO ET^d (to mostly forebrain and midbrain regions) and ET^i (additionally to brainstem and spinal cord; **Figure 3G**), optogenetic activation reveals corresponding functional distinctions: while ET^d induced restricted movements of head and trunk, ET^i additionally elicited coordinated orofacial and forelimb movements that resemble feeding. iNG-ET^i thus not only amplifies ET^d cell numbers but also diversifies functional ET types, enabling coordinated multi-effector movements likely through recruitment of multiple action diversification/execution centers in the brainstem/spinal cord. It is plausible that ET^d might represent the conserved pan-vertebrate pathway that mainly targets the midbrain superior colliculus to regulate midline axis head-body orienting movements, and ET^i might encapsulate the mammalian isocortical innovation that expands to the BS and SpC to control and coordinate multi-effector forelimb-orofacial movement. Consistent with our finding, there is a direct correlation of improved forelimb dexterity with the expansion of the corticospinal neurons even between closely related rodent species[67]. In addition to brainstem and SpC, we further reveal strong ET^i over ET^d projection from motor areas (e.g. RFO, CFA, MOs) to all BG nuclei beyond the striatum, including GPe [68] and output nuclei [69] (**Figure 3G-I**) which may enhance cortical modulation of BG circuits during motor learning [70] and action selection[39,71].

Sensory areas also show substantially expanded ET^i projections over ET^d. The barrel cortex exhibits both strong CT (ET^d) projection to FO and extensive PT (ET^i) projections to HO, BS, and SpC. As a rodent-specific sensorimotor area [72], barrel cortex may exemplify the evolution of hybrid output pathways via iNG- ET^i , consistent with isocortical expansion of sensory areas, [3,73,74]. Notably, the primary visual cortex shows strong ET^i and minimal ET^d projections to the GABAergic prethalamic nuclei like vLGN, which is expanded in nocturnal mammals [40] and mediates innate visual behaviors such as fear responses[75,76]. Input to vLGN from visual cortical areas can suppress such responses [77], suggesting that iNG-ET^i diversification might enable the cortex to modulate instinctive behaviors through learning. iNG-ET^i expansion in sensory areas also targets the lemniscal pathways, such as principal trigeminal nucleus (barrelettes, [78] and VPM (barreloids, [79]) targeted by barrel cortex, and the superior olive (sound localization, [80]) and inferior colliculus (acoustic-motor functions[81]) targeted by auditory cortex. These ET^i projections may confer cortical modulation of ascending sensory processing at multiple levels.

In higher-order areas, the parietal cortex supports decision-making and movement planning [41,82,83], and shows expanded ET^i output to BG, BS, and SpC. PFC, the most recently evolved isocortical area that supports cognitive control [84], shows elaborate ET^i but few ET^d projections to pallial targets like BLA and hippocampus, structures critical for social behavior and memory [85–88], and to neuromodulatory centers like the VTA and dorsal raphe which can influence reward and behavioral states [89]. PFC ET^i projections to the hypothalamus might confer cortical regulation of homeostatic and defensive behaviors[99,100].

Altogether, our results reveal the systematic distinctions and mosaic organization of dNG-ET^d and iNG-ET^i projection streams across the isocortex. They suggest that the evolutionary expansion and diversification of iNG-ET^i may contribute to the expansion, diversification, and functional specialization of numerous isocortical areas through their massive and areal-differentiated corticofugal projections, which further shape the rest of the central nervous system architecture (**Figure 8**).

The area-specific ET projection patterns are likely shaped by the interplay of two broad classes of developmental mechanisms involving progressive as well as regressive processes. While genetic programs for targeted axon growth and guidance are well-suited to specify a species-invariant projection scaffold, regressive axon pruning allows for refinement of initially more exuberant branches, possibly in an activity- and utility-dependent manner to sculpt functional connections [44]. Indeed, axon pruning has been implicated in the development of ET projection patterns [46]. ET neurons across broad cortical areas initially all extend their axons distally to the spinal cord, then undergo massive axon pruning to sculpt their subcortical projection patterns and area specific distribution [47,46,47]. A recent study examined axonal pruning of two broad ET subpopulations: ET_{dist} that predominate in the motor cortex and project distally to the pons, medulla and SpC, and ET_{prox} that predominate in visual cortex and project more proximally to pons and thalamus [12,47]. Whereas subsets of ET_{prox} emerge from pruning of their initially distal-projection axons, others emerge through targeted growth. Here, we found that during the first postnatal week, ET^i neurons across the developing cortex undergo exuberant axon overgrowth to the spinal cord, followed by massive pruning to achieve areal specific distribution patterns in mature cortex. In sharp contrast, most developing ET^d across the cortex do not extend axons to the spinal cord, with the exception of a small subset largely restricted to motor areas. Notably, within the developing secondary motor and somatosensory areas, L6 in addition to L5 ET^i axons also project to the SpC, which are subsequently pruned (Figure 6C,D). Furthermore, beyond the isocortex, broadly defined Fezf2-expressing ET^i but not ET^d neurons in other cortical structures (e.g. hippocampus, BLA, entorhinal cortex, etc) also initially project to SpC and then undergo pruning.

Although we cannot rule out the possibility that a subset of ET^d neurons that project to more proximal targets also undergo pruning, our results indicate that exuberant axon growth followed by extensive pruning is a general and key feature that distinguish ET^i from ET^d. It is plausible that substantial axon pruning is an effective mechanism to sculpt species-typic as well as individually customized ET projection patterns in each animal, in part through use- and activity-dependent mechanisms.

Beyond axon projection patterns, our reliable experimental access to dNG-ET^d and iNG-ET^i will enable multi-faceted analysis of these developmental genetic-defined subpopulations. Future studies will trace their synaptic input patterns, record and manipulate their activity during behavior, and reveal their gene expression profiles and regulatory programs. These studies will integrate the developmental genetic and systems neuroscience approaches toward understanding the diversity and organization of cortical neuron types in the context of vertebrate evolution.

Major unresolved questions include the evolutionary origin(s) of indirect neurogenesis and its massive expansion along the mammalian clade, including the underlying molecular genetic mechanisms that regulate the balance between dNG and iNG. Contrasting the previously held view of an amniote origin[28,90], recent studies provide evidence for a more ancient evolution of iNG dating back to amphibians and even earlier to jawed vertebrates[26,27]. A previous study shows that the balance between dNG and iNG in the dorsal pallium is regulated by the activity levels of a conserved Robo/Slit and Notch/Delta-like 1 (Dll1) signaling across several amniote species[90]. Notably, comparative transcriptomics between shark and mouse revealed that RGs in both species exhibit high expression of Notch-family genes, while IOs express the Delta gene Dll1, suggesting that the Delta-Notch signaling axis constitutes an evolutionary toolkit for indirect neurogenesis that might have persisted for over 450 million years[26]. Intriguingly, mouse IPs exhibit an enhanced proliferative profile compared to their shark counterparts showing a stronger differentiation profile. This raises the possibility that evolutionary changes may have promoted the proliferative capacity in mammalian IPs, thereby contributing to the amplification and diversification of PN types that drive the expansion and complexification of the mammalian cortex.

Acknowledgements

We thank Dr. Dhananjay Huilgol and Dr. Yi Li for helpful discussions. We are indebted to Leah Chestnut and Aditi Patel (LifeCanvas Technologies) for their excellent work on Lightsheet Microscopy Imaging. We thank Bao-Xia for her assistance with genotyping. Funding: NIH grant U19MH114823-01 (ZJH). NIH Director's Pioneer Award 1DP1MH129954-01 (ZJH). International Postdoc Grant, Swedish Research Council grant no: 2021-00238 (SMS).

Author Contributions

ZJH and SMS conceived of the study. SMS, ZJH, XA designed experiments. SMS and XA performed the experiments. YQ designed the *FezF2-TC* mouse line. SZ made the AAV viruses. SMS and XA analysed the data with inputs from HM. SMS and ZJH wrote the manuscript. ZJH supervised all aspects of the study and provided the funding.

Declaration of interests

The authors declare no competing interests.

Inclusion and diversity

We support inclusive, diverse, and equitable conduct of research.

STAR Methods

Key resources table

REAGENT or RESOURCE	SOURCE	IDENTIFIER
Antibodies		
Chicken anti-GFP	Aves Labs	Cat# GFP-1020; RRID:AB_10000240
Rabbit anti-RFP	Rockland	Cat# 600-401-379; RRID:AB_2209751
EasyIndex	LifeCanvas Technologies	https://lifecanvastech.com/shop/easyindex/
Nissl	ThermoFisher	Cat: N21483
Bacterial and virus strains		
AAVPHP.eB-TRE3G-EGFP	This study	
AAVPHP.eB-CAG-FLEX-tdTomato	addgene	Catalog # 28306-PHPeB
AAV9-TRE3G-EGFP	This study	N/A
AAV9-CAG-FLEX-tdTomato	addgene	Catalog # 28306-AAV9
AAVretro-TRE3G-mScarlet	This study	N/A
AAVretro-CAG-DIO-EGFP	addgene	Catalog # 50457-AAV9
AAVretro-TRE3G-H2B-mScarlet	This study	N/A
AAVretro-CAG-DIO-H2B-EGFP	This study	N/A
AAVretro-CAG-EGFP	This study	N/A
Chemicals, peptides, and recombinant proteins		
Tamoxifen	Sigma	T5648
Goat serum	ThermoFisher	10000C
Triton-X100	Sigma	9036-19-5
Experimental models: Organisms/strains		
FezF2-tTA-CreER	This study	N/A
Tbr2-2A-FlpO	JAX; Huilgol et al.[17]	RRID:IMSR_JAX:036297
Fezf2-2A-CreER	JAX;Matho et al.[32]	RRID:IMSR_JAX:036296

LSL-Flpo	JAX;He et al.[91]	RRID:IMSR_JAX:028584
Intersection-Subtraction (IS2)	JAX;He et al.[91] Huilgol et al.[17]	RRID: IMSR_JAX:036760
Ai32	Madisen et al.[48]	RRID:IMSR_JAX:024109
Software and algorithms		
Matlab	MathWorks	https://www.mathworks.com/
python	Python Software Foundation	https://www.python.org/
CellPose	Pachitariu et al.[92,93]	https://cellpose.readthedocs.io/en/latest/
DeepLabCut	Mathis et al.[94]	https://github.com/DeepLabCut/
ZEN software	Zeiss	https://www.zeiss.com/microscopy/us/products/software/zeiss-zen.html
ImageJ/Fiji	Schindelin et al.[95]	https://imagej.net/software/fiji/

Resource availability

Lead contact

Further information and requests for resources and reagents should be directed to and will be fulfilled by the lead contact, Z. Josh Huang (josh.huang@duke.edu).

Materials availability

Materials generated in this study are available on request to the lead contact. *FezF2-TC* mice generated in this study will be deposited to Jackson Laboratory.

Experimental model and study participant details

We have used adult mice (*Mus musculus*) in this study. Adult male and female mice bred onto a C57BL/6J background were used in the experiments. All mouse colonies were maintained in accordance with husbandry protocols approved by the IACUC and housed by gender in groups of 2–5 with access to food and water ad libitum and on a 12-hour light/dark cycle. The experimental procedures were approved by the Institutional Animal Care and Use Committee of Duke University and performed in accordance with the US National Institutes of Health (NIH) guidelines. All adult mouse histology experiments were performed on or after postnatal day P28-P40 animals. Postnatal experiments were performed on P1-P6 mice. We have used the following knock-in mice in this study: Driver lines include *FezF2-tTA-CreER* (this study);*Tbr2-2A-FlpO* (RRID:IMSR_JAX:036297); *Fezf2-2A-CreER* (RRID:IMSR_JAX:036296). Reporter lines include *Intersection-Subtraction (IS2)* (RRID: IMSR_JAX:036760) and *LSL-Flpo* (RRID:IMSR_JAX:028584). Mouse related experimental procedures were approved by the Institutional Animal Care and Use Committee (IACUC) of Duke University in accordance with NIH guidelines.

Method details

Generation of *FezF2-tTA-CreER* knock-in mouse line

FezF2-tTA-CreER was generated by inserting a *frt-tTA-frt-CreER* cassette in frame before the STOP codon of *FezF2*. In *FezFTC;Tbr2-Flp* double-allele mice, dNG-derived ET^d express *tTA* while iNG-derived ET^i express *CreER*, as *tTA* is removed by *Tbr2-Flp* in IPs. Postnatal injection of *AAV-TRE-GFP* and *AAV-FLEX-RFP* in cortex differentially label ET^d and ET^i respectively. Targeting vectors were generated using a PCR-based cloning approach as described before [17,32,91].

Tamoxifen induction

Tamoxifen (T5648, Sigma) was prepared by dissolving the powder in corn oil (20 mg/ml) and constant magnetic stirring overnight at 37°C. A 100–200 mg/kg dose was administered by intraperitoneal injection at the appropriate age; If two doses, 100mg/kg doses were administered at P21 and P28. For experiments with early postnatal mice, it was administered intraperitoneally at P5-P14 from a diluted stock of 5mg/ml. For *FezF2TC;Tbr2Flp* mice with viral infections, tamoxifen induction was performed via intraperitoneal injections at a dose of 100 mg/kg with the first induction after one day following the viral infection and subsequently every 2-3 days, 2-3 times.

Immunohistochemistry

Adult mice were anaesthetized (using Isoflurane) and transcardially perfused with phosphate buffered saline (PBS) followed by 4% paraformaldehyde (PFA) in 0.1 M PBS. Post-fixation, brains were rinsed three times in PBS and sectioned at a 65-70µm thickness with a Leica VT1000S vibratome. Sections were treated with a blocking solution (10% normal goat serum and 0.2% Triton-X100 in 1X PBS) for 1h, then incubated overnight at 4°C with primary antibodies diluted in the blocking solution. Sections were washed three times in PBS and incubated for 2h at room temperature with corresponding secondary antibodies, Goat or Donkey Alexa Fluor 488, 594 or 647 (1:500, Life Technologies) and DAPI or Blue/Far-Red Neurotrace fluorescent Nissl stain to label nuclei (1:1000 in PBS, Life Technologies, 33342, Molecular Probes N21479). Sections were washed three times with PBS and dry-mounted on slides using Fluoromount-G (SouthernBiotech, 0100-01) mounting medium.

In situ hybridization

Hybridization chain reaction (HCR) in situ was performed as previously described[96]. *FezF2* probes were ordered from Molecular Instruments. Mouse brains were sliced into 50-µm-thick slices after paraformaldehyde (PFA) perfusion fixation and sucrose protection. HCR in situ was performed via the free-floating method in a 24-well plate. First, brain slices were exposed to a probe hybridization buffer with HCR Probe Set at 37□°C for 24□hours. Brain slices were washed with a probe wash buffer, incubated with amplification buffer and amplified at 25□°C for 24□hours. On day 3, brain slices were washed, counter-stained with DAPI/Nissl and mounted. *FezF2* (546□nm) probes were used to label *FezF2*+ neurons.

Viral vectors

All viral vectors were produced in house. Viral Vectors used: *AAV9-CAG-FLEX-tdTomato*, *AAV9-TRE3G-EGFP, AAVPHP.eB-TRE3G-EGFP, AAVPHP.eB-CAG-FLEX-tdTomato, AAVretro-TRE3G-mScarlet, AAVretro-CAG-DIO-EGFP, AAVretro-TRE3G-H2B-mScarlet, AAVretro-CAG-DIO-H2B-EGFP, AAVretro-CAG-EGFP*. All viral vectors were aliquoted and stored at -80 °C until use.

Stereotaxic surgery

Mice, anesthetized with isoflurane (2-5 % at the beginning and 0.8-1.2 % for the rest of the surgical procedure), were positioned in a stereotaxic frame and their body temperature was maintained at 34-37

°C with a heating pad. Lidocaine (2%) was applied subcutaneously to the scalp prior to surgery. Ketoprofen (5 mg/kg) was administered intraperitonially (IP) as an analgesic before and after surgery. A vertical incision was made through the scalp and connective tissue to expose the dorsal surface of the skull. The skin was pushed aside, and the skull surface was cleared using saline. A digital mouse brain atlas, linked to the stereotaxic frame, guided the identification and targeting of different brain areas (Angle Two Stereotaxic System, Leica Biosystems). A small burr hole was drilled in the skull and brain surface was exposed. A pulled glass pipette, with a tip of 20-30 µm, containing the viral suspension was lowered into the brain. A 500-700 nl volume was delivered at a rate of 10-30 nl/min using a Picospritzer (General Valve Corp). The pipette remained in place for 5 min, to prevent backflow, prior to retraction. The incision was closed with Tissueglue (3M Vetbond) and 5/0 nylon suture thread (Ethilon Nylon Suture, Ethicon). The mice were kept warm on a heating pad during recovery. Coordinates used are as follows (all measured in mm from bregma except for medulla):

Area	Anterior/Posterior (+/-,mm)	Lateral/Medial (+/-,mm)	Dorsal/Ventral (+/-,mm)
Rostral forelimb orofacial area (RFO)	1.71	2.25	-0.65
Caudal forelimb area (CFA)	0.5	1.5	0.6
Secondary motor cortex (MOS)	1.6	1.37	-0.7
Visual Cortex (VIS)	-3.4	2.6	0.55
Auditory Cortex (AUD)	-2.6	4	-0.95
Barrel Cortex (BAR)	-1.1	3.1	-0.6
Prefrontal Cortex (PFC)	1.7	0.4	-1.5
Parietal Cortex (PAR)	-1.85	1.3	-0.6
Superior Colliculus	-3.68	0.5	-1.6
PONS	-4	0.5	-5.5
Medulla [measured from Lambda]	-1.4	1.55	-4.3

Injections into the spinal cord of adult mice were performed as described[97]. Specifically, a dorsal incision was made along the vertebral column at the cervical level. The overlying muscle was dissected to expose the cervical vertebral column, and a laminectomy was performed at C5-7 to expose the spinal cord. 0.5 µl of viral solution was injected at 0.4 mm lateral to midline and 0.5 mm and 1 mm depth using a glass micropipette. The dorsal muscle layers were sutured, and the skin was closed with

sterile wound clips. For all anterograde and retrograde injections, a viral suspension containing a mixture of *AAV9-CAG-FLEX-tdTomato* and *AAV9-TRE3G-EGFP* or *AAVretro-CAG-DIO-EGFP* and *AAVretro-TRE3G-H2B-mScarlet* was used respectively, in the ratio 1:1. Injections into the cervical spinal cord of P1,P4 or P6 mice were performed using a Hamilton syringe (5 µl) with a mixture of *AAVretro-TRE3G-H2B-mScarlet* and *AAVretro-CAG-DIO-H2B-EGFP* (1:1, 2-2.5 µl) or just *AAVretro-CAG-EGFP* (1-2 µl) as described [98].

Light-Sheet Fluorescence Microscopy

For all anterograde and retrograde injections, post-fixed brains were processed for tissue-clearing, antibody staining and Lightsheet Scanning. A total of 36 brains were processed and imaged by LightSheet Microscopy (by LifeCanvas Technologies (LCT)).

Tissue Preservation, Clearing, Immunolabeling and Imaging

Paraformaldehyde-fixed samples were preserved using SHIELD reagents (LCT) using the manufacturer's instructions [99]. Samples were delipidated using LCT Clear+ delipidation reagents for 2 days. Following delipidation, samples were labeled using eFLASH[100] technology which integrates stochastic electrotransport [101] and SWITCH [102], using a SmartBatch+ (or SmartLabel) device (LCT). For immunolabeling, the samples were incubated with 96 µg Chicken anti-GFP, 50 µg Goat anti-RFP, and 72 µg Rabbit NeuN (36 brains) following which the samples were incubated in 50% EasyIndex (RI = 1.52) overnight at 37°C followed by 1 d incubation in 100% EasyIndex for refractive index matching (RI = 1.52). After index matching the samples were imaged using a SmartSPIM axially swept light sheet microscope using a 3.6x objective (0.2 NA) with 4 um z-step, and 1.8 um x-y pixel size.

Atlas Registration (NeuN)

Samples were registered to the Allen Brain Atlas[103] using an automated process (LCT). A NeuN channel for each brain was registered to an average NeuN atlas (generated by using previously registered samples). Registration was performed using successive rigid, affine, and b-spline warping algorithms (SimpleElastix: https://simpleelastix.github.io/).

Cell Detection

Automated cell detection was performed by using a custom convolutional neural network created with the Tensorflow python package (Google, LCT). The cell detection was performed by two networks in sequence. First, a fully- convolutional detection network [104] based on a U-Net architecture [105] was used to find possible positive locations. Second, a convolutional network using a ResNet architecture [106] was used to classify each location as positive or negative. Using the previously calculated Atlas Registration, each cell location was projected onto the Allen Brain Atlas in order to count the number of cells for each atlas- defined region.

Image Segmentation and Thresholding

Process-specific signals were identified by applying an absolute intensity threshold to each voxel within the volumetric image. Voxels exhibiting fluorescence intensity greater than the predetermined threshold were classified as “positive.”

Atlas Registration (Anterograde projections)

The pixels from the resulting segmentation mask were spatially transformed (warped) to the Allen Brain Atlas to determine which region each positive pixel belongs to.

Computation of Fraction Occupation and Percent Occupation

For each anatomical region defined by the registered atlas, the number of positive voxels (i.e., those exceeding the intensity threshold) was summed. This count was then divided by the total voxel count of the same region to yield the fraction occupation metric:

$$\text{Fraction Occupation}_{\text{region}} = \frac{N_{\text{positive voxels, region}}}{N_{\text{total voxels, region}}}$$

$$\text{Percent Occupation}_{\text{region}} = 100 \times \text{Fraction Occupation}_{\text{region}}$$

Coronal Video Reconstruction

Whole Brains were imaged by LightSheet Microscopy horizontally at a resolution of 1.8, 1.8, and 4 um for the medial-lateral, anterior-posterior, and dorsal-ventral axes respectively. The acquired whole-brain image data was resampled to generate a series of raw coronal images with a resolution of 1.8 and 4 um for the medial-lateral and dorsal-ventral axes respectively. The dorsal-ventral axis was downsampled to a resolution of 54 um. To make the video of coronal images, we further downsampled each raw coronal image five times. The display range of each color channel was carefully adjusted linearly to reveal axons and cell bodies of anterograde and retrograde tracing data respectively.

Confocal Microscopy

Confocal photomicrographs were obtained using a Zeiss Laser scanning microscope (LSM 900, in house). Tile-scans were taken with a 5x objective while Z-stacks of optical sections were obtained using either a 10x or a 20x objective. Projection images and illustrations were processed/prepared by Zeiss ZEN software, ImageJ and Adobe Illustrator CC. Various sections of interest from a total of 40 mouse brains were analyzed using confocal microscopy.

Optogenetic activation of ET^{all}, ET^{d} and ET^{i}

For optogenetic activation, ChRmine was expressed in ET^{d} on the ipsilateral side of RFO using viral injections of AAV8-TRE3G-ChRmine-oScarlet and in ET^{i} using AAV8-nEF-FLEX-ChRmine-oScarlet on the contralateral side of RFO in the same *FezF2TC;Tbr2Flp* mice. For optogenetic activation of ET^{all}, *FezF2CreER* mice were crossed with the *Ai32* reporter mice to express channelrhodopsin in all *FezF2*$^{+}$ neurons. Tapered optical fibers (diameter 200 µm; NA, 0.37; taper 1 mm) were implanted bilaterally in the RFO. The optical fibers were implanted at a depth 650 µm from the cortical surface. To fix the implants to the skull, a silicone adhesive (Kwik-Sil, WPI) was applied to cover the hole, followed by a layer of dental cement (C&B Metabond, Parkell), black instant adhesive (Loctite 426), and dental cement (Ortho-Jet, Lang Dental). A titanium head bar was fixed to the skull near Lambda using dental cement.

During head-fixed activation, two cameras (FL3-U3-13S2C-CS, FLIR) were placed in front of the mice. Two LED light lamps next to the two cameras provided illumination. A fiber coupled laser (5-ms pulses, 10-20 mW; λ = 473/630 nm) was used to apply stimulation at 10, 20, 30, and 50 Hz and constantly for 0.5 s. For free-moving activation, mice with optical fibers implanted in the RFO were placed into an acrylic activity box (14 cm × 14 cm × 16.5 cm, L × W × H). A 473-nm laser (5-ms pulses, 10 mW) coupled to a rotary joint (RJPFL2, Thorlabs) was used to apply stimulation at 10, 20, 30, and 50 Hz and constantly for 0.5 s. One camera (FL3-U3-13S2C-CS, FLIR) was used to take video recordings at a

frame rate of 100 Hz from the bottom of the activity box. A LED light lamp adjacent to the camera provided illumination.

Data Analysis

Heatmap Visualization of Projection Patterns

For anterograde projections, fraction occupation percentage data (obtained from the LightSheet analysis pipeline, LCT) were extracted for selected ipsilateral and contralateral brain regions for each injection site. For each injection site, the downstream areas selected across the brain were based on comparisons of equivalent injections (based on coordinates) in the isocortex from the Allen Mouse Brain Connectivity dataset (https://community.brain-map.org/t/api-allen-brain-connectivity/2988). The downstream areas selected for each injection site are listed in Table S1. The data were then normalized, and the mean GFP and RFP values were calculated for each region. For global normalization, Min-Max scaling was applied to the combined GFP and RFP data across both ipsilateral and contralateral regions. The final normalized data were saved for further analysis. Normalized mean fraction occupation for ET^d and ET^i were visualized as heatmaps, for both ipsilateral and contralateral projections across different selected regions. Region names were aligned along the y-axis, and color intensity scaled to reflect normalized fraction occupation.

Linear Regression and Visualization

ET^d and ET^i fraction occupations for each injection site from target structures of interest (eg: thalamus, midbrain, PONS, medulla were extracted for both ipsilateral and contralateral regions. Structures selected for each of the target structures considered for each injection site are listed in Table S1. For each target structure, linear regression (polyfit) was performed between ET^d and ET^i fraction occupation values. Regression lines were plotted alongside scatter plots of individual data points representing ipsilateral and contralateral areas within each region group. Anatomical area labels were overlaid on the plots using text annotations. ET^d and ET^i fraction occupation values for two region groups compared were normalized using z-score transformation. The z-score for each data point was calculated using the formula:

$$z = (x - \mu) / \sigma$$

where x is the data point, μ is the global mean of the two region groups, and σ is the global standard deviation of two region groups. Percent occupation differences ($\Delta = ET^d - ET^i$) were computed for each target structure. Statistical tests were performed within-group and visualized through boxplots with median, interquartile range, and individual data points along with p-value annotations to indicate statistical significance. To further assess whether the percent occupation differences ($\Delta = ET^d - ET^i$) were uniform across different target structures from an injection site, a multicomparisons test followed by post-hoc comparisons were performed. Post-hoc comparisons were done between different target structures and the thalamus. Since the thalamus in general received significant ET^d and ET^i projections, it was used as a control for comparison with other target structures.

Cell Count Quantification Using Cellpose

Cell body segmentation and quantification for confocal images were performed using the Cellpose algorithm [92], a deep learning-based tool for cellular segmentation. Images were preprocessed for contrast enhancement and background subtraction before input into Cellpose. The “cyto” model was

used with default parameters, and the estimated cell diameter was manually specified or automatically determined, depending on image resolution.

Batch segmentation was conducted via the Cellpose GUI or command-line interface, and outputs were visually inspected for accuracy. Resulting masks were used to quantify total cell counts per region or image.

Correlation Analysis

Correlation analysis was performed on either projection fraction occupation values or cell counts across brain regions, on brains scanned by Lightsheet Microscopy. For each subject, direct and indirect data from both hemispheres were combined. Correlation matrices were computed using Pearson correlation coefficients and visualized as heatmaps to compare projection/cell count similarities across individual mice.

Video analysis for optogenetic activation

Videos of behavior from head-fixed activation were analyzed with DeepLabCut[94]. The two cameras were calibrated using the Camera Calibrator App in MATLAB. For DeepLabCut training, 750 images were used from the frontal video recordings to track the movements of the jaw and hands. The tracking results were validated manually and errors were corrected accordingly in MATLAB. Trials in which mice made spontaneous movements before stimulation onset (within 0.5 s) were excluded from the analyses, based on either manual examinations or setting threshold (3 × SD from the mean) on average speed distributions of all trials. For videos obtained from free-moving activation, the tracking of different body parts was performed using DeepLabCut. The network was trained with 500 images. Seven body parts (left and right hands and feet, nose tip, jaw, and tail base) were labeled in the images. The behavioral videos and tracking results were visualized and analyzed in a custom-written MATLAB app. Tracking errors were corrected using the app.

Statistical analysis

For statistical comparisons, normality of the dataset was assessed using either the Shapiro-Wilk test or the Kolmogorov-Smirnov test. When data were not normally distributed, non-parametric statistical tests were used. For multiple comparisons, normality was assessed using the Lilliefors test followed by a nonparametric Kruskal-Wallis test. Post-hoc comparisons of different target regions with thalamus were performed by pairwise Wilcoxon rank-sum tests or Kolmogorov-Smirnov (KS) tests. To control for multiple comparisons while preserving statistical power, all post hoc p-values were corrected using the Benjamini-Hochberg false discovery rate (FDR) method. Significance levels used in the analyses and figures were as follows: *$P < 0.05$, **$P < 0.01$, ***$P < 0.005$, ****$P < 0.001$, *****$P < 0.0001$, and n.s. (not significant). Data are presented as median with the 25th–75th percentiles (IQR), or as mean ± s.d., unless otherwise indicated. All statistics were implemented in MATLAB.

Data availability/Code availability

The data that support the findings of this study are available from the lead contact upon reasonable request. Custom-written scripts used in this study are available from: https://github.com/ShreyasDuke/ETd-ETi-Code.git. Anterograde projection and cell distribution video datasets can be viewed at: https://figshare.com/s/4aa9d712da9756bc7551.

REFERENCES:

1. Suryanarayana, S.M., Robertson, B., and Grillner, S. (2022). The neural bases of vertebrate motor behaviour through the lens of evolution. Philos. Trans. R. Soc. Lond. B Biol. Sci. *377*, 20200521.

2. Swanson, L.W. (2000). Cerebral hemisphere regulation of motivated behavior. Brain Res. *886*, 113–164.

3. Douglas, R.J., and Martin, K.A. (2012). Behavioral architecture of the cortical sheet. Curr. Biol. *22*, R1033-8.

4. Rakic, P. (2009). Evolution of the neocortex: a perspective from developmental biology. Nat. Rev. Neurosci. *10*, 724–735.

5. Tasic, B., Yao, Z., Graybuck, L.T., Smith, K.A., Nguyen, T.N., Bertagnolli, D., Goldy, J., Garren, E., Economo, M.N., Viswanathan, S., et al. (2018). Shared and distinct transcriptomic cell types across neocortical areas. Nature *563*, 72–78.

6. Harris, K.D., and Shepherd, G.M.G. (2015). The neocortical circuit: themes and variations. Nat. Neurosci. *18*, 170–181.

7. Huang, Z.J. (2014). Toward a genetic dissection of cortical circuits in the mouse. Neuron *83*, 1284–1302.

8. Lemon, R.N., and Griffiths, J. (2005). Comparing the function of the corticospinal system in different species: organizational differences for motor specialization? Muscle Nerve *32*, 261–279.

9. Lemon, R.N. (2008). Descending pathways in motor control. Annu. Rev. Neurosci. *31*, 195–218.

10. Munoz-Castaneda, R., Zingg, B., Matho, K.S., Chen, X., Wang, Q., Foster, N.N., Li, A., Narasimhan, A., Hirokawa, K.E., Huo, B., et al. (2021). Cellular anatomy of the mouse primary motor cortex. Nature *598*, 159–166.

11. Carmona, L.M., Thomas, E.D., Smith, K., Tasic, B., Costa, R.M., and Nelson, A. (2024). Topographical and cell type-specific connectivity of rostral and caudal forelimb corticospinal neuron populations. Cell Rep. *43*, 113993.

12. Economo, M.N., Viswanathan, S., Tasic, B., Bas, E., Winnubst, J., Menon, V., Graybuck, L.T., Nguyen, T.N., Smith, K.A., Yao, Z., et al. (2018). Distinct descending motor cortex pathways and their roles in movement. Nature *563*, 79–84.

13. Shepherd, G.M.G. (2014). Diversity and complexity in the pyramidal tract projectome. Nat. Rev. Neurosci. *15*, 63.

14. Smith, Y., Wichmann, T., and DeLong, M.R. (2014). Corticostriatal and mesocortical dopamine systems: do species differences matter? Nat. Rev. Neurosci. *15*, 63.

15. Kita, T., and Kita, H. (2012). The subthalamic nucleus is one of multiple innervation sites for long-range corticofugal axons: a single-axon tracing study in the rat. J. Neurosci. *32*, 5990–5999.

16. Beattie, R., and Hippenmeyer, S. (2017). Mechanisms of radial glia progenitor cell lineage progression. FEBS Lett. *591*, 3993–4008.

17. Huilgol, D., Levine, J.M., Galbavy, W., Wang, B.S., He, M., Suryanarayana, S.M., and Huang, Z.J. (2023). Direct and indirect neurogenesis generate a mosaic of distinct glutamatergic projection neuron types in cerebral cortex. Neuron. https://doi.org/10.1016/j.neuron.2023.05.021.

18. Martinez-Cerdeno, V., Noctor, S.C., and Kriegstein, A.R. (2006). The role of intermediate progenitor cells in the evolutionary expansion of the cerebral cortex. Cereb. Cortex *16 Suppl 1*, i152-61.

19. Noctor, S.C., Martinez-Cerdeno, V., Ivic, L., and Kriegstein, A.R. (2004). Cortical neurons arise in symmetric and asymmetric division zones and migrate through specific phases. Nat. Neurosci. *7*, 136–144.

20. Kriegstein, A., Noctor, S., and Martínez-Cerdeño, V. (2006). Patterns of neural stem and progenitor cell division may underlie evolutionary cortical expansion. Nat. Rev. Neurosci. *7*, 883–890.

21. Kriegstein, A., and Alvarez-Buylla, A. (2009). The glial nature of embryonic and adult neural stem cells. Annu. Rev. Neurosci. *32*, 149–184.

22. Dimou, L., and Götz, M. (2014). Glial cells as progenitors and stem cells: new roles in the healthy and diseased brain. Physiol. Rev. *94*, 709–737.

23. Hevner, R.F. (2019). Intermediate progenitors and Tbr2 in cortical development. J. Anat. *235*, 616–625.

24. Florio, M., and Huttner, W.B. (2014). Neural progenitors, neurogenesis and the evolution of the neocortex. Development *141*, 2182–2194.

25. Baumann, N., Wagener, R.J., Javed, A., Conti, E., Abe, P., Lopes, A., Sansevrino, R., Lavalley, A., Magrinelli, E., Szalai, T., et al. (2025). Regional differences in progenitor metabolism shape brain growth during development. Cell. https://doi.org/10.1016/j.cell.2025.04.003.

26. Quintana-Urzainqui, I., Oel, P.A., Gerber, T., Pan, L., Papadopoulos, N., Serka, Z.G., Verbanac, A., Börsig, M., Torres-Sabino, D., Rollán-Delgado, I.C., et al. (2025). Developmental landscape of shark telencephalon sheds light on the evolution of telencephalic cell types and the ancient origin of Cajal-Retzius cells. bioRxiv. https://doi.org/10.1101/2025.05.08.652169.

27. Deryckere, A., Choudhary, S., Lynch, C., Limperis, L.K.V.P., Affatato, P., Woych, J., Gumnit, E., Ortega Gurrola, A., Satija, R., Mayer, C., et al. (2025). A conserved logic for the development of cortical layering in tetrapods. bioRxiv, 2025.10.01.679862. https://doi.org/10.1101/2025.10.01.679862.

28. Cárdenas, A., and Borrell, V. (2020). Molecular and cellular evolution of corticogenesis in amniotes. Cell. Mol. Life Sci. *77*, 1435–1460.

29. Espinós, A., Fernández-Ortuño, E., Negri, E., and Borrell, V. (2022). Evolution of genetic mechanisms regulating cortical neurogenesis. Dev. Neurobiol. *82*, 428–453.

30. Hatanaka, Y., Yamada, K., Eritate, T., Kawaguchi, Y., and Hirata, T. (2024). Neuronal fate resulting from indirect neurogenesis in the mouse neocortex. Cereb. Cortex *34*. https://doi.org/10.1093/cercor/bhae439.

31. Arlotta, P., Molyneaux, B.J., Chen, J., Inoue, J., Kominami, R., and Macklis, J.D. (2005). Neuronal subtype-specific genes that control corticospinal motor neuron development in vivo. Neuron *45*,

207–221.

32. Matho, K.S., Huilgol, D., Galbavy, W., He, M., Kim, G., An, X., Lu, J., Wu, P., Di Bella, D.J., Shetty, A.S., et al. (2021). Genetic dissection of the glutamatergic neuron system in cerebral cortex. Nature *598*, 182–187.

33. An, X., Matho, K.S., Li, Y., Mohan, H., Xu, X.H., Whisaw, I., Kepecs, A., and Huang, J. (2022). A cortical circuit for orchestrating oromanual food manipulation. bioRxiv. https://doi.org/10.1101/2022.12.03.518964.

34. Brown, A.R., and Teskey, G.C. (2014). Motor cortex is functionally organized as a set of spatially distinct representations for complex movements. J. Neurosci. *34*, 13574–13585.

35. Morandell, K., and Huber, D. (2017). The role of forelimb motor cortex areas in goal directed action in mice. Sci. Rep. *7*, 15759.

36. Tennant, K.A., Adkins, D.L., Donlan, N.A., Asay, A.L., Thomas, N., Kleim, J.A., and Jones, T.A. (2011). The organization of the forelimb representation of the C57BL/6 mouse motor cortex as defined by intracortical microstimulation and cytoarchitecture. Cereb. Cortex *21*, 865–876.

37. Li, Y., An, X., Mulcahey, P.J., Qian, Y., Xu, X.H., Zhao, S., Mohan, H., Suryanarayana, S.M., Bachschmid-Romano, L., Brunel, N., et al. (2024). Cortico-thalamic communication for action coordination in a skilled motor sequence. bioRxiv, 2023.10.25.563871.

38. Grillner, S., Robertson, B., and Kotaleski, J.H. (2020). Basal Ganglia-A Motion Perspective. Compr. Physiol. *10*, 1241–1275.

39. Markowitz, J.E., Gillis, W.F., Beron, C.C., Neufeld, S.Q., Robertson, K., Bhagat, N.D., Peterson, R.E., Peterson, E., Hyun, M., Linderman, S.W., et al. (2018). The Striatum Organizes 3D Behavior via Moment-to-Moment Action Selection. Cell *174*, 44-58 e17.

40. Sherman, S.M., and Guillery, R.W. (2001). Exploring the thalamus (Elsevier).

41. Mohan, H., An, X., Xu, X.H., Kondo, H., Zhao, S., Matho, K.S., Wang, B.S., Musall, S., Mitra, P., and Huang, Z.J. (2023). Cortical glutamatergic projection neuron types contribute to distinct functional subnetworks. Nat. Neurosci. *26*, 481–494.

42. Binkofski, F., and Buccino, G. (2018). The role of the parietal cortex in sensorimotor transformations and action coding. Handb. Clin. Neurol. *151*, 467–479.

43. Anastasiades, P.G., and Carter, A.G. (2021). Circuit organization of the rodent medial prefrontal cortex. Trends Neurosci. *44*, 550–563.

44. Riccomagno, M.M., and Kolodkin, A.L. (2015). Sculpting neural circuits by axon and dendrite pruning. Annu. Rev. Cell Dev. Biol. *31*, 779–805.

45. Luo, L., and O'Leary, D.D.M. (2005). Axon retraction and degeneration in development and disease. Annu. Rev. Neurosci. *28*, 127–156.

46. Stanfield, B.B., O'Leary, D.D., and Fricks, C. (1982). Selective collateral elimination in early postnatal development restricts cortical distribution of rat pyramidal tract neurones. Nature *298*, 371–373.

47. Abe, P., Lavalley, A., Morassut, I., Santinha, A.J., Roig-Puiggros, S., Javed, A., Klingler, E.,

Baumann, N., Prados, J., Platt, R.J., et al. (2024). Molecular programs guiding arealization of descending cortical pathways. Nature *634*, 644–651.

48. Madisen, L., Mao, T., Koch, H., Zhuo, J.-M., Berenyi, A., Fujisawa, S., Hsu, Y.-W.A., Garcia, A.J., 3rd, Gu, X., Zanella, S., et al. (2012). A toolbox of Cre-dependent optogenetic transgenic mice for light-induced activation and silencing. Nat Neurosci *15*, 793–802.

49. Lemon, R. (2019). Recent advances in our understanding of the primate corticospinal system. F1000Res. *8*. https://doi.org/10.12688/f1000research.17445.1.

50. Brain Initiative Cell Census Network (2021). A multimodal cell census and atlas of the mammalian primary motor cortex. Nature *598*, 86–102.

51. Ocana, F.M., Suryanarayana, S.M., Saitoh, K., Kardamakis, A.A., Capantini, L., Robertson, B., and Grillner, S. (2015). The lamprey pallium provides a blueprint of the mammalian motor projections from cortex. Curr. Biol. *25*, 413–423.

52. Suryanarayana, S.M., Robertson, B., Wallen, P., and Grillner, S. (2017). The Lamprey Pallium Provides a Blueprint of the Mammalian Layered Cortex. Curr. Biol. *27*, 3264-3277 e5.

53. Suryanarayana, S.M., Perez-Fernandez, J., Robertson, B., and Grillner, S. (2022). The Lamprey Forebrain - Evolutionary Implications. Brain Behav. Evol. *96*, 318–333.

54. Lopes, G., and Kampff, A.R. (2015). Cortical control: learning from the lamprey. Curr. Biol. *25*, R203-5.

55. Isa, T., Marquez-Legorreta, E., Grillner, S., and Scott, E.K. (2021). The tectum/superior colliculus as the vertebrate solution for spatial sensory integration and action. Curr. Biol. *31*, R741–R762.

56. Grillner, S., and Robertson, B. (2016). The Basal Ganglia Over 500 Million Years. Curr. Biol. *26*, R1088-r1100.

57. Grillner, S., and El Manira, A. (2020). Current Principles of Motor Control, with Special Reference to Vertebrate Locomotion. Physiol. Rev. *100*, 271–320.

58. Briscoe, S.D., and Ragsdale, C.W. (2019). Evolution of the Chordate Telencephalon. Curr. Biol. *29*, R647–R662.

59. Briscoe, S.D., and Ragsdale, C.W. (2018). Homology, neocortex, and the evolution of developmental mechanisms. Science *362*, 190–193.

60. Ruder, L., and Arber, S. (2019). Brainstem Circuits Controlling Action Diversification. Annu. Rev. Neurosci. *42*, 485–504.

61. Arber, S., and Costa, R.M. (2022). Networking brainstem and basal ganglia circuits for movement. Nat. Rev. Neurosci. *23*, 342–360.

62. Arber, S., and Costa, R.M. (2018). Connecting neuronal circuits for movement. Science *360*, 1403–1404.

63. Cisek, P. (2022). Evolution of behavioural control from chordates to primates. Philos. Trans. R. Soc. Lond. B Biol. Sci. *377*, 20200522.

64. Suryanarayana, S.M., and Huilgol, D. (2023). Conservation and diversification of pallial cell types

across vertebrates - an evo-devo perspective. Brain Behav. Evol. https://doi.org/10.1159/000531718.

65. Mayrhofer, J.M., El-Boustani, S., Foustoukos, G., Auffret, M., Tamura, K., and Petersen, C.C.H. (2019). Distinct Contributions of Whisker Sensory Cortex and Tongue-Jaw Motor Cortex in a Goal-Directed Sensorimotor Transformation. Neuron *103*, 1034-1043 e5.

66. Yang, W., Kanodia, H., and Arber, S. (2023). Structural and functional map for forelimb movement phases between cortex and medulla. Cell *186*, 162-177 e18.

67. Tyssowski, K.M., Cohen, J.D., Guo, J.-Z., Richardson, P.R., Cortina, K.E., Smith, I.H., Eijogu, D.C., Hantman, A.W., and Hoekstra, H.E. (2025). Evolutionary expansion of the corticospinal system is linked to dexterity in mice. bioRxiv. https://doi.org/10.1101/2025.10.16.682851.

68. Ferenczi, E.A., Wang, W., Biswas, A., Pottala, T., Dong, Y., Chan, A.K., Albanese, M.A., Sohur, R.S., Jia, T., Mastro, K.J., et al. (2024). Projections between the globus pallidus externa and cortex span motor and non-motor regions. bioRxiv, 2024.11.08.622712.

69. Thompson, W.S., Grillner, S., and Silberberg, G. (2024). Motor cortex directly excites the output nucleus of the basal ganglia, the substantia nigra pars reticulata. bioRxiv, 2024.03.19.585632.

70. Kawai, R., Markman, T., Poddar, R., Ko, R., Fantana, A.L., Dhawale, A.K., Kampff, A.R., and Olveczky, B.P. (2015). Motor cortex is required for learning but not for executing a motor skill. Neuron *86*, 800–812.

71. Redgrave, P., Prescott, T.J., and Gurney, K. (1999). The basal ganglia: a vertebrate solution to the selection problem? Neuroscience *89*, 1009–1023.

72. Petersen, C.C. (2007). The functional organization of the barrel cortex. Neuron *56*, 339–355.

73. Kaas, J.H. (2011). Reconstructing the areal organization of the neocortex of the first mammals. Brain Behav. Evol. *78*, 7–21.

74. Kaas, J.H. (2013). The evolution of brains from early mammals to humans. Wiley Interdiscip. Rev. Cogn. Sci. *4*, 33–45.

75. Crombie, D., and Busse, L. (2021). Should I stay or should I go? A thalamic circuit for modulating behavioral responses to visual threat. Neuron *109*, 3717–3719.

76. Fratzl, A., Koltchev, A.M., Vissers, N., Tan, Y.L., Marques-Smith, A., Stempel, A.V., Branco, T., and Hofer, S.B. (2021). Flexible inhibitory control of visually evoked defensive behavior by the ventral lateral geniculate nucleus. Neuron *109*, 3810-3822 e9.

77. Mederos, S., Blakely, P., Vissers, N., Clopath, C., and Hofer, S.B. (2025). Overwriting an instinct: Visual cortex instructs learning to suppress fear responses. Science *387*, 682–688.

78. Veinante, P., and Deschenes, M. (1999). Single- and multi-whisker channels in the ascending projections from the principal trigeminal nucleus in the rat. J. Neurosci. *19*, 5085–5095.

79. Brecht, M., and Sakmann, B. (2002). Whisker maps of neuronal subclasses of the rat ventral posterior medial thalamus, identified by whole-cell voltage recording and morphological reconstruction. J. Physiol. *538*, 495–515.

80. Grothe, B., Pecka, M., and McAlpine, D. (2010). Mechanisms of sound localization in mammals.

Physiol. Rev. *90*, 983–1012.

81. Du, X., Xu, H., Song, P., Zhai, Y., Ye, H., Bao, X., Huang, Q., Tanigawa, H., Tu, Z., Chen, P., et al. (2025). The multifaceted role of the inferior colliculus in sensory prediction, reward processing, and decision-making. Elife *13*. https://doi.org/10.7554/eLife.101142.

82. Carandini, M., and Churchland, A.K. (2013). Probing perceptual decisions in rodents. Nat. Neurosci. *16*, 824–831.

83. Odoemene, O., Pisupati, S., Nguyen, H., and Churchland, A.K. (2018). Visual Evidence Accumulation Guides Decision-Making in Unrestrained Mice. J. Neurosci. *38*, 10143–10155.

84. Miller, E.K. (2000). The prefrontal cortex and cognitive control. Nat. Rev. Neurosci. *1*, 59–65.

85. Allsop, S.A., Wichmann, R., Mills, F., Burgos-Robles, A., Chang, C.J., Felix-Ortiz, A.C., Vienne, A., Beyeler, A., Izadmehr, E.M., Glober, G., et al. (2018). Corticoamygdala Transfer of Socially Derived Information Gates Observational Learning. Cell *173*, 1329-1342 e18.

86. Gangopadhyay, P., Chawla, M., Dal Monte, O., and Chang, S.W.C. (2021). Prefrontal-amygdala circuits in social decision-making. Nat. Neurosci. *24*, 5–18.

87. Eichenbaum, H. (2017). Prefrontal-hippocampal interactions in episodic memory. Nat. Rev. Neurosci. *18*, 547–558.

88. Jin, J., and Maren, S. (2015). Prefrontal-Hippocampal Interactions in Memory and Emotion. Front. Syst. Neurosci. *9*, 170.

89. Souza, R., Bueno, D., Lima, L.B., Muchon, M.J., Goncalves, L., Donato, J., Jr, Shammah-Lagnado, S.J., and Metzger, M. (2022). Top-down projections of the prefrontal cortex to the ventral tegmental area, laterodorsal tegmental nucleus, and median raphe nucleus. Brain Struct. Funct. *227*, 2465–2487.

90. Cárdenas, A., Villalba, A., de Juan Romero, C., Picó, E., Kyrousi, C., Tzika, A.C., Tessier-Lavigne, M., Ma, L., Drukker, M., Cappello, S., et al. (2018). Evolution of Cortical Neurogenesis in Amniotes Controlled by Robo Signaling Levels. Cell *174*, 590-606.e21.

91. He, M., Tucciarone, J., Lee, S., Nigro, M.J., Kim, Y., Levine, J.M., Kelly, S.M., Krugikov, I., Wu, P., Chen, Y., et al. (2016). Strategies and tools for combinatorial targeting of GABAergic neurons in mouse cerebral cortex. Neuron *91*, 1228–1243.

92. Stringer, C., Wang, T., Michaelos, M., and Pachitariu, M. (2021). Cellpose: a generalist algorithm for cellular segmentation. Nat. Methods *18*, 100–106.

93. Pachitariu, M., Rariden, M., and Stringer, C. (2025). Cellpose-SAM: superhuman generalization for cellular segmentation. bioRxiv, 2025.04.28.651001. https://doi.org/10.1101/2025.04.28.651001.

94. Mathis, A., Mamidanna, P., Cury, K.M., Abe, T., Murthy, V.N., Mathis, M.W., and Bethge, M. (2018). DeepLabCut: markerless pose estimation of user-defined body parts with deep learning. Nat. Neurosci. *21*, 1281–1289.

95. Schindelin, J., Arganda-Carreras, I., Frise, E., Kaynig, V., Longair, M., Pietzsch, T., Preibisch, S., Rueden, C., Saalfeld, S., Schmid, B., et al. (2012). Fiji: an open-source platform for biological-image analysis. Nat. Methods *9*, 676–682.

96. Choi, H.M.T., Schwarzkopf, M., Fornace, M.E., Acharya, A., Artavanis, G., Stegmaier, J., Cunha, A., and Pierce, N.A. (2018). Third-generation in situ hybridization chain reaction: multiplexed, quantitative, sensitive, versatile, robust. Development *145*. https://doi.org/10.1242/dev.165753.

97. Chaterji, S., Barik, A., and Sathyamurthy, A. (2021). Intraspinal injection of adeno-associated viruses into the adult mouse spinal cord. STAR Protoc. *2*, 100786.

98. Ayers, J.I., Fromholt, S., Sinyavskaya, O., Siemienski, Z., Rosario, A.M., Li, A., Crosby, K.W., Cruz, P.E., DiNunno, N.M., Janus, C., et al. (2015). Widespread and efficient transduction of spinal cord and brain following neonatal AAV injection and potential disease modifying effect in ALS mice. Mol. Ther. *23*, 53–62.

99. Park, Y.G., Sohn, C.H., Chen, R., McCue, M., Yun, D.H., Drummond, G.T., Ku, T., Evans, N.B., Oak, H.C., Trieu, W., et al. (2018). Protection of tissue physicochemical properties using polyfunctional crosslinkers. Nat. Biotechnol. https://doi.org/10.1038/nbt.4281.

100. Yun, D.H., Park, Y.-G., Cho, J.H., Kamentsky, L., Evans, N.B., Albanese, A., Xie, K., Swaney, J., Sohn, C.H., Tian, Y., et al. (2019). Ultrafast immunostaining of organ-scale tissues for scalable proteomic phenotyping. bioRxiv, 660373. https://doi.org/10.1101/660373.

101. Kim, S.Y., Cho, J.H., Murray, E., Bakh, N., Choi, H., Ohn, K., Ruelas, L., Hubbert, A., McCue, M., Vassallo, S.L., et al. (2015). Stochastic electrotransport selectively enhances the transport of highly electromobile molecules. Proc. Natl. Acad. Sci. U. S. A. *112*, E6274-83.

102. Murray, E., Cho, J.H., Goodwin, D., Ku, T., Swaney, J., Kim, S.Y., Choi, H., Park, Y.G., Park, J.Y., Hubbert, A., et al. (2015). Simple, Scalable Proteomic Imaging for High-Dimensional Profiling of Intact Systems. Cell *163*, 1500–1514.

103. Wang, Q., Ding, S.L., Li, Y., Royall, J., Feng, D., Lesnar, P., Graddis, N., Naeemi, M., Facer, B., Ho, A., et al. (2020). The Allen Mouse Brain Common Coordinate Framework: A 3D Reference Atlas. Cell *181*, 936-953 e20.

104. Shelhamer, E., Long, J., and Darrell, T. (2016). Fully convolutional networks for semantic segmentation. IEEE Trans. Pattern Anal. Mach. Intell. *39*, 640–651.

105. Ronneberger, O., Fischer, P., and Brox, T. (2015). U-net: Convolutional networks for biomedical image segmentation (Springer).

106. He, K., Zhang, X., Ren, S., and Sun, J. (2016). Deep residual learning for image recognition.

Figure Legends

Figure 1. **Genetic strategy for differential targeting of *Fezf2*$^{+}$ ET^{d} and ET^{i} PNs in the same mouse**.

(A) Schematic of *Fezf2-tTA-CreER (FezF2TC)* knockin allele where a *frt-tTA-frt-CreER* cassette was inserted in frame before the STOP codon of *Fezf2* gene. In *FezfTC;Tbr2-Flp* double-allele mice, dNG-derived ET^{d} express *tTA* while iNG-derived ET^{i} express *CreER*, as *tTA* is removed by *Tbr2-Flp* in IPs. Postnatal injection of *AAV-TRE-GFP* and *AAV-FLEX-RFP* in cortex differentially label ET^{d} and ET^{i}, respectively.

(B) Cortex wide labelling of ET^{d} and ET^{i} neurons through retro-orbital co-injections of *AAVPHP.eB-TRE-EGFP* and *AAVPHP.eB-FLEX-tdTomato* in *FezfTC;Tbr2-Flp* mice.

(C) Schematic of stereotactic AAV injection to label ET^d and ET^i using *FezF2-TC;Tbr2Flp* mice in the RFO, BAR, and VIS. Labeled ET neurons across the three areas consist of 24% ET^d and 76% ET^i.

(C1-C3) Focal labelling of ET^d (red) and ET^i (green) in RFO (C1) BAR (C2), and VIS (C3). Significantly more number of ET^i than ET^d neurons were labelled in all three areas (bottom panels).

Abbreviations: RFO – rostral forelimb orofacial area in motor cortex; BAR – barrel cortex; VIS – visual cortex; dNG – direct neurogenesis; iNG - indirect neurogenesis; ET^d – direct neurogenesis generated extratelencephalic neuron; ET^i – indirect neurogenesis generated extratelencephalic neuron; RG - radial glia; IP – intermediate progenitor. Scatter points in bar plots indicate individual data points. Error bars indicate SD. Statistical tests used two-sample t-tests (p-values: *p < 0.05, n.s = not significant) Scalebars in (B) 1 mm (C1-C3) 500 µm.

Figure 2. Amplification, diversification and innovation of ET^i over ET^d subclasses

(A-D) Retrograde labelling of ET^d (red) and ET^i (green) from superior colliculus (A), pontine nuclei (B), medulla (C), and cervical spinal cord (D). Injection schematics are in top left. Pie charts show the overall proportion of labeled ET^d and ET^iacross isocortex for each injection site. Bottom row shows the 3D rendering of the distribution of labelled ET^d and ET^ineurons across isocortex. Green arrows indicate example areas with both ET^d and ET^i; red arrows indicate example areas with significantly more or entirely ET^i.

(E-H) Retrogradely labelled ET^d and ET^i for (E) colliculus-projecting, (F) pons-projecting, (G) medullary-projecting and (H) spinal-projecting neurons across the isocortex.

(I-L) Left panels: Bar plots showing that the number of retrogradely labeled ET^i is significantly larger than that of ET^dacross isocortex from each of the four injection sites. Right panels: Paired bar plots comparing the expected proportions of ET^d and ET^i (based on their approximate overall 1:3 cell number ratio) to the actual labelled proportions for each injection site. There is a significant increase in the proportion of actual ET^i over expected ET^i for all 4 injection sites. On the other hand, there is a significant decrease of proportion of actual ET^d over expected ET^d.

(M-O) Bar plots of retrogradely labelled ET neuron numbers for areas with exclusively ET^i and no ET^d from pontine (M), medullary (N), and spinal (O) injections, suggesting the innovation of novel ET^i over ET^d projection types in these areas. Note the abundance of sensory (brown font) and higher order (blue font) areas. There were no areas with exclusively ET^i labeling from collicular injection.

(P) Schematic representing amplification, diversification and innovation of ET subclasses by iNG. Amplification is simple generation of copies of ET^d by ET^i; Diversification is generation of distinct projection subclasses by ET^i while innovation reflects generation of novel projection classes which are exclusively ET^i.

Abbreviations: BG – basal ganglia; Th – thalamus; SC – superior colliculus; PONS – pontine nuclei; SpC – spinal cord. For abbreviations in (M-O) see Table S1. Scatter points in bar plots indicate individual data. Filled markers indicate ipsilateral and open markers indicate contralateral data.Error bars indicate SD. Statistical tests used: two-sample t-tests (p-values: *p < 0.05, ****p < 0.0001, n.s = not significant) Scalebars in (E-H, top panels) 1 mm (E-H, bottom panels) 500 µm.

Figure 3. Amplification and diversification of ET^i over ET^d projections from motor areas.

(A-C). Schematic of anterograde AAV injection site and 3D rendering in the sagittal plane for ET^d and ET^i axonal projections from (RFO, A), (CFA, B) and (MOs, C). White circles indicate injection sites. Black arrows indicate examples of greatly expanded ET^i projections to more distal targets.

(D-F). Heatmaps showing normalized percent occupation of target structures across the brain from ET^d and ET^i for ipsilateral and contralateral sides of the injection sites for RFO (D) CFA (E) MOs (F). White arrows indicate example areas with significant increase in percent occupation by ET^i over ET^d. Note the substantial increase of ET^i projections to several brainstem areas and the pyramidal tract.

(G-I). Schematics showing the amplification and diversification of ET^i over ET^d neurons and projections from the three motor areas scaled to the proportion of ET^d and ET^i labelled at the injection sites. Note the significantly expanded ET^i projections to the BG (action selection), and medulla and SpC (action diversification and execution) areas while having similar projections as ET^d to thalamus.

Abbreviations: RFO – rostral forelimb orofacial area in the motor cortex; CFA – caudal forelimb area; MOs – secondary motor area; BG – basal ganglia; SpC – spinal cord. For abbreviations in (D-F) see Table S1.

Figure 4. Amplification, diversification and innovation of ET^i over ET^d projections from sensory areas.

(A-C). Schematic of anterograde AAV injection site and 3D rendering in the sagittal plane for ET^d and ET^i axonal projections from (VIS, A), (AUD, B) and (BAR, C). White circles indicate injection sites. Black arrows indicate examples of greatly expanded ET^i projections to more distal targets.

(D-F). Heatmaps showing normalized percent occupation of target structures across the brain from ET^d and ET^i for both ipsilateral and contralateral sides of the injection sites for VIS (D) AUD (E), and BAR (D). White arrows indicate example areas with significant increase in percent occupation by ET^i over ET^d. Note the increased or exclusive projections to PONS from ET^i in all three areas while similar increased projections to medulla from ET^i from BAR.

(G-I). Schematics showing the amplification and diversification of ET^i over ET^d neurons and projections from the three sensory areas scaled to the proportion of ET^d and ET^i labelled at the injection sites. Note that the corticopontine projections are almost exclusively ET^i projections and the massive ET^i elaboration to lemniscal centers. There is also an expansion of ET^i projections to medulla and SpC, similar to motor areas from BAR.

Abbreviations: VIS – visual cortex; AUD – auditory cortex; BAR – barrel cortex; PONS – pontine nuclei; SpC – spinal cord. For abbreviations in (D-F) see Table S1.

Figure 5. Amplification, diversification and innovation of ET^i over ET^d projections from higher order areas.

(A-B). Schematic of AAV injection site and 3D renderings in the sagittal plane for ET^d and ET^i axonal projections from (PFC, A) and (PAR, B). White circles indicate injection sites. Black arrows indicate examples of greatly expanded ET^i projections to more distal targets.

(C-D). Heatmaps showing normalized percent occupation of target structures across the brain from ET^d and ET^i for both ipsilateral and contralateral sides of the injection sites for PFC (C) and PAR (D). White arrows indicate example areas with significant increase in percent occupation by ET^i over ET^d. Note the significantly increased ET^i projections to hypothalamus, other pallial areas and the brainstem, while similar projections as ET^d in the thalamus from PFC. For PAR note the increased ET^i projections to BG and brainstem areas.

(E-F). Schematics showing the amplification and diversification of ET^i over ET^d neurons and projections from PFC and PAR scaled to the proportion of ET^d and ET^i labelled at the injection sites. Note the expansion of ET^i projections to neuromodulatory, hypothalamic and other pallial areas while having similar proportions as ET^d to the epithalamus from PFC. Note motor-like expansion of ET^i projections to BG and medulla/SpC from PAR.

Abbreviations: PFC – prefrontal cortex; PAR – parietal cortex; BG – basal ganglia; SpC – spinal cord. For abbreviations in (C-D) see Table S1.

Figure 6. Selective axon pruning in ET^i but not ET^d neuron during early postnatal development shapes the areal distribution of ET^i

(A-B) 3D renderings of retrogradely labelled ET^d (red) and ET^i (green) spinal projecting neurons/nuclei across isocortex from retrograde AAV injections into the cervical spinal cord of P28-P40 (A) and P4-P40 (B) mice.

(C-D) Retrogradely labelled ET^d and ET^i spinal projecting neurons (C) or nuclei (D) from cSpC injections in P28-P40 (C) and P4-P40 (D) mice. Scale bars: 1 mm in top and 500um in bottom panels.

(E-F) Bar plots showing number of retrogradely labelled ET^d (red) and ET^i (green) spinal projecting neurons across different isocortical areas. Error bars represent standard deviations. Zoomed in views magnify selected areas (in dotted black rectangle) showing low ET^d numbers compared to ET^i. The zoomed ET^i bar plots are truncated to show ET^d cell numbers.

(G) Pie charts showing the proportion of ET^d and ET^i spinal projecting neurons across isocortex from injections into the cervical spinal cord of P28-P40 (left) P4-P40 (right) mice.

(H) Bar plots showing that the number of retrogradely labelled ET^i spinal projecting neurons is significantly larger than the number of ET^d spinal projecting neurons across isocortex from injections into cSpC of P4-P40 mice.

(I) Bar plots showing that number of ET^i spinal projecting neurons across isocortex from cSpC injections in P4-P40 mice is significantly more than that of cSpC injections in P28-P40 mice, while there is no significant change for ET^dspinal projecting neurons between the two.

(J) Paired bar plots comparing number of retrogradely labelled layer 5 spinal projecting neurons/nuclei in MOp, MOs, SSp-ll, SSp-ul, SSp-tr and SSs between P28-P40 and P4-P40 mice. The P4-P40 mice

had significantly more nuclei in MOp, MOs and SSs while there were no significant changes in other areas.

(K) Paired bar plots comparing number of retrogradely labelled layer 6 spinal projecting neurons/nuclei in MOp, MOs, SSp-ll, SSp-ul, SSp-tr and SSs between P28-P40 and P4-P40 mice. The P4-P40 mice had significantly more nuclei in MOs and SSs while there were no significant changes in other areas.

(O) A schematic showing selective axon pruning in corticospinal ET^i but not ET^d neurons during early postnatal development more evident in mid and posterior areas of the isocortex , which shapes the projection patterns and areal distribution of ET^i in mature cortex.

Abbreviations: P28-P40 – mice with injections on P28 and harvested at P40; P4-P40 – mice with injections at P4 and harvested at P40; cSpC – cervical spinal cord. For abbreviations in (E-F, J-K) see Table S1. Error bars indicate SD. Scatter points indicate individual data.Filled markers indicate ipsilateral and open markers indicate contralateral data Statistical tests used: (H, J, K) two-sample t-test; (I) two-sample t-test and Mann-Whitney U test (p-values: *p < 0.05, **p < 0.01, ***p < 0.001,****p < 0.0001, n.s = not significant)

Figure 7. Optogenetic activation of ET^d and ET^i in the motor cortex reveal distinct roles in controlling movement

(A-C) Schematic showing experimental setup for head-fixed optogenetic activation (B) Schematic showing activation of ET^{all} in the RFO in *Fezf2CreERAi32* mice; ET^{all} neurons expressing channelrhodopsin (right). (B) Schematic showing activation ET^i and ET^d in the same *Fezf2Tbr2flp* miceRFO (left). ET^d is targeted with AAV8-TRE-ChRmine-oScarlet on the right RFO while ET^i is targeted with AAV8-FLEX-ChRmine-oScarlet on the left RFO.Labelling of ET^i and ET^d (right) showing expression of ChRmine (magenta) in the left and right RFO respectively.

(D) Contralateral forelimb trajectories during activation of ET^{all} (20 trials, left), ET^i (20 trials, middle) and ET^d (17 trials, right) in RFO with circles and squares indicating start and end points respectively. Thick line indicates the average trajectory. Note that forelimb movement was absent during ET^d activation.

(E) 2D projections of forelimb movement trajectories during optogenetic activation of ET^{all} (n = 6) and ET^i (n = 6) and ET^d (n = 4) . Thick line indicates the average position. Movement directions are indicated as: A, anterior; P, posterior; D, dorsal; V, ventral; M, medial; L, lateral.

(F) Bar plots showing no significant differences in distance travelled (left) and peak speed (right) upon optogenetic activation for the forelimb between ET^{all} (n = 6) and ET^i (n = 6) and significant differences between ET^d (n = 4) and ET^i (n = 6).

(G-H) Jaw movement trajectories during optogenetic activation (top blue bar) of ET^{all} (20 trials, left), ET^i (20 trials, middle) and ET^d (17 trials, right) and (H) across different mice for ET^{all} (n = 6), ET^i (n = 6) and ET^d (n = 4).

(I) Bar plots showing no significant differences in distance travelled (left) and peak speed (right) upon optogenetic activation for the jaw between ET^{all} (n = 6) and ET^{i} (n = 6) and significant differences between ET^{d} (n = 4) and ET^{i} (n = 6).

(J-J3) Illustrative schematics with corresponding movement trajectory plots of nose and contra/ipsi forelimb showing behavioural effects of optogenetic activation in free moving mice (single trial) in the RFO (preactivation, J) for ET^{all} (J1), ET^{i} (J2) and ET^{d} (J3). Note the significantly amplified nose movement and unique contralateral forelimb movement upon ET^{i} activation.

(K-L) Bar plots showing significant differences in distance travelled (left) and peak speed (right) upon optogenetic stimulation in free-moving mice for the nose (K) and forelimb (L) for ET^{all} (n = 4), ET^{i} (n = 5) and ET^{d} (n = 5).

(M) Plot showing change in hand to nose distance upon optogenetic activation of ET^{all} (n = 4), ET^{i} (n = 5) and ET^{d} (n = 5) in free-moving mice, with significantly higher changes in ET^{i} while that of ET^{d} is almost zero.

Abbreviations: RFO - Rostral forelimb orofacial area; Error-bars indicate SEM. Statistical tests used: Two-sided paired t-test or Two-sided Wilcoxon signed-rank test. p-values: *p < 0.05, **p < 0.01, ***p < 0.001. Movement trajectories were normalized to the start position in (D) and (E).Scalebars in (B) 500 µm, (C) 5 mm.

Figure 8. Schematic summary of the evolutionary origin and development impact of dNG and iNG that shape the amplification, diversification and innovation of corticofugal projection neurons.

While dNG evolved before the dawn of vertebrates, iNG emerged from amniotes and greatly expanded in mammals. In early vertebrates (left), the pallium does have a basic dNG-ET^{d} (red) efferent projection pattern from the pallium to downstream motor centers, in mammals (right), dNG-ET^{d} and the hugely expanded iNG-ET^{i} (green) are intermixed and form mosaic circuits. While dNG-ET^{d} largely targets conserved structures in the forebrain and midbrain, iNG-ET^{i} massively amplifies, diversifies and *innovates* projection classes to brainstem and spinal cord. Moreover, iNG-ET^{i} expands projections in an area specific manner (extreme right) reflected in the expanded projections to action selection, diversification and execution centers from the motor areas; to sensory processing centers along the lemniscal pathways from the sensory areas; and to neuromodulatory, hypothalamic and other pallial centers from higher order areas of the isocortex.

Abbreviations: dNG – direct neurogenesis; iNG - indirect neurogenesis; ET^{d} – direct neurogenesis generated extratelencephalic neuron; ET^{i} – indirect neurogenesis generated extratelencephalic neuron; MLR - mesencephalic locomotor region; RSN - reticulospinal neurons; TN - trigeminal nucleus; vlRN - ventro-lateral reticular nuc;eus; FMN - facial motor nucleus; LatRM - lateral rostral medulla; TSN - trigeminal sensory nucleus; SPN - spinal nucleus of the trigeminal; SpC – spinal cord.

Supplemental Figure Legends

Figure S1. Validation of the *FezFTC;Tbr2Flp* mice for viral access to capture ET^d and ET^i, Related to Figure 1.

(A) Schematic of strategy for validating the *FezF2-TC* line. Without the*Tbr2-Flp* allele *FezF2-TC* drives *tTA* expression in all *FezF2*+ neurons, which can be labelled by injection of *AAV-TRE-EGFP*.

(B-C) The vast majority of the EGFP-labelled neurons in the deep layers overlap with *in situ* detection of *FezF2* mRNA (red) verifying that they are *FezF2*+ (yellow).

(D-G) Strategy and result of checking for non-specific labelling for *AAV-TRE-EGFP*. Injection of *AAV9-TRE-EGFP* in *LSL-Flp* mice, which do not express tTA (D), did not result in prominent GFP expression. Faint GFP signals at the injection site (E) resulted from low level leakage of *TRE-EGFP* but did not label any corticofugal axons in pons (F) and medulla (G) even after antibody amplification of EGFP signal.

(H-I) Strategy and result for checking non-specific labelling for *AAV-CAG-FLEX-tdTomato*. We inject *AAV9-CAG-FLEX-tdTomato* together with *AAV9-TRE-EGFP* in *FezF2-TC* mice as in (A). All *FezF2*+ neurons are labelled with EGFP at the injection site. There is negligible labelling of *tdTomato, as* there is no *Cre* expression in the *FezF2-TC*, indicating that there is almost no leaky expression.

(J) (left) Schematic of a previous strategy wherein dNG and iNG can be simultaneously visualized by a genetic fate-mapping scheme using the IS2 reporter with *FezF2-CreER* (RG) and *Tbr2-Flp* (IP) drivers: dNG-ET^d (*Fezf2*$^+$/*Tbr2*-) is labeled by RFP through "Cre-NOT-Flp" subtraction; iNG-ET^i (*FezF2*$^+$/*Tbr2*$^+$) is labeled by EGFP through "Cre-AND-Flp" intersection (see[17]). (right) Overall proportions of ET^d and ET^i neurons from RFO, BAR and VIS areas was 1:3.

(K-M) (left) We compared sections from RFO (K), BAR (L) and VIS (M) corresponding to the sections in Figure 1C1-C3. (right) The number of ET^i neurons were significantly more than ET^d for RFO and BAR.

(N-N2) Comparing proportions of dNG-ET^d and iNG-ET^i labelled from the new and old strategies: viral targeting in *FezFTC;Tbr2Flp* in Figure 1A and *FezFTC;Tbr2Flp;IS2* in (J), showed no significant differences showing both strategies are comparable and consistent for (N) RFO, (N1) BAR and (N2) VIS.

Abbreviations: RFO – rostral forelimb orofacial area; BAR – barrel cortex; VIS – visual cortex; Error bars indicate SD. Scatter points indicate individual data. Statistical tests used: two-sample t-tests (p-values: *$p < 0.05$, **$p < 0.01$, n.s = not significant).Scalebars in (B,E,I) 500 µm (F,G) 1 mm.

Figure S2. ET^d and ET^i collicular-, pontine-, medulla- and spinal- projecting neurons. Related to Figure 2.

(A-D) Bar plots of retrogradely labelled ET^d (red) and ET^i (green) neuron numbers across different areas of the isocortex from collicular (A), pontine (B), medulla (C), and cervical spinal cord (D) injections. X-axis is shown in a Log_{10} scale.

(E) Correlation matrix heatmap showing pairwise Pearson correlations between number of retrogradely labelled $ET^d$and ET^i neurons across all areas of the isocortex from 2-3 mice each from collicular, pontine, medulla, and cervical spinal cord injections.

Abbreviations for all isocortical regions in (A-D) are listed in Table S1. Error-bars represent SEM.

Figure S3. Predominant ET^i over ET^d subcortical projections from RFO, Related to Figure 3

(A) AAV injection in the RFO labeled ET^d (red) and ET^i (green).

(A1) Left, location of the injection site shown on a schematic of the dorsal cortex. Right, pie chart of proportion of ET^d and ET^i neurons labelled at the injection site.

(A2) Bar plots of layer-wise counts of labelled ET^d and ET^i neurons in the injection site (n = 2 mice). Labelling is evident in deep layers including layer 6. *FezF2* is known to recruit *Tle4* to repress PT genes, and their co-expression in layer 6[80] likely explains their labeling.

(B) PT and CT fiber bundles with ET^d and ET^i projections from RFO. Notice both ET^d and ET^i projections in CT (arrowhead) while largely ET^i in PT (arrow).

(C) Dense ET^d and ET^i projections to the thalamus, including VPM/VPL.

(D) Dense ET^i but weak ET^d projections to the GPe.

(E) Stronger ET^i over ET^d projections to the superior colliculus.

(F) Strong ET^i but weak ET^d projections to the PONS.

(G) Strong ET^i but nearly no ET^d projections to the spinal cord.

(B1-G1) Scatter plots with linear regression of normalized fraction occupations of RFO ET^d and ET^i projections to target regions (B1) thalamus and brainstem, (C1) first order (FO) and higher order (HO) thalamus, (D1) basal ganglia, (E1) midbrain, (F1) PONS, (G1) medulla.

(B2-G2) Violin plots showing normalized percent occupation for RFO ET^d and ET^i projections with the star indicating the median and black circles showing individual values for subregions within target regions of (B2) thalamus and brainstem (C2) first order (FO) and higher order (HO) thalamus (D2) basal ganglia (E2) midbrain (F2) PONS (G2) medulla.

(B3-G3) Box plots of Z-score normalized percent occupation differences between ET^i and ET^d projections from RFO to (B3) thalamus and brainstem, (C3) first order (FO) and higher order (HO) thalamus, (D3) basal ganglia, (E3) midbrain, (F3) PONS, (G3) medulla. p-values reflect significant within region differences.

(H) Box plots of Z-score normalized percent occupation differences between ET^i and ET^d projections from RFO for brainstem, midbrain, PONS, medulla and BG with post-hoc comparisons to thalamus, following a multiple comparisons test ($p < 0.05$) to assess statistical differences among different projection target regions. The brainstem, medulla and BG regions showed significantly more iNG-ET^i projections than thalamus.

(I) Correlation matrix heatmap showing pairwise Pearson correlations between ET^d and ET^i normalized fraction occupation across all areas for projections from RFO across two mice used for LightSheet Imaging.

Abbreviations: RFO – rostral forelimb orofacial area; FO – first order thalamic nuclei; HO- higher order thalamic nuclei; VPM – ventral posterior medial nucleus; VPL – ventral posterior lateral nucleus; PO – posterior thalamic nucleus GPe- Globus pallidus externa; PONS – pontine nuclei; BG – basal ganglia. Subregions for each target region are listed in Table S1. Scatter points in scatter plots, violin plots and box plots represent individual subregion percent occupation (normalized or raw) values, with filled markers for ipsilateral and open markers for contralateral data. Regression lines indicate overall correlation trends. Dotted grey line indicates the line of equality. Interquartile range in box plots is 25th–75th percentiles. Statistical tests used one-sample t-test, Wilcoxon signed-rank test, Kruskal–Wallis test, Wilcoxon rank-sum test and Kolmogorov-Smirnov test (p-values: *$p < 0.05$, **$p < 0.01$, ***$p < 0.001$, ****$p < 0.0001$, n.s = not significant) Scalebars in (A-F) 1 mm; (G, A right, B right) 500 µm; (C right, E right, F right) 200 µm; (D right, G right) 100 µm.

Figure S4. Predominant ET^i over ET^d subcortical projections from CFA, Related to Figure 3

(A) AAV injection in the CFA labelling ET^d (red) and ET^i (green).

(A1) (left) Location of the injection site shown on a schematic of dorsal cortex. (right) Pie chart of proportion of $ET^d$and ET^i neurons labelled at the injection site.

(A2) Bar plots of layer-wise counts of labelled ET^d and ET^i neurons in the injection site (n = 2 mice).

(B) PT and CT fiber bundles with ET^d and ET^i projections from CFA. Notice both ET^d and ET^i projections in CT (arrowhead) while largely ET^i in PT (arrow).

(C) Dense ET^d and ET^i projections to the thalamus, including VPM.

(D) Dense ET^i but weak ET^d projections to the SNr.

(E) Stronger ET^i over ET^d projections to the superior colliculus.

(F) Strong ET^i but weak ET^d projections to the PONS.

(G) Strong ET^i but nearly no ET^d projections to the spinal cord.

(B1-G1) Scatter plots with linear regression of normalized fraction occupations of CFA ET^d and ET^i projections to target regions (B1) thalamus and brainstem, (C1) first order (FO) and higher order (HO) thalamus, (D1) basal ganglia, (E1) midbrain, (F1) PONS, (G1) medulla.

(B2-G2) Violin plots showing normalized percent occupation for CFA ET^d and ET^i projections with the Star indicating the median and black circles showing individual values for subregions within target regions of (B2) thalamus and brainstem (C2) first order (FO) and higher order (HO) thalamus (D2) basal ganglia (E2) midbrain (F2) PONS (G2) medulla.

(B3-G3) Box plots of Z-score normalized percent occupation differences between ET^i and ET^d projections from CFA to (B3) thalamus and brainstem, (C3) first order (FO) and higher order (HO) thalamus, (D3) basal ganglia, (E3) midbrain, (F3) PONS, (G3) medulla. p-values reflect significant within region differences.

(H) Box plots of Z-score normalized percent occupation differences between ET^i and ET^d projections from CFA for brainstem, midbrain, PONS, medulla and BG with post-hoc comparisons to thalamus, following a multiple comparisons test ($p < 0.0001$) to assess statistical differences among different projection target regions. The brainstem, PONS, medulla and BG regions showed significantly more iNG-ET^i projections than thalamus.

(I) Correlation matrix heatmap showing pairwise Pearson correlations between ET^d and ET^i normalized fraction occupation across all areas for projections from CFA across two mice used for LightSheet Imaging.

Abbreviations: CFA – caudal forelimb area; FO – first order thalamic nuclei; HO- higher order thalamic nuclei; VPM – ventral posterior medial nucleus; PO – posterior thalamic nucleus SNr – substantia nigra *pars reticulata*; PONS – pontine nuclei; BG – basal ganglia. Subregions for each target region are listed in Table S1. Scatter points in scatter plots, violin plots and box plots represent individual subregion percent occupation (normalized or raw) values, with filled markers for ipsilateral and open markers for contralateral data. Regression lines indicate overall correlation trends. Dotted grey line indicates the line of equality. Interquartile range in box plots is 25th–75th percentiles. Statistical tests used one-sample t-test, Wilcoxon signed-rank test, Kruskal–Wallis test, Wilcoxon rank-sum test and Kolmogorov-Smirnov test (p-values: *$p < 0.05$, **$p < 0.01$, ***$p < 0.001$, ****$p < 0.0001$, n.s = not significant) Scalebars in (A-F) 1 mm; (G, A-B right) 500 µm; (C right, E right, G right) 250 µm; (D right, F right) 200 µm.

Figure S5. Predominant ET^i over ET^d subcortical projections from MOs, Related to Figure 3

(A) AAV injection in the MOs labeled ET^d (red) and ET^i (green).

(A1) Left, location of the injection site shown on a schematic of dorsal cortex. Right, pie chart of proportion of ET^d and ET^i neurons labelled at the injection site.

(A2) Bar plots of layer-wise counts of labelled ET^d and ET^i neurons in the injection site (n = 2 mice).

(B) PT and CT fiber bundles with ET^d and ET^i projections from MOs. Notice both ET^d and ET^i projections in CT (arrowhead) while largely ET^i in PT (arrow).

(C) Dense ET^d and ET^i projections to the thalamus, including PO/PCN.

(D) Dense ET^i but weak ET^d projections to the GPi.

(E) Stronger ET^i over ET^d projections to the superior colliculus.

(F) Strong ET^i but weak ET^d projections to the PONS.

(G) Strong ET^i but nearly no ET^d projections to the spinal cord.

(B1-G1) Scatter plots with linear regression of normalized fraction occupations of MOs ET^d and ET^i projections to target regions (B1) thalamus and brainstem, (C1) first order (FO) and higher order (HO) thalamus, (D1) basal ganglia, (E1) midbrain, (F1) PONS, (G1) medulla.

(B2-G2) Violin plots showing normalized percent occupation for MOs ET^d and ET^i projections with the Star indicating the median and black circles showing individual values for subregions within target regions of (B2) thalamus and brainstem (C2) first order (FO) and higher order (HO) thalamus (D2) basal ganglia (E2) midbrain (F2) PONS (G2) medulla.

(B3-G3) Box plots of Z-score normalized percent occupation differences between ET^i and ET^d projections from MOs to (B3) thalamus and brainstem, (C3) first order (FO) and higher order (HO) thalamus, (D3) basal ganglia, (E3) midbrain, (F3) PONS, (G3) medulla. p-values reflect significant within region differences.

(H) Box plots of Z-score normalized percent occupation differences between ET^i and ET^d projections from MOs for brainstem, midbrain, PONS, medulla and BG with post-hoc comparisons to thalamus, following a multiple comparisons test ($p < 0.01$) to assess statistical differences among different projection target regions. The brainstem, PONS, medulla and BG regions showed significantly more iNG-ET^i projections than thalamus.

(I) Correlation matrix heatmap showing pairwise Pearson correlations between ET^d and ET^i normalized fraction occupation across all areas for projections from MOs across two mice used for LightSheet Imaging.

Abbreviations: MOs – secondary motor area; FO – first order thalamic nuclei; HO- higher order thalamic nuclei; VPM – ventral posterior medial nucleus; VPL – ventral posterior lateral nucleus; PO – posterior thalamic nucleus; GPi – globus pallidus interna; PONS – pontine nuclei; BG – basal ganglia. Subregions for each target region are listed in Table S1. Scatter points in scatter plots, violin plots and box plots represent individual subregion percent occupation (normalized or raw) values, with filled markers for ipsilateral and open markers for contralateral data. Regression lines indicate overall correlation trends. Dotted grey line indicates the line of equality. Interquartile range in box plots is 25th–75th percentiles. Statistical tests used: one-sample t-test, Wilcoxon signed-rank test, Kruskal–Wallis test, Wilcoxon rank-sum test and Kolmogorov-Smirnov test (p-values: *$p < 0.05$, **$p < 0.01$, ***$p < 0.001$, ****$p < 0.0001$, n.s = not significant) Scalebars in (A-G) 1 mm; (A-B right, D-F right) 500 µm; (C right) 250 µm; (G right) 100 µm.

Figure S6. Predominant ET^i over ET^d subcortical projections from VIS, Related to Figure 4

(A) AAV injection in the VIS labeled ET^d (yellow) and ET^i (magenta).

(A1) Left, location of the injection site shown on a schematic of dorsal cortex. Right, pie chart of proportion of ET^d and ET^i neurons labelled at the injection site.

(A2) Bar plots of layer-wise counts of labelled ET^d and ET^i neurons in the injection site (n = 2 mice).

(B) PT and CT fiber bundles with ET^d and ET^i projections from VIS. Notice both ET^d and ET^i projections in CT (arrowhead) while largely ET^i in PT (arrow).

(C) Dense ET^d and ET^i projections to the thalamus, including LGd/LGv.

(D) Stronger ET^i over ET^d projections to the superior colliculus.

(E) Strong ET^i but nearly no ET^d projections to the PONS.

(B1-E1) Scatter plots with linear regression of normalized fraction occupations of VIS ET^d and ET^i projections to target regions (B1) thalamus and brainstem, (C1) first order (FO) and higher order (HO) thalamus, (D1) midbrain, (E1) PONS.

(B2-E2) Violin plots showing normalized percent occupation for VIS ET^d and ET^i projections with the star indicating the median and black circles showing individual values for subregions within target regions of (B2) thalamus and brainstem, (C2) first order (FO) and higher order (HO) thalamus, (D2) midbrain, (E2) PONS.

(B3-E3) Box plots of Z-score normalized percent occupation differences between ET^i and ET^d projections from VIS to (B3) thalamus and brainstem, (C3) first order (FO) and higher order (HO) thalamus, (D3) midbrain, (E3) PONS. p-values reflect significant within region differences.

(F) Box plots of Z-score normalized percent occupation differences between ET^i and ET^d projections from VIS for brainstem, midbrain and PONS with post-hoc comparisons to thalamus, following a multiple comparisons test ($p < 0.01$) to assess statistical differences among different projection target regions. There were no significant differences between target regions.

(G) Correlation matrix heatmap showing pairwise Pearson correlations between ET^d and ET^i normalized fraction occupation across all areas for projections from VIS across two mice used for LightSheet Imaging.

Abbreviations: VIS - visual cortex; FO – first order thalamic nuclei; HO- higher order thalamic nuclei; LGd - lateral geniculate dorsal; LGv – lateral geniculate ventral; PONS – pontine nuclei. Subregions for each target region are listed in Table S1. Scatter points in scatter plots, violin plots and box plots represent individual subregion percent occupation (normalized or raw) values, with filled markers for ipsilateral and open markers for contralateral data. Regression lines indicate overall correlation trends. Dotted grey line indicates the line of equality. Interquartile range in box plots is 25th–75th percentiles. Statistical tests used one-sample t-test, Wilcoxon signed-rank test, Kruskal–Wallis test, Wilcoxon rank-sum test and Kolmogorov-Smirnov test (p-values: *$p < 0.05$, **$p < 0.01$, ***$p < 0.001$, ****$p < 0.0001$, n.s = not significant) Scalebars in (A-E) 1 mm; (A-B right, D right) 500 µm; (C right) 250 µm; (E right) 200 µm.

Figure S7. Predominant ET^i over ET^d subcortical projections from AUD, Related to Figure 4

(A) AAV injection in the AUD labeled ET^d (red) and ET^i (green).

(A1) (left) Location of the injection site shown on a schematic of dorsal cortex. (right) Pie chart of proportion of $ET^d$and ET^i neurons labelled at the injection site.

(A2) Bar plots of layer-wise counts of labelled ET^d and ET^i neurons in the injection site (n = 2 mice).

(B) PT and CT fiber bundles with ET^d and ET^i projections from AUD. Notice both ET^d and ET^i projections in CT (arrowhead) while largely ET^i in PT (arrow).

(C) Dense ET^d and ET^i projections to the thalamus, including MGv.

(D) Dense ET^i but weak ET^d projections to the NLLv.

(E) Stronger ET^i over ET^d projections to the inferior colliculus.

(F) Strong ET^i but weak ET^d projections to the PONS.

(G) Sparse ET^i but nearly no ET^d projections to the CN.

(B1-G1) Scatter plots with linear regression of normalized fraction occupations of AUD ET^d and ET^i projections to target regions (B1) thalamus and brainstem, (C1) first order (FO) and higher order (HO) thalamus, (D1) lemniscal sensory areas, (E1) midbrain, (F1) PONS, (G1) medulla.

(B2-G2) Violin plots showing normalized percent occupation for AUD ET^d and ET^i projections with the Star indicating the median and black circles showing individual values for subregions within target regions of (B2) thalamus and brainstem (C2) first order (FO) and higher order (HO) thalamus (D2) lemniscal sensory areas (E2) midbrain (F2) PONS (G2) medulla.

(B3-G3) Box plots of Z-score normalized percent occupation differences between ET^i and ET^d projections from AUD to (B3) thalamus and brainstem, (C3) first order (FO) and higher order (HO) thalamus, (D3) lemniscal sensory areas (E3) midbrain, (F3) PONS, (G3) medulla. p-values reflect significant within region differences.

(H) Box plots of Z-score normalized percent occupation differences between ET^i and ET^d projections from AUD for brainstem, midbrain, PONS, medulla and lemniscal sensory areas with post-hoc comparisons to thalamus, following a multiple comparisons test ($p < 0.01$) to assess statistical differences among different projection target regions. The PONS and lemniscal sensory areas showed significantly more iNG-ET^i projections than thalamus.

(I) Correlation matrix heatmap showing pairwise Pearson correlations between ET^d and ET^i normalized fraction occupation across all areas for projections from AUD across two mice used for LightSheet Imaging.

Abbreviations: AUD – auditory cortex; FO – first order thalamic nuclei; HO- higher order thalamic nuclei; MGv – medial geniculate ventral; NLLv - nucleus of the lateral lemniscus ventral; PONS – pontine nuclei; BG – basal ganglia. Subregions for each target region are listed in Table S1. Scatter points in scatter plots, violin plots and box plots represent individual subregion percent occupation (normalized or raw) values, with filled markers for ipsilateral and open markers for contralateral data. Regression lines indicate overall correlation trends. Dotted grey line indicates the line of equality. Interquartile range in box plots is 25th–75th percentiles. Statistical tests used one-sample t-test, Wilcoxon signed-rank test, Kruskal–Wallis test, Wilcoxon rank-sum test and Kolmogorov-Smirnov test (p-values: *$p < 0.05$, **$p < 0.01$, ***$p < 0.001$, ****$p < 0.0001$, n.s = not significant) Scalebars in (A-G) 1 mm; (A-B right) 500 µm; (C right, E-G right) 200 µm; (D right) 100 µm.

Figure S8. Predominant ET^i over ET^d subcortical projections from BAR, Related to Figure 4

(A) AAV injection in the BAR labeled ET^d (red) and ET^i (green).

(A1) (left) Location of the injection site shown on a schematic of the dorsal cortex. (right) Pie chart of proportion of $ET^d$and ET^i neurons labelled at the injection site.

(A2) Bar plots of layer-wise counts of labelled ET^d and ET^i neurons in the injection site (n = 2 mice).

(B) PT and CT fiber bundles with ET^d and ET^i projections from BAR. Notice both ET^d and ET^i projections in CT (arrowhead) while largely ET^i in PT (arrow).

(C) Dense ET^d and ET^i projections to the thalamus, including VPL/VPM/PO.

(D) Dense ET^i but weak ET^d projections to the inferior colliculus/PSV.

(E) Stronger ET^i over ET^d projections to the superior colliculus.

(F) Strong ET^i but weak ET^d projections to the PONS.

(G) Strong ET^i but weak ET^d projections to the PARN.

(B1-G1) Scatter plots with linear regression of normalized fraction occupations of BAR ET^d and ET^i projections to target regions (B1) thalamus and brainstem, (C1) first order (FO) and higher order (HO) thalamus, (D1) lemniscal sensory areas, (E1) midbrain, (F1) PONS, (G1) medulla.

(B2-G2) Violin plots showing normalized percent occupation for BAR ET^d and ET^i projections with the Star indicating the median and black circles showing individual values for subregions within target regions of (B2) thalamus and brainstem (C2) first order (FO) and higher order (HO) thalamus (D2) lemniscal sensory areas (E2) midbrain (F2) PONS (G2) medulla.

(B3-G3) Box plots of Z-score normalized percent occupation differences between ET^i and ET^d projections from BAR to (B3) thalamus and brainstem, (C3) first order (FO) and higher order (HO) thalamus, (D3) lemniscal sensory areas (E3) midbrain, (F3) PONS, (G3) medulla. p-values reflect significant within region differences.

(H) Box plots of Z-score normalized percent occupation differences between ET^i and ET^d projections from BAR for brainstem, midbrain, PONS, medulla and lemniscal sensory areas with post-hoc comparisons to thalamus, following a multiple comparisons test ($p < 0.0001$) to assess statistical differences among different projection target regions. The brainstem, midbrain, PONS, medulla and lemniscal sensory areas showed significantly more iNG-ET^i projections than thalamus.

(I) Correlation matrix heatmap showing pairwise Pearson correlations between ET^d and ET^i normalized fraction occupation across all areas for projections from BAR across two mice used for LightSheet Imaging.

Abbreviations: BAR – barrel cortex; FO – first order thalamic nuclei; HO- higher order thalamic nuclei; VPM – ventral posterior medial nucleus; VPL – ventral posterior lateral nucleus; PO – posterior thalamic nucleus; PONS – pontine nuclei; PSV – principal sensory nucleus of the trigeminal. Subregions for each target region are listed in Table S1. Scatter points in scatter plots, violin plots and

box plots represent individual subregion percent occupation (normalized or raw) values, with filled markers for ipsilateral and open markers for contralateral data. Regression lines indicate overall correlation trends. Dotted grey line indicates the line of equality. Interquartile range in box plots is 25th–75th percentiles. Statistical tests used one-sample t-test, Wilcoxon signed-rank test, Kruskal–Wallis test, Wilcoxon rank-sum test and Kolmogorov-Smirnov test (p-values: *p < 0.05, **p < 0.01, ***p < 0.001, ****p < 0.0001, n.s = not significant) Scalebars in (A-G) 1 mm; (B right) 500 µm; (A right, C-F right) 200 µm; (G right) 100 µm.

Figure S9. Predominant ET^i over ET^d subcortical projections from PFC, Related to Figure 5

(A) AAV injection in the PFC labeled ET^d (red) and ET^i (green).

(A1) (left) Location of the injection site shown on a schematic of dorsal cortex. (right) Pie chart of proportion of $ET^d$and ET^i neurons labelled at the injection site.

(A2) Bar plots of layer-wise counts of labelled ET^d and ET^i neurons in the injection site (n = 2 mice).

(B) PT and CT fiber bundles with ET^d and ET^i projections from PFC. Notice both ET^d and ET^i projections in CT (arrowhead) while largely ET^i in PT (arrow).

(C) Dense ET^d and ET^i projections to the thalamus, including AV/AL/MD.

(D) Dense ET^i but weak ET^d projections to the olfactory tubercle.

(E) Similar ET^i and ET^d projections to the epithalamus.

(F) Strong ET^i but weak ET^d projections to the hypothalamus.

(G) Strong ET^i but weak ET^d projections to the NDB.

(H) Strong ET^i but weak ET^d projections to the superior colliculus.

(I) Strong ET^i but weak ET^d projections to the PONS.

(J) Strong ET^i but nearly no ET^d projections to the LDTN.

(B1-J1) Scatter plots with linear regression of normalized fraction occupations of PFC ET^d and ET^i projections to target regions (B1) thalamus and brainstem, (C1) first order (FO) and higher order (HO) thalamus, (D1) pallial areas, (E1) epithalamus, (F1) hypothalamus, (G1) neuromodulatory structures, (H1) midbrain, (I1) PONS, (J1) medulla.

(B2-J2) Violin plots showing normalized percent occupation for PFC ET^d and ET^i projections with the Star indicating the median and black circles showing individual values for subregions within target regions of (B2) thalamus and brainstem, (C2) first order (FO) and higher order (HO) thalamus, (D2) pallial areas, (E2) epithalamus, (F2) hypothalamus, (G2) neuromodulatory structures, (H2) midbrain, (I2) PONS, (J2) medulla.

(B3-J3) Box plots of Z-score normalized percent occupation differences between ET^i and ET^d projections from PFC to (B3) thalamus and brainstem, (C3) first order (FO) and higher order (HO) thalamus, (D3) pallial areas, (E3) epithalamus, (F3) hypothalamus, (G3) neuromodulatory structures, (H3) midbrain, (I2) PONS, (J3) medulla. p-values reflect significant within region differences.

(K) Box plots of Z-score normalized percent occupation differences between ET^i and ET^d projections from PFC for brainstem, pallium, epithalamus, hypothalamus, neuromodulatory structures, midbrain, PONS and medulla with post-hoc comparisons to thalamus, following a multiple comparisons test ($p < 0.0001$) to assess statistical differences among different projection target regions. The brainstem, pallium, hypothalamus, neuromodulatory structures, midbrain, PONS and medulla areas showed significantly more iNG-ET^i projections than thalamus.

(L) Correlation matrix heatmap showing pairwise Pearson correlations between ET^d and ET^i normalized fraction occupation across all areas for projections from PFC across two mice used for LightSheet Imaging.

Abbreviations: PFC – prefrontal cortex; FO – first order thalamic nuclei; HO- higher order thalamic nuclei; VPM – ventral posterior medial nucleus; AV – anteroventral nucleus; AM – anteromedial nucleus; MD – mediodorsal nucleus of thalamus; NDB – nucleus of the diagonal band; LDTN – lateral dorsal tegmental nucleus; PONS – pontine nuclei. Subregions for each target region are listed in Table S1. Scatter points in scatter plots, violin plots and box plots represent individual subregion percent occupation (normalized or raw) values, with filled markers for ipsilateral and open markers for contralateral data. Regression lines indicate overall correlation trends. Dotted grey line indicates the line of equality. Interquartile range in box plots is 25th–75th percentiles. Statistical tests used one-sample t-test, Wilcoxon signed-rank test, Kruskal–Wallis test, Wilcoxon rank-sum test and Kolmogorov-Smirnov test (p-values: *$p < 0.05$, **$p < 0.01$, ***$p < 0.001$, ****$p < 0.0001$, n.s = not significant) Scalebars in (A-J) 1 mm; (B right) 500 µm; (A right, C-D right, F-J right) 200 µm; (E right) 100 µm.

Figure S10. Predominant ET^i over ET^d subcortical projections from PAR, Related to Figure 5

(A) AAV injection in the PAR labeled ET^d (red) and ET^i (green).

(A1) (left) Location of the injection site shown on a schematic of dorsal cortex. (right) Pie chart of proportion of $ET^d$and ET^i neurons labelled at the injection site.

(A2) Bar plots of layer-wise counts of labelled ET^d and ET^i neurons in the injection site (n = 2 mice).

(B) PT and CT fiber bundles with ET^d and ET^i projections from PAR. Notice both ET^d and ET^i projections in CT (arrowhead) while largely ET^i in PT (arrow).

(C) Dense ET^d and ET^i projections to the thalamus, including VPL/VPM/VA.

(D) Dense ET^i but weak ET^d projections to the GPe.

(E) Stronger ET^i over ET^d projections to the superior colliculus.

(F) Strong ET^i but weak ET^d projections to the PONS.

(G) Strong ET^i but nearly no ET^d projections to the spinal cord.

(B1-G1) Scatter plots with linear regression of normalized fraction occupations of PAR ET^d and ET^i projections to target regions (B1) thalamus and brainstem, (C1) first order (FO) and higher order (HO) thalamus, (D1) basal ganglia, (E1) midbrain, (F1) PONS, (G1) medulla.

(B2-G2) Violin plots showing normalized percent occupation for PAR ET^d and ET^i projections with the Star indicating the median and black circles showing individual values for subregions within target regions of (B2) thalamus and brainstem (C2) first order (FO) and higher order (HO) thalamus (D2) basal ganglia (E2) midbrain (F2) PONS (G2) medulla.

(B3-G3) Box plots of Z-score normalized percent occupation differences between ET^i and ET^d projections from PAR to (B3) thalamus and brainstem, (C3) first order (FO) and higher order (HO) thalamus, (D3) basal ganglia, (E3) midbrain, (F3) PONS, (G3) medulla. p-values reflect significant within region differences.

(H) Box plots of Z-score normalized percent occupation differences between ET^i and ET^d projections from PAR for brainstem, midbrain, PONS, medulla and BG with post-hoc comparisons to thalamus, following a multiple comparisons test ($p < 0.001$) to assess statistical differences among different projection target regions. The brainstem, PONS and medulla regions showed significantly more iNG-ET^i projections than thalamus.

(I) Correlation matrix heatmap showing pairwise Pearson correlations between ET^d and ET^i normalized fraction occupation across all areas for projections from PAR across two mice used for LightSheet Imaging.

Abbreviations: PAR – parietal cortex; FO – first order thalamic nuclei; HO- higher order thalamic nuclei; VPM – ventral posterior medial nucleus; VPL – ventral posterior lateral nucleus; VAL – ventral anterio-lateral complex of thalamus; GPe – globus pallidus externa; PONS – pontine nuclei; BG – basal ganglia. Subregions for each target region are listed in Table S1. Scatter points in scatter plots, violin plots and box plots represent individual subregion percent occupation (normalized or raw) values, with filled markers for ipsilateral and open markers for contralateral data. Regression lines indicate overall correlation trends. Dotted grey line indicates the line of equality. Interquartile range in box plots is 25th–75th percentiles. Statistical tests used one-sample t-test, Wilcoxon signed-rank test, Kruskal–Wallis test, Wilcoxon rank-sum test and Kolmogorov-Smirnov test (p-values: *$p < 0.05$, **$p < 0.01$, ***$p < 0.001$, ****$p < 0.0001$, n.s = not significant) Scalebars in (A-G) 1 mm; (B right) 500 µm; (G right) 400 µm; (A right,C-F right) 200 µm.

Figure S11. Developing ET^i neurons across cerebral cortical structures initially all project axons to the spinal cord. Related to Figure 6

(A-C) Spinal-projecting neurons retrogradely labelled from injections to cSpC of P4 mice and harvested at P40 (P4-P40) in (A) piriform cortex (B) BLA (C) Hippocampus – CA1 & subiculum. Note almost all of the labelled nuclei are ET^i.

(D) Correlation matrix heatmap showing pairwise Pearson correlations between ET^d and ET^i nuclei retrogradely labelled from cSpC in P4-P40 mice, across different non-isocortical pallial areas from two mice used for LightSheet Imaging.

(E) Bar plots of retrogradely labelled spinal-projecting ET^d (red) and ET^i (green) nuclei numbers across different non-isocortical pallial areas labelled from injections into cSpC in P4-P40 mice. Zoomed in sections (dotted black box) of the bar plots showing small to zero number of ET^d with the longer bar of ET^i which exceeds the zoomed scale truncated.

(F) Proportions of spinal-projecting ET^d (red) and ET^i (green) nuclei across different non-isocortical pallial areas in P4-P40 mice.

(G) Number of retrogradely labelled corticospinal ET^i are significantly more than ET^d across different non-isocortical pallial areas in P4-P40 mice.

(H) Sparse labelling of retrogradely labelled spinal-projecting ET^d and ET^i neurons in the isocortex from injections into cSpC in P1-P40 mice.

(I) Retrogradely labelled spinal-projecting ET^d and ET^i neurons in the isocortex and BLA from injections of generic retro-AAV into cSpC of P6 wildtype mice and harvested at P40 (P6-P40).

Abbreviations: BLA – basolateral amygdala; CA1 – Cornu Ammonis area 1; cSpC – cervical spinal cord. P1-P40 – injected in P1 and harvested at P40; P4-P40 – injected in P4 and harvested at P40; P28-P40 – injected in P28 and harvested at P40 Subregions in (E) are listed in Table S1. Statistical tests used: two-sample t-test, (p-values: ****$p < 0.0001$) Scalebars in (A-C, H-I) 1 mm; (C middle, H right) 500 µm; (B right, C right, I right) 200 µm.

Supplementary Videos

Supplementary Video 1. Whole-brain Lightsheet image stack of retrogradely labelled ET^d (red) and ET^i (green) neurons across the isocortex from injections into the superior colliculus(SC) in a FezF2TC;Tbr2Flp mouse.

Supplementary Video 2. Whole-brain Lightsheet image stack of retrogradely labelled ET^d (red) and ET^i (green) neurons across the isocortex from injections into the pontine nuclei (PONS) in a FezF2TC;Tbr2Flp mouse.

Supplementary Video 3. Whole-brain Lightsheet image stack of retrogradely labelled ET^d (red) and ET^i (green) neurons across the isocortex from injections into the medulla (MED) in a FezF2TC;Tbr2Flp.

Supplementary Video 4. Whole-brain Lightsheet image stack of retrogradely labelled ET^d (red) and ET^i (green) neurons across the isocortex from injections into the cervical spinal cord (cSpC) in a FezF2TC;Tbr2Flp mouse.

Supplementary Video 5. Whole-brain Lightsheet image stack of anterograde axonal projections of ET^d (red) and ET^i (green) neurons in the rostral forelimb orofacial area (RFO) of the isocortex in a FezF2TC;Tbr2Flp mouse.

Supplementary Video 6. Whole-brain Lightsheet image stack of anterograde axonal projections of ET^d (red) and ET^i (green) neurons in the caudal forelimb area (CFA) of the isocortex in a FezF2TC;Tbr2Flp mouse.

Supplementary Video 7. Whole-brain Lightsheet image stack of anterograde axonal projections of ET^d (red) and ET^i (green) neurons in the secondary motor area (MOs) of the isocortex in a FezF2TC;Tbr2Flp mouse.

Supplementary Video 8. Whole-brain Lightsheet image stack of anterograde axonal projections of ET^d (red) and ET^i (green) neurons in the visual cortex (VIS) in a FezF2TC;Tbr2Flp mouse.

Supplementary Video 9. Whole-brain Lightsheet image stack of anterograde axonal projections of ET^d (red) and ET^i (green) neurons in the auditory cortex (AUD) in a FezF2TC;Tbr2Flp mouse.

Supplementary Video 10. Whole-brain Lightsheet image stack of anterograde axonal projections of ET^d (red) and ET^i (green) neurons in the barrel cortex (BAR) in a FezF2TC;Tbr2Flp mouse.

Supplementary Video 11. Whole-brain Lightsheet image stack of anterograde axonal projections of ET^d (red) and ET^i (green) neurons in the prefrontal cortex (PFC) in a FezF2TC;Tbr2Flp mouse.

Supplementary Video 12. Whole-brain Lightsheet image stack of anterograde axonal projections of ET^d (red) and ET^i (green) neurons in the parietal cortex (PAR) in a FezF2TC;Tbr2Flp mouse.

Supplementary Video 13. Whole-brain Lightsheet image stack of retrogradely labelled ET^d (red) and ET^i(green) nuclei across different cortical/pallial areas from injections into the cervical spinal cord (cSpC) of a P4 FezF2TC;Tbr2Flp mouse and harvested at P40 (P4-P40).

Supplementary Video 14. Behavioural effects of optogenetic activation of ET^{all},ET^d and ET^i in the RFO shown sequentially in both the head-fixed and free moving conditions.

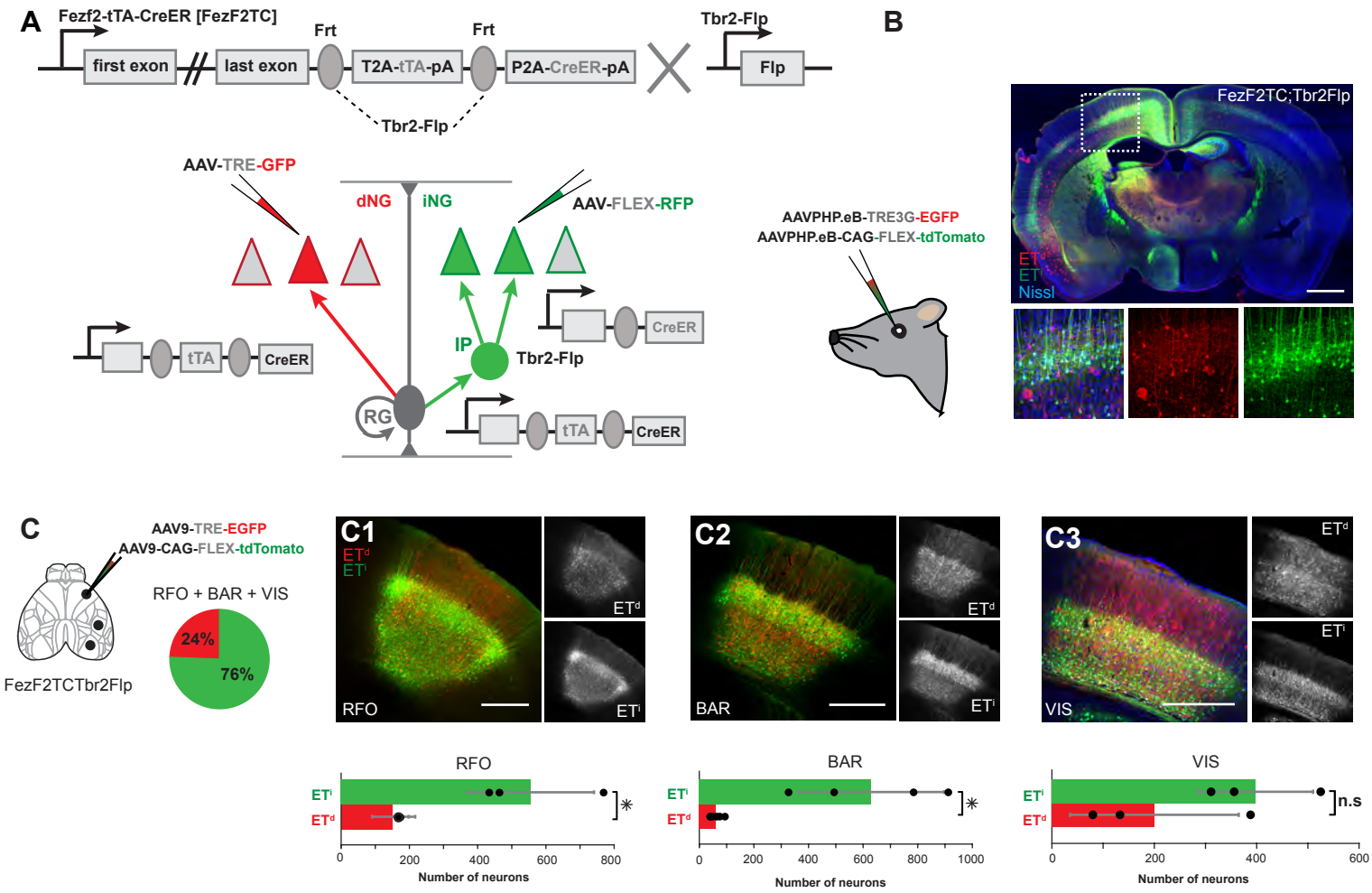
A
Fezf2-tTA-CreER [FezF2TC]
first exon
last exon
Frt
Frt
T2A-tTA-pA
P2A-CreER-pA
Tbr2-Flp
Tbr2-Flp
Flp
B
AAV-TRE-GFP
dNG
iNG
AAV-FLEX-RFP
tTA
CreER
IP
Tbr2-Flp
CreER
RG
tTA
CreER
AAVPHP.eB-TRE3G-EGFP
AAVPHP.eB-CAG-FLEX-tdTomato
FezF2TC;Tbr2Flp
ETd
ETi
Nissl
C
AAV9-TRE-EGFP
AAV9-CAG-FLEX-tdTomato
FezF2TCTbr2Flp
RFO + BAR + VIS
24%
76%
C1
ETd
ETi
RFO
ETd
ETi
C2
BAR
ETd
ETi
C3
VIS
ETd
ETi
RFO
ETi
ETd
*
0
200
400
600
800
Number of neurons
BAR
ETi
ETd
*
0
200
400
600
800
1000
Number of neurons
VIS
ETi
ETd
n.s
0
200
400
600
Number of neurons

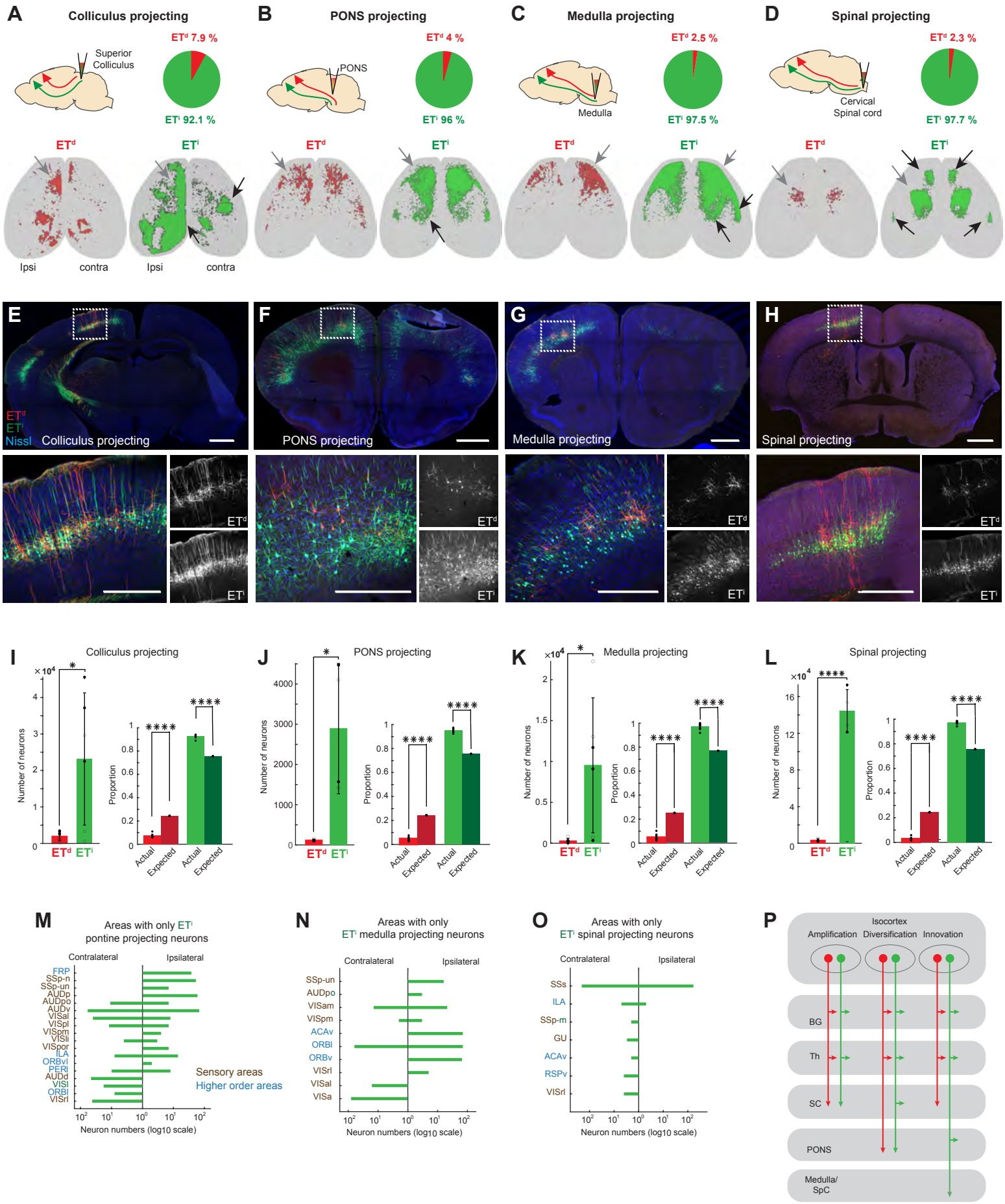
A
Colliculus projecting
Superior Colliculus
ETd 7.9 %
ETi 92.1 %
B
PONS projecting
PONS
ETd 4 %
ETi 96 %
C
Medulla projecting
Medulla
ETd 2.5 %
ETi 97.5 %
D
Spinal projecting
Cervical Spinal cord
ETd 2.3 %
ETi 97.7 %
ETd
ETi
Ipsi
contra
E
F
G
H
Nissl
Colliculus projecting
PONS projecting
Medulla projecting
Spinal projecting
I
Colliculus projecting
J
PONS projecting
K
Medulla projecting
L
Spinal projecting
Number of neurons
Proportion
Actual
Expected
M
Areas with only ETi pontine projecting neurons
Contralateral
Ipsilateral
FRP
SSp-n
SSp-un
AUDp
AUDpo
AUDv
VISal
VISpl
VISpm
VISli
VISpor
ILA
ORBvl
PERI
AUDd
VISl
ORBl
VISrl
Sensory areas
Higher order areas
Neuron numbers (log10 scale)
N
Areas with only ETi medulla projecting neurons
SSp-un
AUDpo
VISam
VISpm
ACAv
ORBl
ORBv
VISrl
VISal
VISa
O
Areas with only ETi spinal projecting neurons
SSs
ILA
SSp-m
GU
ACAv
RSPv
VISrl
P
Isocortex
Amplification
Diversification
Innovation
BG
Th
SC
PONS
Medulla/ SpC

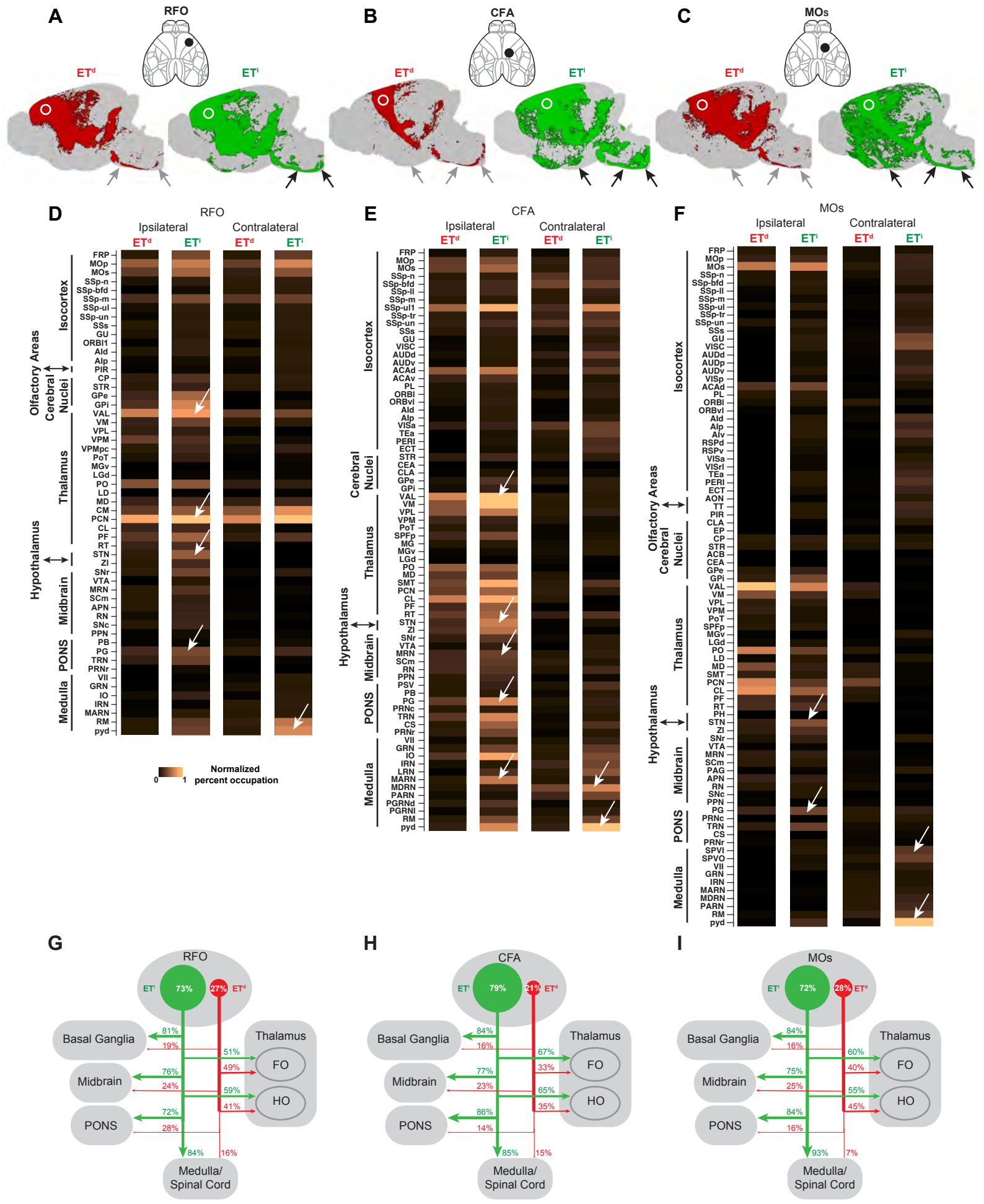
A
RFO
ET^d
ET^i
B
CFA
ET^d
ET^i
C
MOs
ET^d
ET^i
D
RFO
Ipsilateral
Contralateral
ET^d
ET^i
ET^d
ET^i
Olfactory Areas
Cerebral Nuclei
Hypothalamus
Isocortex
Thalamus
Midbrain
PONS
Medulla
FRP
MOp
MOs
SSp-n
SSp-bfd
SSp-m
SSp-ul
SSp-un
SSs
GU
ORBl1
Ald
Alp
PIR
CP
STR
GPe
GPi
VAL
VM
VPL
VPM
VPMpc
PoT
MGv
LGd
PO
LD
MD
CM
PCN
CL
PF
RT
STN
ZI
SNr
VTA
MRN
SCm
APN
RN
SNc
PPN
PB
PG
TRN
PRNr
VII
GRN
IO
IRN
MARN
RM
pyd
Normalized
percent occupation
0
1
E
CFA
Ipsilateral
Contralateral
ET^d
ET^i
ET^d
ET^i
Isocortex
Cerebral Nuclei
Thalamus
Hypothalamus
Midbrain
PONS
Medulla
FRP
MOp
MOs
SSp-n
SSp-bfd
SSp-ll
SSp-m
SSp-ul1
SSp-tr
SSp-un
SSs
GU
VISC
AUDd
AUDv
ACAd
ACAv
PL
ORBl
ORBvl
Ald
Alp
VISa
TEa
PERI
ECT
STR
CEA
CLA
GPe
GPi
VAL
VM
VPL
VPM
PoT
SPFp
MG
MGv
LGd
PO
MD
SMT
PCN
CL
PF
RT
STN
ZI
SNr
VTA
MRN
SCm
RN
PPN
PSV
PB
PG
PRNc
TRN
CS
PRNr
VII
GRN
IO
IRN
LRN
MARN
MDRN
PARN
PGRNd
PGRNl
RM
pyd
F
MOs
Ipsilateral
Contralateral
ET^d
ET^i
ET^d
ET^i
Isocortex
Olfactory Areas
Cerebral Nuclei
Thalamus
Hypothalamus
Midbrain
PONS
Medulla
FRP
MOp
MOs
SSp-n
SSp-bfd
SSp-ll
SSp-m
SSp-ul
SSp-tr
SSp-un
SSs
GU
VISC
AUDd
AUDp
AUDv
VISp
ACAd
PL
ORBl
ORBvl
Ald
Alp
Alv
RSPd
RSPv
VISa
VISrl
TEa
PERI
ECT
AON
TT
PIR
CLA
EP
CP
STR
ACB
CEA
GPe
GPi
VAL
VM
VPL
VPM
PoT
SPFp
MGv
LGd
PO
LD
MD
SMT
PCN
CL
PF
RT
PH
STN
ZI
SNr
VTA
MRN
SCm
PAG
APN
RN
SNc
PPN
PG
PRNc
TRN
CS
PRNr
SPVI
SPVO
VII
GRN
IRN
MARN
MDRN
PARN
RM
pyd
G
RFO
ET^i
73%
27%
ET^d
Basal Ganglia
81%
19%
Thalamus
51%
49%
FO
Midbrain
76%
24%
59%
41%
HO
PONS
72%
28%
84%
16%
Medulla/
Spinal Cord
H
CFA
ET^i
79%
21%
ET^d
Basal Ganglia
84%
16%
Thalamus
67%
33%
FO
Midbrain
77%
23%
65%
35%
HO
PONS
86%
14%
85%
15%
Medulla/
Spinal Cord
I
MOs
ET^i
72%
28%
ET^d
Basal Ganglia
84%
16%
Thalamus
60%
40%
FO
Midbrain
75%
25%
55%
45%
HO
PONS
84%
16%
93%
7%
Medulla/
Spinal Cord

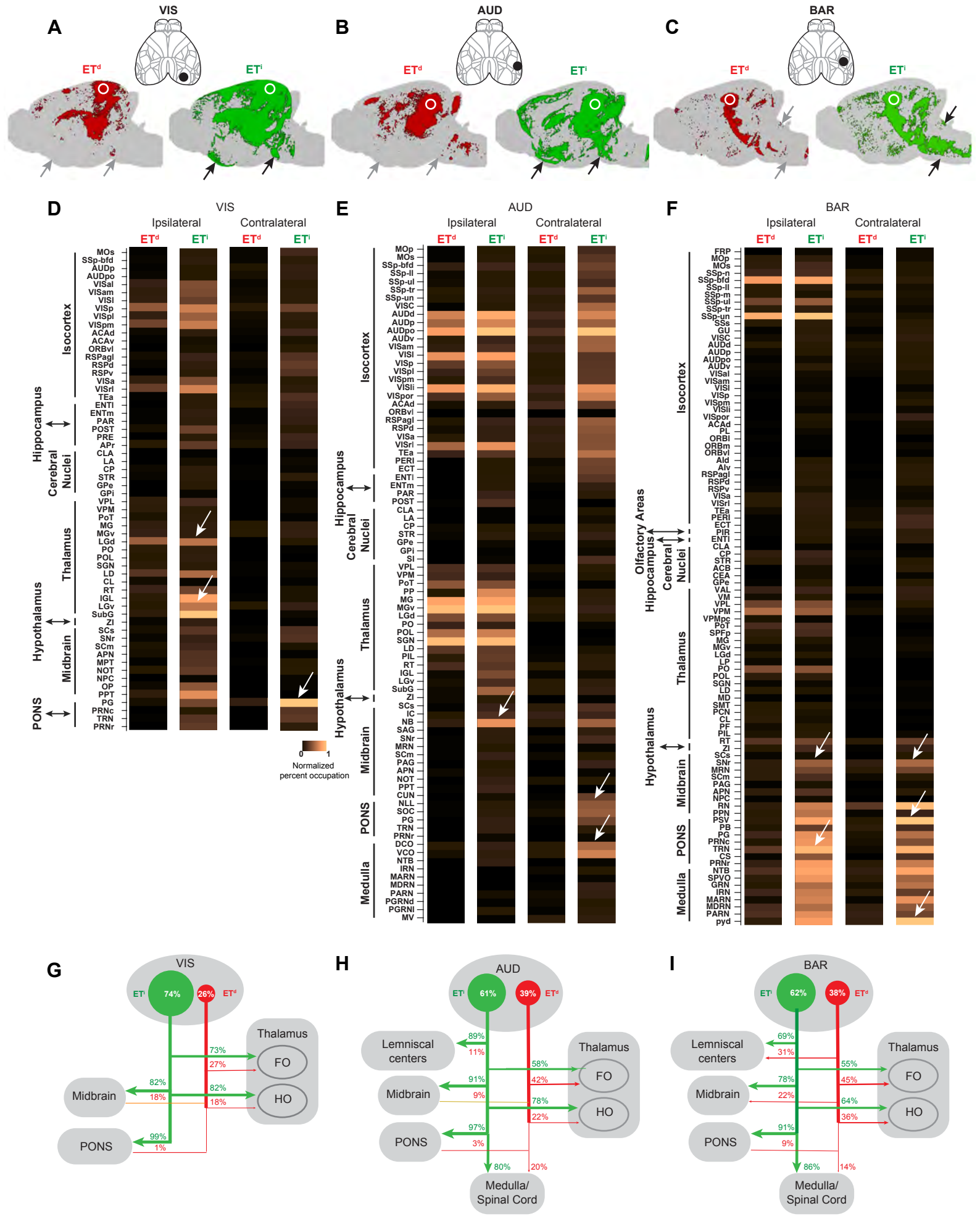
A
VIS
ETd
ETi
B
AUD
ETd
ETi
C
BAR
ETd
ETi
D
VIS
Ipsilateral
Contralateral
ETd
ETi
ETd
ETi
Isocortex
Hippocampus
Cerebral Nuclei
Thalamus
Hypothalamus
Midbrain
PONS
MOs
SSp-bfd
AUDp
AUDpo
VISal
VISam
VISl
VISp
VISpl
VISpm
ACAd
ACAv
ORBvl
RSPagl
RSPd
RSPv
VISa
VISrl
TEa
ENTl
ENTm
PAR
POST
PRE
APr
CLA
LA
CP
STR
GPe
GPi
VPL
VPM
PoT
MG
MGv
LGd
PO
POL
SGN
LD
CL
RT
IGL
LGv
SubG
ZI
SCs
SNr
SCm
APN
MPT
NOT
NPC
OP
PPT
PG
PRNc
TRN
PRNr
0
1
Normalized percent occupation
E
AUD
Ipsilateral
Contralateral
ETd
ETi
ETd
ETi
Isocortex
Hippocampus
Cerebral Nuclei
Thalamus
Hypothalamus
Midbrain
PONS
Medulla
MOp
MOs
SSp-bfd
SSp-ll
SSp-ul
SSp-tr
SSp-un
VISC
AUDd
AUDp
AUDpo
AUDv
VISam
VISl
VISp
VISpl
VISpm
VISli
VISpor
ACAd
ORBvl
RSPagl
RSPd
VISa
VISrl
TEa
PERI
ECT
ENTl
ENTm
PAR
POST
CLA
LA
CP
STR
GPe
GPi
SI
VPL
VPM
PoT
PP
MG
MGv
LGd
PO
POL
SGN
LD
PIL
RT
IGL
LGv
SubG
ZI
SCs
IC
NB
SAG
SNr
MRN
SCm
PAG
APN
NOT
PPT
CUN
NLL
SOC
PG
TRN
PRNr
DCO
VCO
NTB
IRN
MARN
MDRN
PARN
PGRNd
PGRNl
MV
F
BAR
Ipsilateral
Contralateral
ETd
ETi
ETd
ETi
Olfactory Areas
Hippocampus
Cerebral Nuclei
Thalamus
Hypothalamus
Midbrain
PONS
Medulla
FRP
MOp
MOs
SSp-n
SSp-bfd
SSp-ll
SSp-m
SSp-ul
SSp-tr
SSp-un
SSs
GU
VISC
AUDd
AUDp
AUDpo
AUDv
VISal
VISam
VISl
VISp
VISpm
VISli
VISpor
ACAd
PL
ORBl
ORBm
ORBvl
AId
AIv
RSPagl
RSPd
RSPv
VISa
VISrl
TEa
PERI
ECT
PIR
ENTl
CLA
CP
STR
ACB
CEA
GPe
VAL
VM
VPL
VPM
VPMpc
PoT
SPFp
MG
MGv
LGd
LP
PO
POL
SGN
LD
MD
SMT
PCN
CL
PF
PIL
RT
ZI
SCs
SNr
MRN
SCm
PAG
APN
NPC
RN
PPN
PSV
PB
PG
PRNc
TRN
CS
PRNr
NTB
SPVO
GRN
IRN
MARN
MDRN
PARN
pyd
G
VIS
ETi
74%
26%
ETd
Thalamus
FO
HO
Midbrain
PONS
73%
27%
82%
18%
82%
18%
99%
1%
H
AUD
ETi
61%
39%
ETd
Lemniscal centers
Thalamus
FO
HO
Midbrain
PONS
Medulla/ Spinal Cord
89%
11%
58%
42%
91%
9%
78%
22%
97%
3%
80%
20%
I
BAR
ETi
62%
38%
ETd
Lemniscal centers
Thalamus
FO
HO
Midbrain
PONS
Medulla/ Spinal Cord
69%
31%
55%
45%
78%
22%
64%
36%
91%
9%
86%
14%

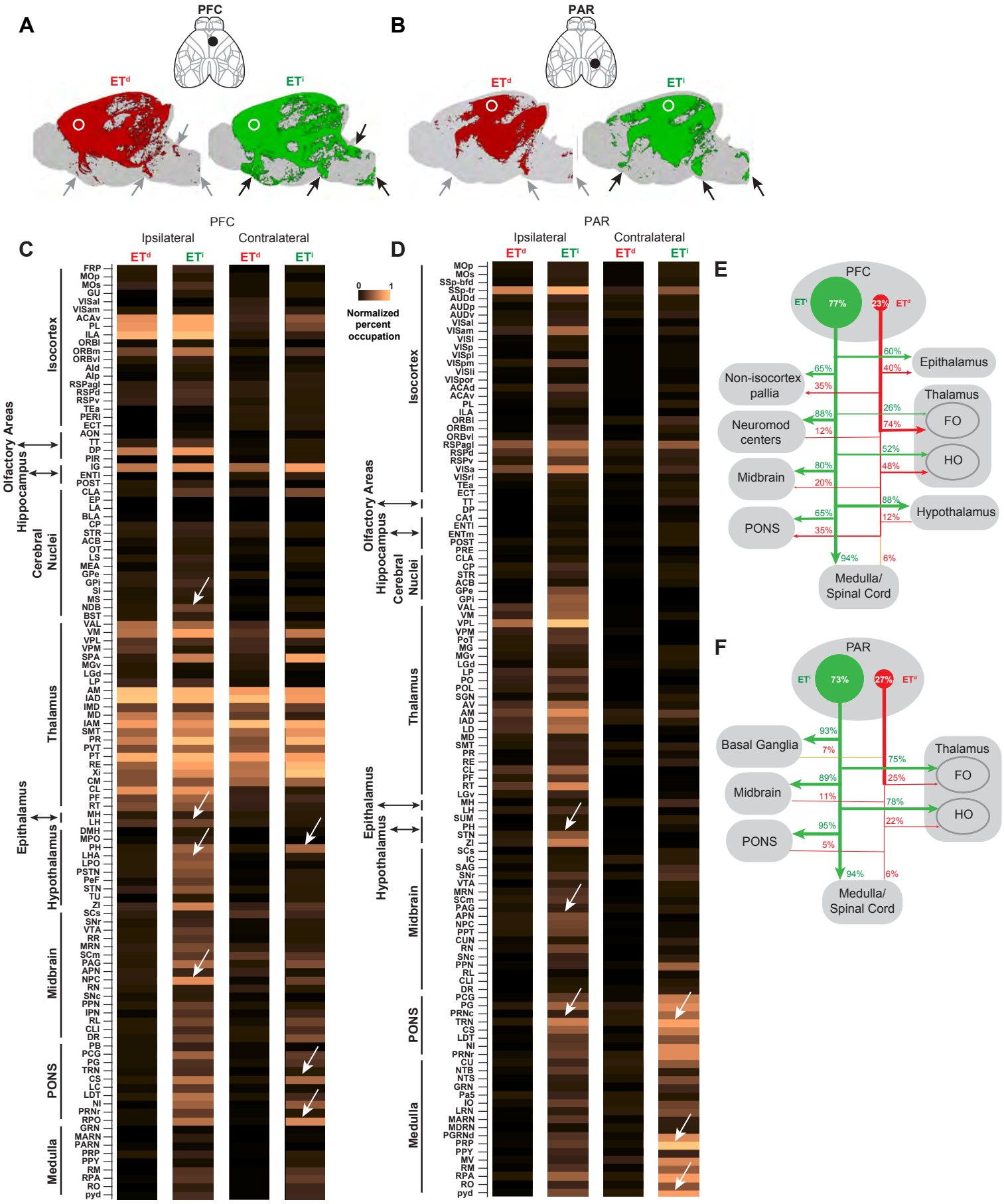
A
PFC
ETd
ETi
B
PAR
ETd
ETi
C
PFC
Ipsilateral
Contralateral
ETd
ETi
ETd
ETi
Olfactory Areas
Hippocampus
Cerebral Nuclei
Isocortex
Thalamus
Epithalamus
Hypothalamus
Midbrain
PONS
Medulla
FRP
MOp
MOs
GU
VISal
VISam
ACAv
PL
ILA
ORBl
ORBm
ORBvl
AId
AIp
RSPagl
RSPd
RSPv
TEa
PERI
ECT
AON
TT
DP
PIR
IG
ENTl
POST
CLA
EP
LA
BLA
CP
STR
ACB
OT
LS
MEA
GPe
GPi
SI
MS
NDB
BST
VAL
VM
VPL
VPM
SPA
MGv
LGd
LP
AM
IAD
IMD
MD
IAM
SMT
PR
PVT
PT
RE
Xi
CM
CL
PF
RT
MH
LH
DMH
MPO
PH
LHA
LPO
PSTN
PeF
STN
TU
ZI
SCs
SNr
VTA
RR
MRN
SCm
PAG
APN
NPC
RN
SNc
PPN
IPN
RL
CLI
DR
PB
PCG
PG
TRN
CS
LC
LDT
NI
PRNr
RPO
GRN
MARN
PARN
PRP
PPY
RM
RPA
RO
pyd
0
1
Normalized percent occupation
D
PAR
Ipsilateral
Contralateral
ETd
ETi
ETd
ETi
Olfactory Areas
Hippocampus
Cerebral Nuclei
Isocortex
Thalamus
Epithalamus
Hypothalamus
Midbrain
PONS
Medulla
MOp
MOs
SSp-bfd
SSp-tr
AUDd
AUDp
AUDv
VISal
VISam
VISl
VISp
VISpl
VISpm
VISli
VISpor
ACAd
ACAv
PL
ILA
ORBl
ORBm
ORBvl
RSPagl
RSPd
RSPv
VISa
VISrl
TEa
ECT
TT
DP
CA1
ENTl
ENTm
POST
PRE
CLA
CP
STR
ACB
GPe
GPi
VAL
VM
VPL
VPM
PoT
MG
MGv
LGd
LP
PO
POL
SGN
AV
AM
IAD
LD
MD
SMT
PR
RE
CL
PF
RT
LGv
MH
LH
SUM
PH
STN
ZI
SCs
IC
SAG
SNr
VTA
MRN
SCm
PAG
APN
NPC
PPT
CUN
RN
SNc
PPN
RL
CLI
DR
PCG
PG
PRNc
TRN
CS
LDT
NI
PRNr
CU
NTB
NTS
GRN
Pa5
IO
LRN
MARN
MDRN
PGRNd
PRP
PPY
MV
RM
RPA
RO
pyd
E
PFC
ETi
77%
23%
ETd
60%
40%
Epithalamus
Non-isocortex pallia
65%
35%
Thalamus
26%
74%
FO
Neuromod centers
88%
12%
52%
48%
HO
Midbrain
80%
20%
88%
12%
Hypothalamus
PONS
65%
35%
94%
6%
Medulla/ Spinal Cord
F
PAR
ETi
73%
27%
ETd
93%
7%
Basal Ganglia
Thalamus
75%
25%
FO
Midbrain
89%
11%
78%
22%
HO
PONS
95%
5%
94%
6%
Medulla/ Spinal Cord

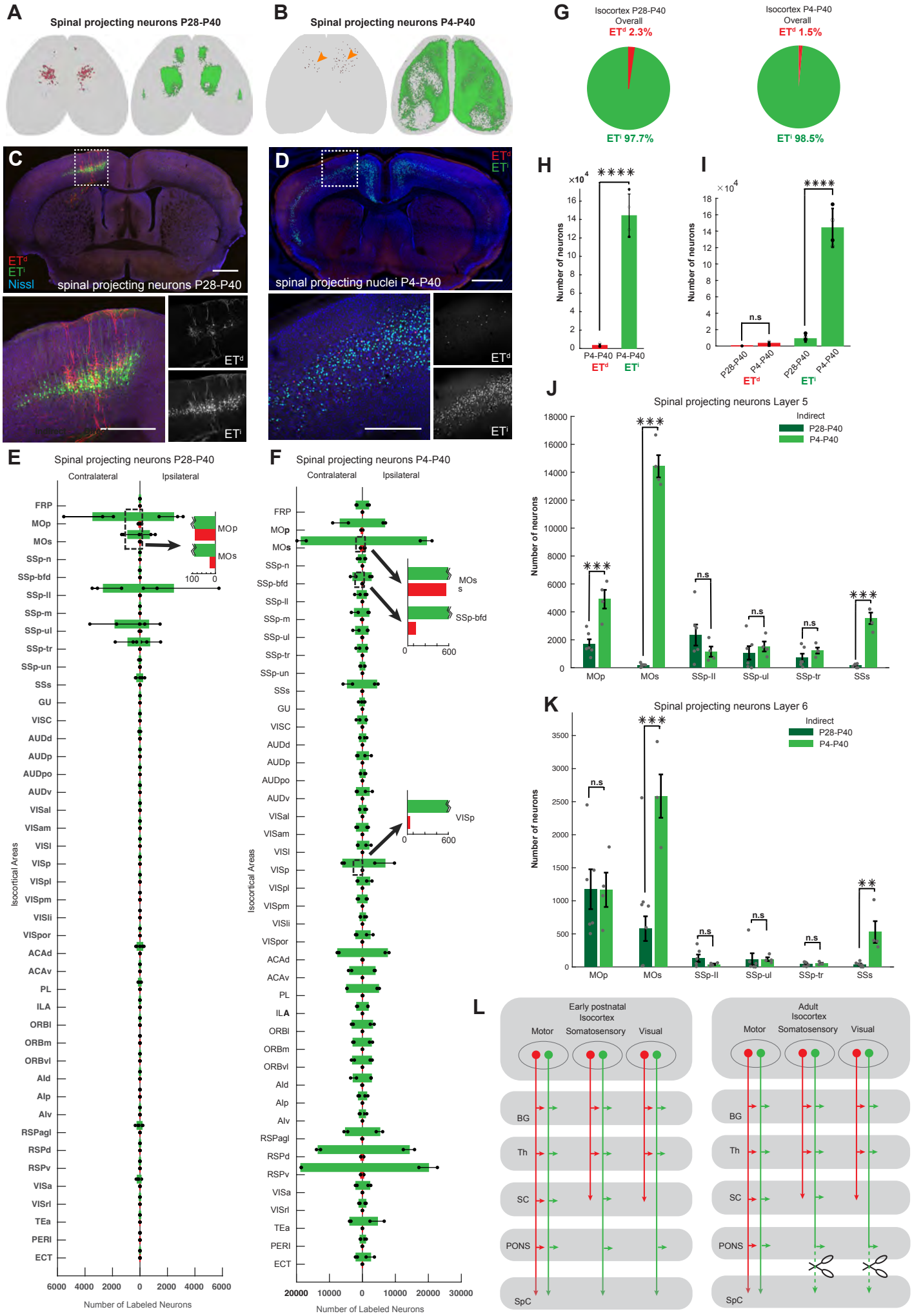
A
Spinal projecting neurons P28-P40
B
Spinal projecting neurons P4-P40
G
Isocortex P28-P40
Overall
ETd 2.3%
ETi 97.7%
Isocortex P4-P40
Overall
ETd 1.5%
ETi 98.5%
C
ETd
ETi
Nissl
spinal projecting neurons P28-P40
D
ETd
ETi
spinal projecting nuclei P4-P40
H
Number of neurons
P4-P40 P4-P40
ETd ETi
I
Number of neurons
n.s
P28-P40 P4-P40 P28-P40 P4-P40
ETd ETi
J
Spinal projecting neurons Layer 5
Indirect
P28-P40
P4-P40
Number of neurons
MOp MOs SSp-ll SSp-ul SSp-tr SSs
E
Spinal projecting neurons P28-P40
Contralateral
Ipsilateral
Isocortical Areas
Number of Labeled Neurons
F
Spinal projecting neurons P4-P40
Contralateral
Ipsilateral
Isocortical Areas
Number of Labeled Neurons
K
Spinal projecting neurons Layer 6
Indirect
P28-P40
P4-P40
Number of neurons
MOp MOs SSp-ll SSp-ul SSp-tr SSs
L
Early postnatal
Isocortex
Motor
Somatosensory
Visual
BG
Th
SC
PONS
SpC
Adult
Isocortex
Motor
Somatosensory
Visual
BG
Th
SC
PONS
SpC

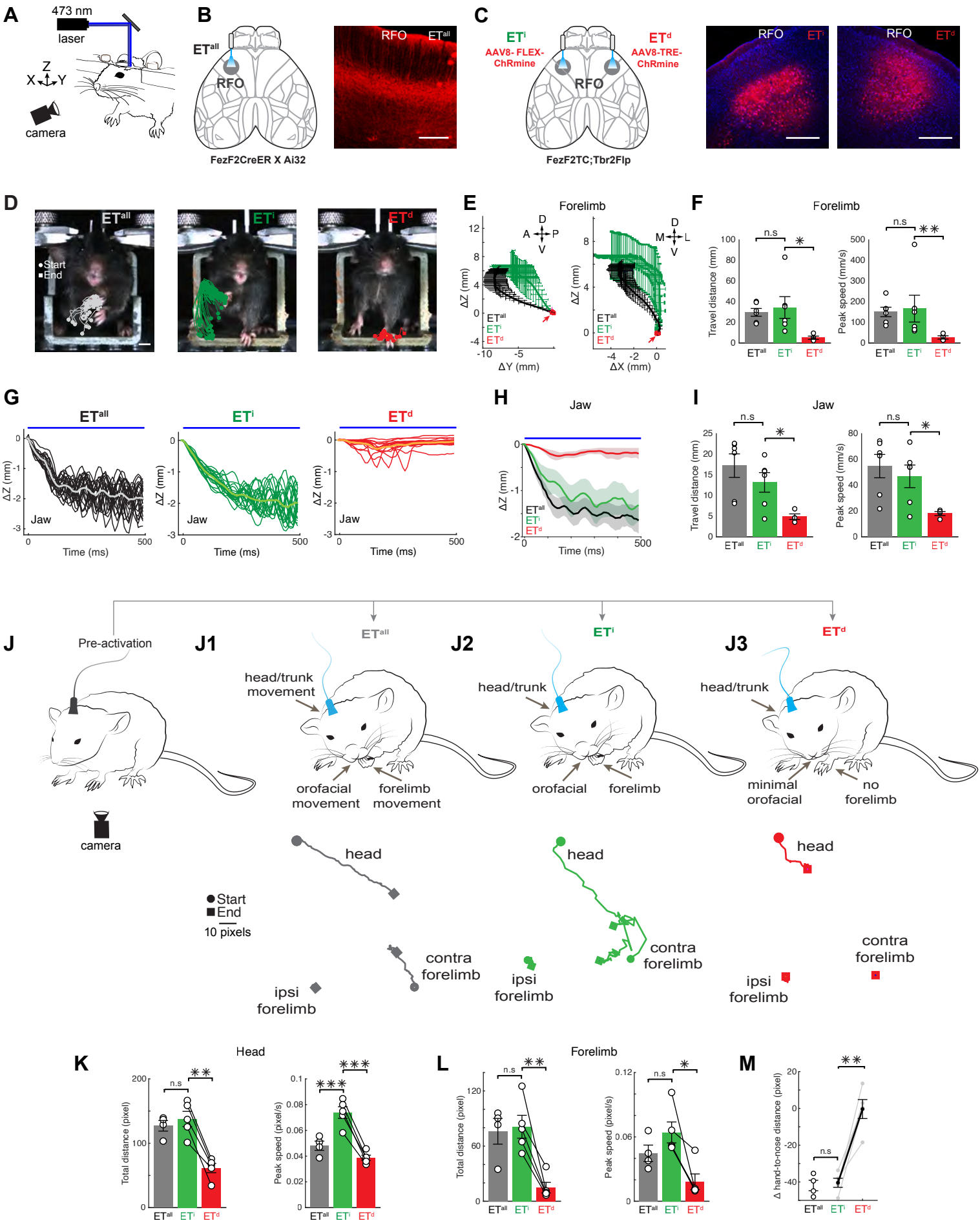
A
473 nm
laser
camera
B
ETall
RFO
FezF2CreER X Ai32
RFO ETall
C
ETi
AAV8- FLEX-ChRmine
ETd
AAV8-TRE-ChRmine
RFO
FezF2TC;Tbr2Flp
RFO ETi
RFO ETd
D
ETall
ETi
ETd
Start
End
E
Forelimb
ΔZ (mm)
ΔY (mm)
ΔX (mm)
F
Forelimb
Travel distance (mm)
Peak speed (mm/s)
n.s
G
ETall
ETi
ETd
Jaw
Time (ms)
H
Jaw
I
Jaw
J
Pre-activation
camera
J1
head/trunk movement
orofacial movement
forelimb movement
J2
head/trunk
orofacial
forelimb
J3
head/trunk
minimal orofacial
no forelimb
head
contra forelimb
ipsi forelimb
Start
End
10 pixels
K
Head
Total distance (pixel)
Peak speed (pixel/s)
L
Forelimb
M
Δ hand-to-nose distance (pixel)

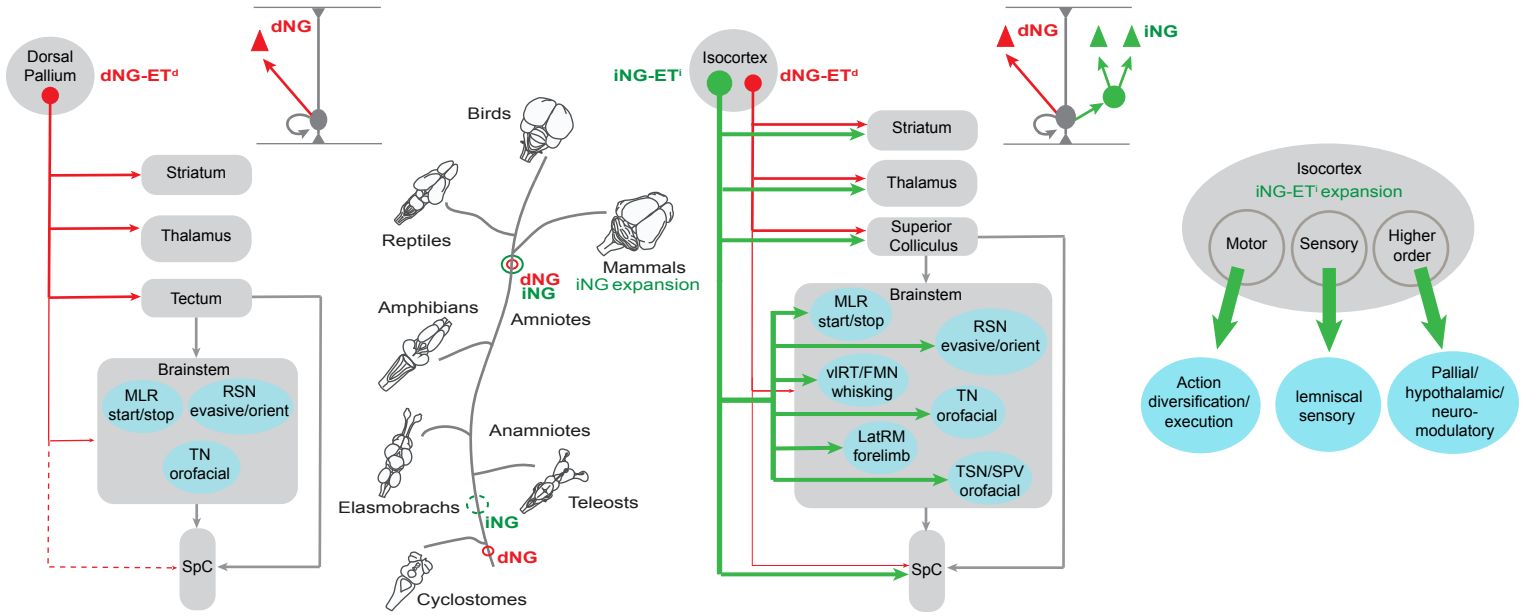
Dorsal Pallium
dNG-ET^d
dNG
Striatum
Thalamus
Tectum
Brainstem
MLR start/stop
RSN evasive/orient
TN orofacial
SpC
Birds
Reptiles
Mammals
iNG expansion
dNG
iNG
Amphibians
Amniotes
Anamniotes
Elasmobrachs
iNG
Teleosts
dNG
Cyclostomes
Isocortex
iNG-ET^l
dNG-ET^d
Striatum
Thalamus
Superior Colliculus
Brainstem
MLR start/stop
RSN evasive/orient
vIRT/FMN whisking
TN orofacial
LatRM forelimb
TSN/SPV orofacial
SpC
dNG
iNG
Isocortex
iNG-ET^l expansion
Motor
Sensory
Higher order
Action diversification/ execution
lemniscal sensory
Pallial/ hypothalamic/ neuro-modulatory

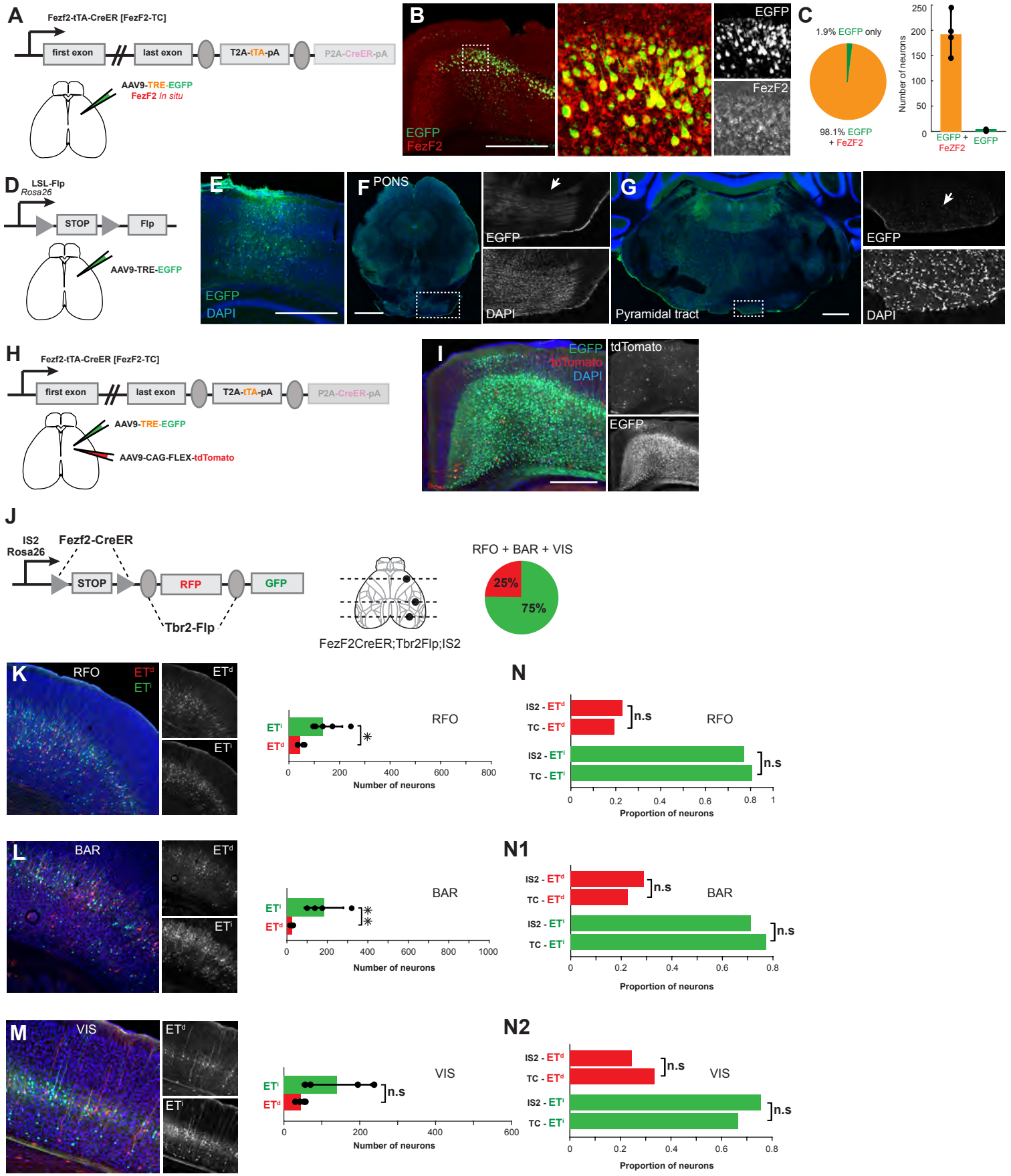
A
Fezf2-tTA-CreER [FezF2-TC]
first exon
last exon
T2A-tTA-pA
P2A-CreER-pA
AAV9-TRE-EGFP
FezF2 In situ
B
EGFP
FezF2
C
1.9% EGFP only
98.1% EGFP + FezF2
Number of neurons
EGFP + FezF2
EGFP
D
LSL-Flp
Rosa26
STOP
Flp
AAV9-TRE-EGFP
E
EGFP
DAPI
F
PONS
G
Pyramidal tract
H
AAV9-CAG-FLEX-tdTomato
I
tdTomato
J
IS2
Rosa26
Fezf2-CreER
RFP
GFP
Tbr2-Flp
FezF2CreER;Tbr2Flp;IS2
RFO + BAR + VIS
25%
75%
K
RFO
ETd
ETi
Number of neurons
Proportion of neurons
n.s
N
L
BAR
N1
M
VIS
N2
IS2 - ETd
TC - ETd
IS2 - ETi
TC - ETi

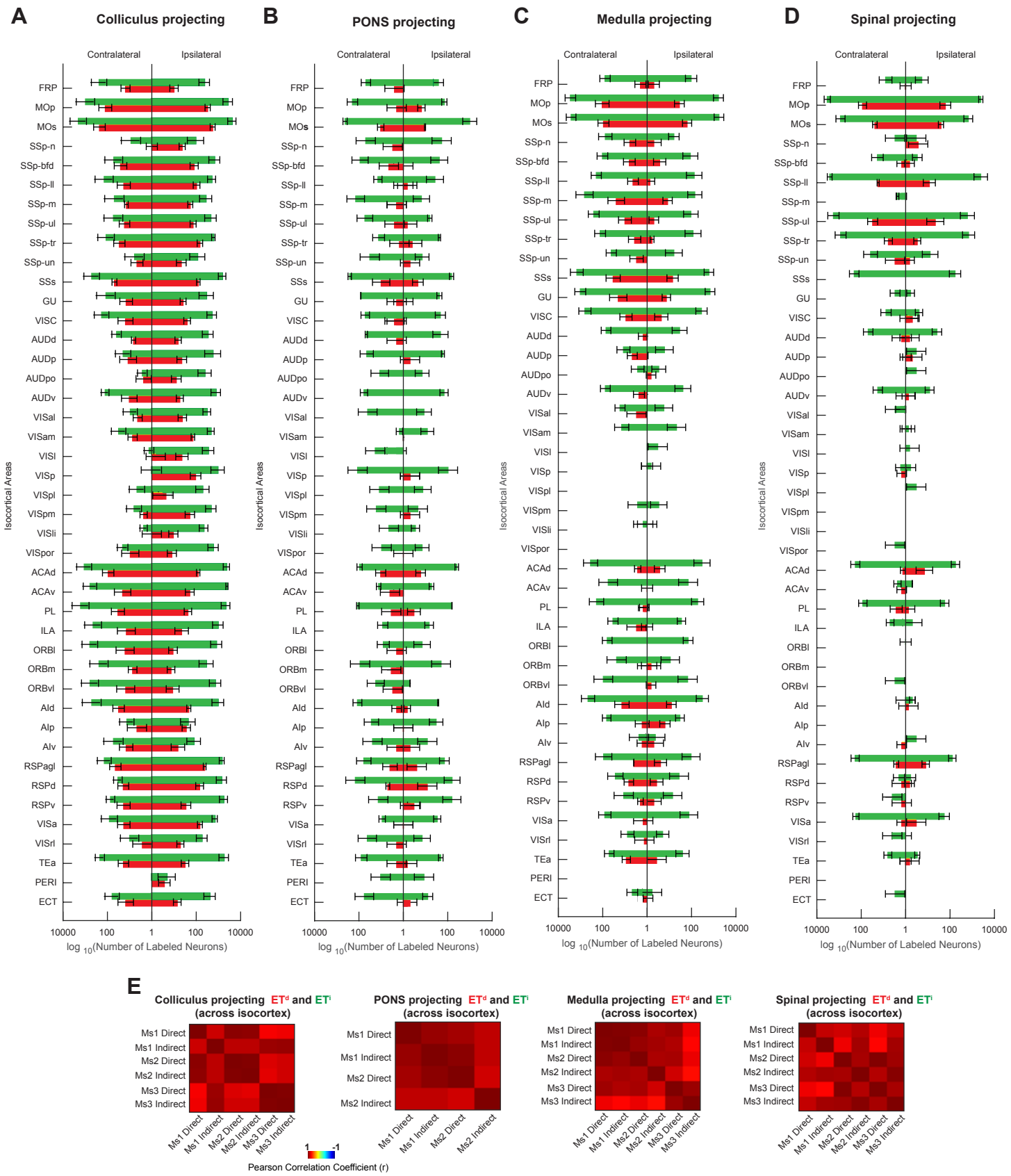
A
Colliculus projecting
B
PONS projecting
C
Medulla projecting
D
Spinal projecting
Contralateral
Ipsilateral
Isocortical Areas
FRP
MOp
MOs
SSp-n
SSp-bfd
SSp-ll
SSp-m
SSp-ul
SSp-tr
SSp-un
SSs
GU
VISC
AUDd
AUDp
AUDpo
AUDv
VISal
VISam
VISl
VISp
VISpl
VISpm
VISli
VISpor
ACAd
ACAv
PL
ILA
ORBl
ORBm
ORBvl
AId
AIp
AIv
RSPagl
RSPd
RSPv
VISa
VISrl
TEa
PERI
ECT
10000
100
1
100
10000
log 10(Number of Labeled Neurons)
E
Colliculus projecting ETd and ETi
(across isocortex)
PONS projecting ETd and ETi
(across isocortex)
Medulla projecting ETd and ETi
(across isocortex)
Spinal projecting ETd and ETi
(across isocortex)
Ms1 Direct
Ms1 Indirect
Ms2 Direct
Ms2 Indirect
Ms3 Direct
Ms3 Indirect
1
-1
Pearson Correlation Coefficient (r)

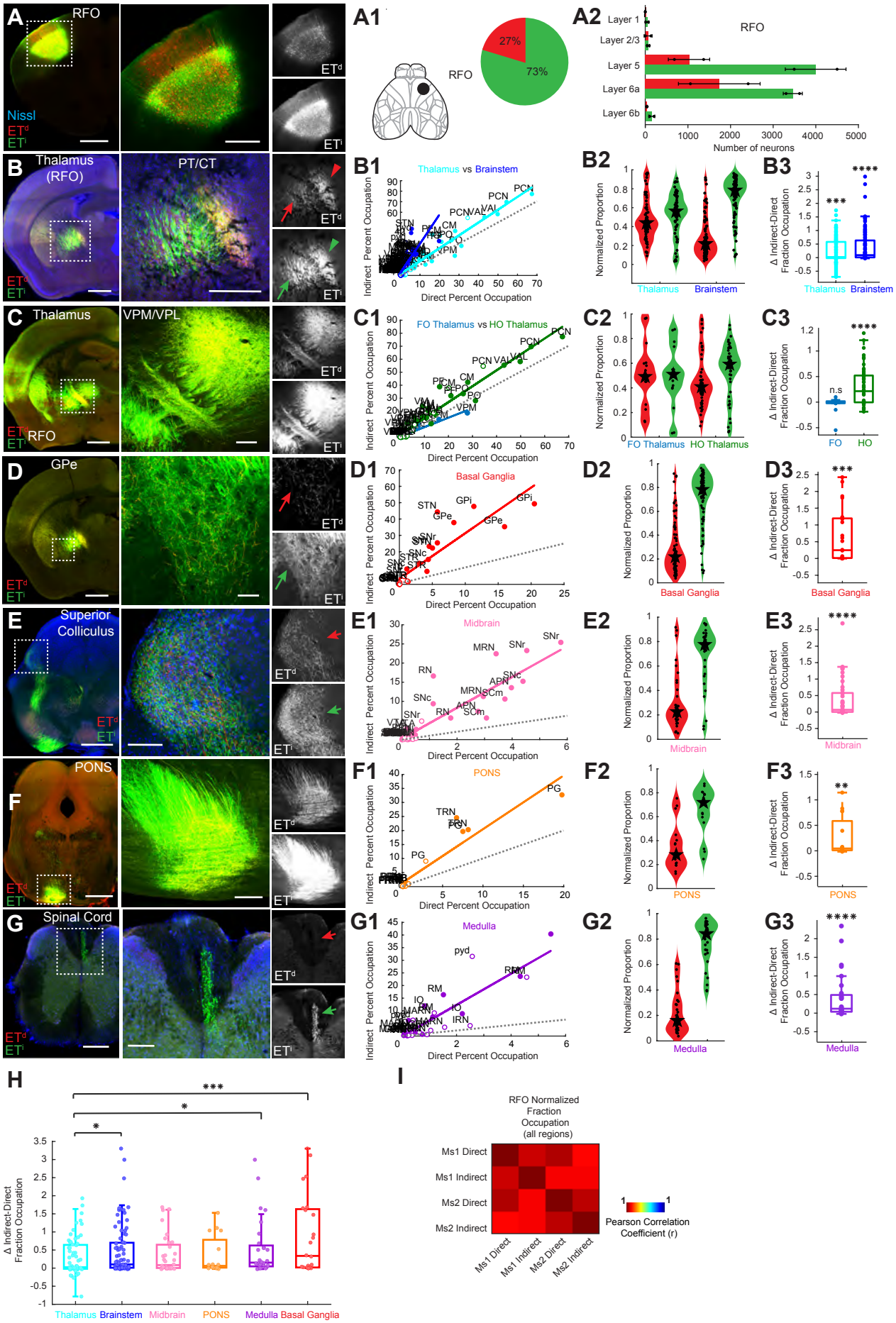
A
RFO
Nissl
ETd
ETi
B
Thalamus (RFO)
PT/CT
C
Thalamus
VPM/VPL
RFO
D
GPe
E
Superior Colliculus
F
PONS
G
Spinal Cord
A1
RFO
27%
73%
A2
RFO
Layer 1
Layer 2/3
Layer 5
Layer 6a
Layer 6b
Number of neurons
B1
Thalamus vs Brainstem
Indirect Percent Occupation
Direct Percent Occupation
B2
Normalized Proportion
Thalamus
Brainstem
B3
Δ Indirect-Direct Fraction Occupation
C1
FO Thalamus vs HO Thalamus
C2
FO Thalamus
HO Thalamus
C3
n.s
FO
HO
D1
Basal Ganglia
D2
D3
E1
Midbrain
E2
E3
F1
PONS
F2
F3
G1
Medulla
G2
G3
H
Thalamus
Brainstem
Midbrain
PONS
Medulla
Basal Ganglia
I
RFO Normalized Fraction Occupation (all regions)
Ms1 Direct
Ms1 Indirect
Ms2 Direct
Ms2 Indirect
Pearson Correlation Coefficient (r)

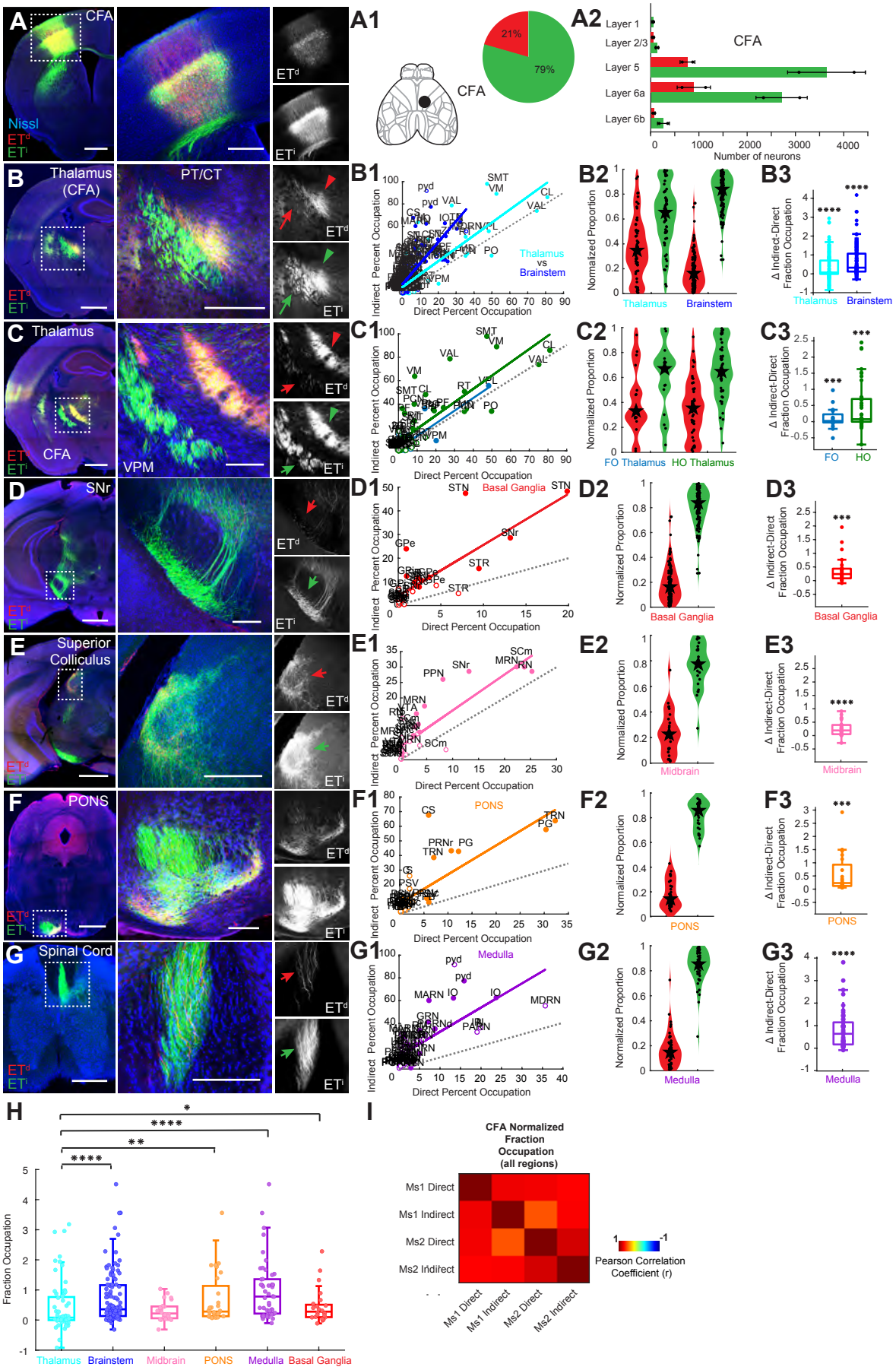
A
CFA
Nissl
ETd
ETi
A1
21%
79%
CFA
A2
Layer 1
Layer 2/3
Layer 5
Layer 6a
Layer 6b
CFA
Number of neurons
B
Thalamus (CFA)
PT/CT
B1
Thalamus vs Brainstem
Percent Occupation
Direct Percent Occupation
B2
Normalized Proportion
Thalamus
Brainstem
B3
Δ Indirect-Direct Fraction Occupation
C
Thalamus
CFA
VPM
C1
C2
FO Thalamus
HO Thalamus
C3
FO
HO
D
SNr
D1
Basal Ganglia
D2
D3
E
Superior Colliculus
E1
E2
Midbrain
E3
F
PONS
F1
F2
F3
G
Spinal Cord
G1
Medulla
G2
G3
H
Thalamus
Brainstem
Midbrain
PONS
Medulla
Basal Ganglia
I
CFA Normalized Fraction Occupation (all regions)
Ms1 Direct
Ms1 Indirect
Ms2 Direct
Ms2 Indirect
Pearson Correlation Coefficient (r)

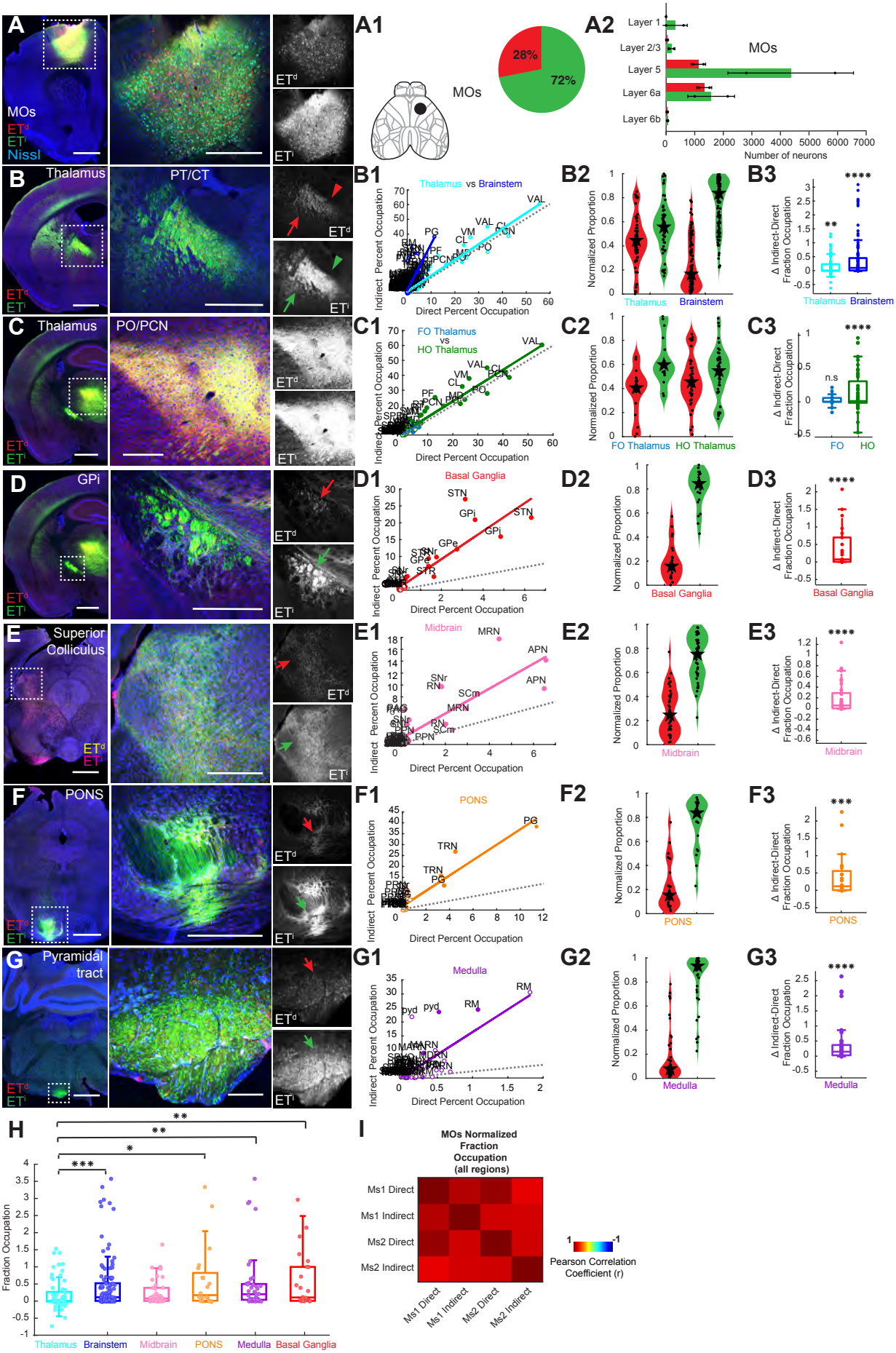
A
MOs
ETd
ETi
Nissl
A1
MOs
28%
72%
A2
MOs
Layer 1
Layer 2/3
Layer 5
Layer 6a
Layer 6b
Number of neurons
B
Thalamus
PT/CT
B1
Thalamus vs Brainstem
Direct Percent Occupation
Indirect Percent Occupation
B2
Normalized Proportion
Thalamus
Brainstem
B3
Δ Indirect-Direct Fraction Occupation
C
Thalamus
PO/PCN
C1
FO Thalamus vs HO Thalamus
C2
FO Thalamus
HO Thalamus
C3
n.s
FO
HO
D
GPi
D1
Basal Ganglia
D2
D3
E
Superior Colliculus
E1
Midbrain
E2
E3
F
PONS
F1
F2
F3
G
Pyramidal tract
G1
Medulla
G2
G3
H
Thalamus
Brainstem
Midbrain
PONS
Medulla
Basal Ganglia
I
MOs Normalized Fraction Occupation (all regions)
Ms1 Direct
Ms1 Indirect
Ms2 Direct
Ms2 Indirect
Pearson Correlation Coefficient (r)

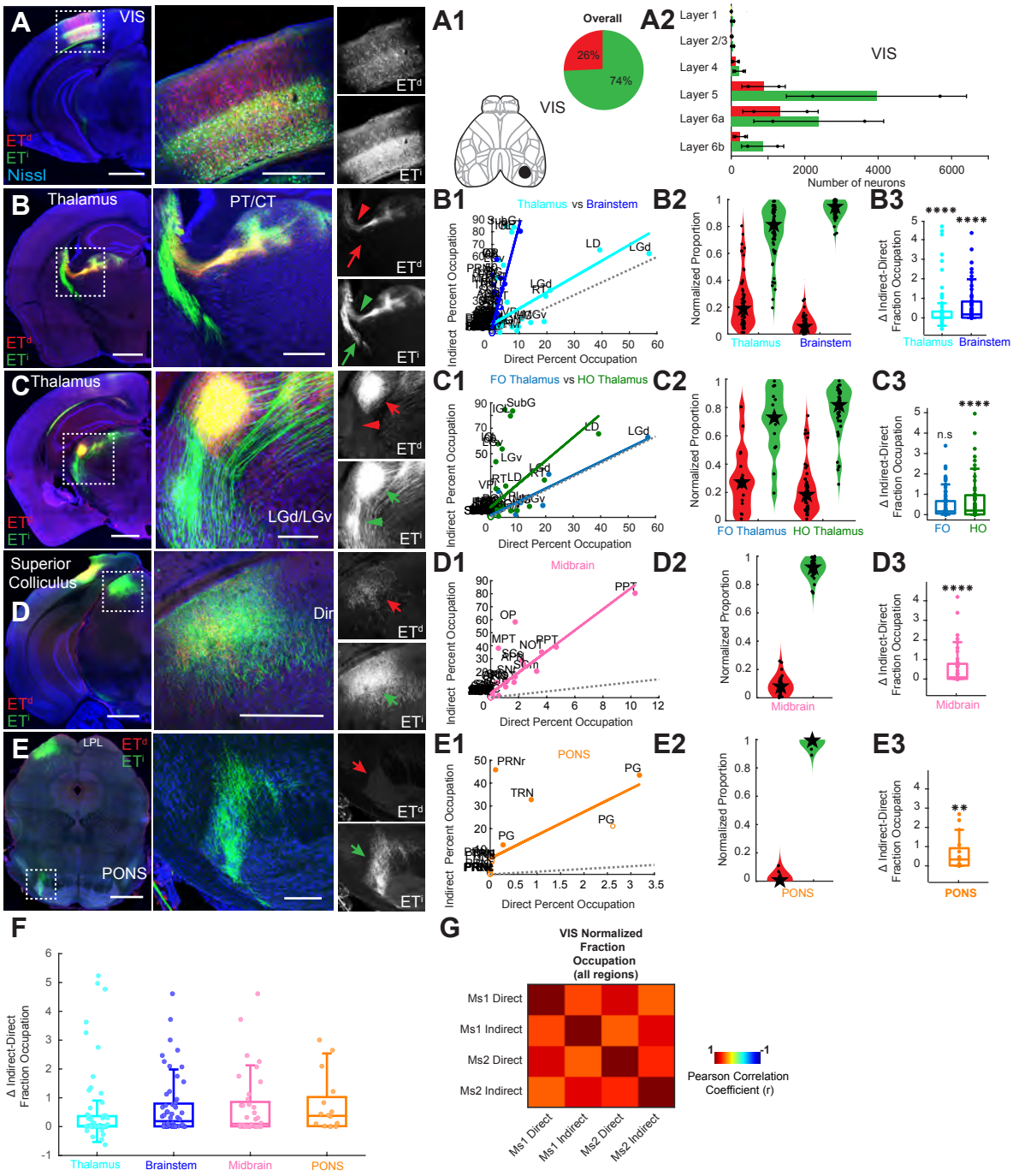
A
VIS
ETd
ETi
Nissl
B
Thalamus
PT/CT
C
Thalamus
LGd/LGv
Superior Colliculus
D
Dir
E
LPL
PONS
A1
Overall
26%
74%
VIS
A2
Layer 1
Layer 2/3
Layer 4
Layer 5
Layer 6a
Layer 6b
Number of neurons
B1
Thalamus vs Brainstem
Percent Occupation
Direct Percent Occupation
B2
Normalized Proportion
Thalamus
Brainstem
B3
Δ Indirect-Direct Fraction Occupation
C1
FO Thalamus vs HO Thalamus
C2
FO Thalamus
HO Thalamus
C3
n.s
FO
HO
D1
Midbrain
D2
D3
E1
PONS
E2
E3
F
Thalamus
Brainstem
Midbrain
PONS
G
VIS Normalized Fraction Occupation (all regions)
Ms1 Direct
Ms1 Indirect
Ms2 Direct
Ms2 Indirect
Pearson Correlation Coefficient (r)

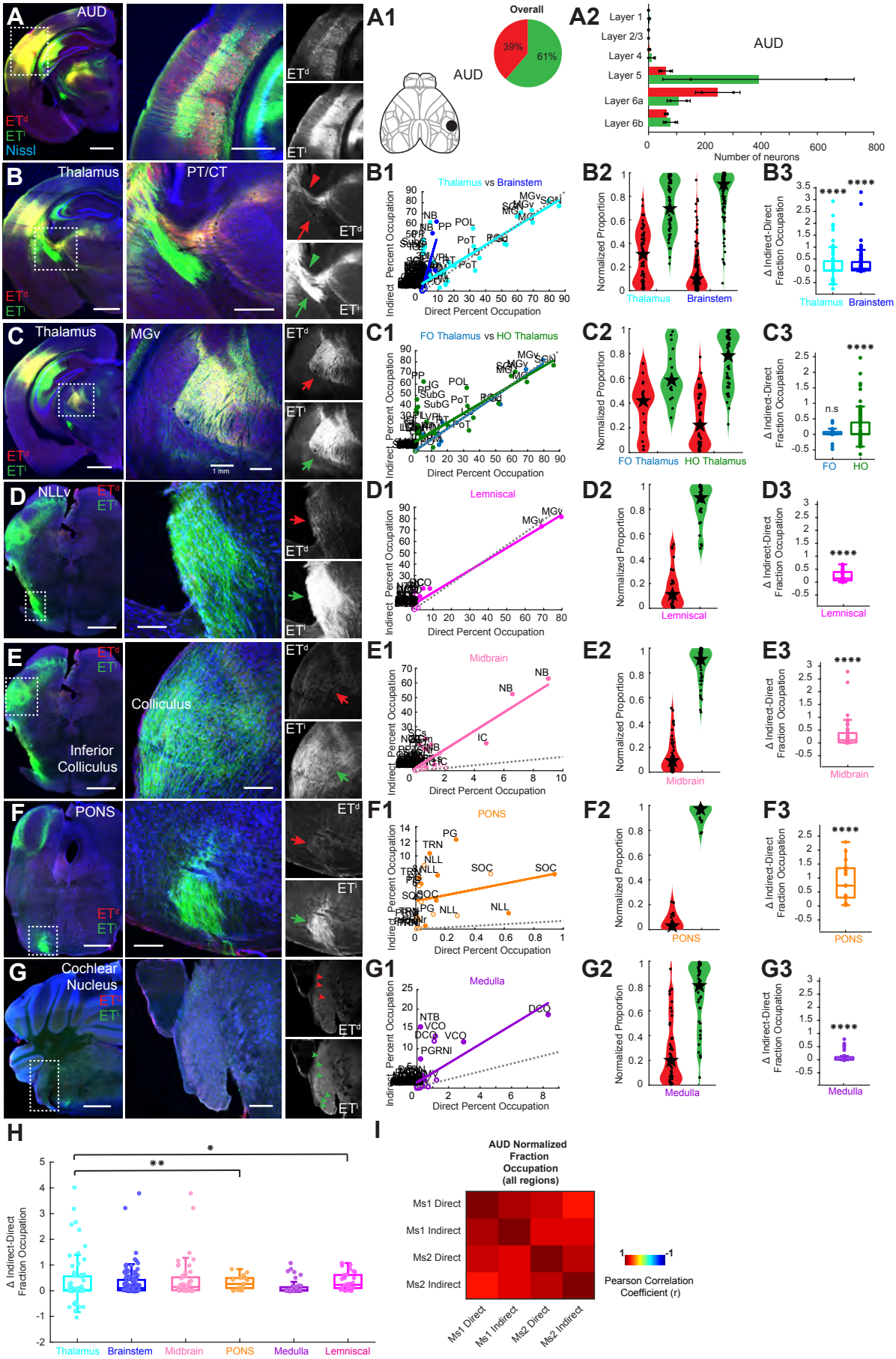
A
AUD
ETd
ETi
Nissl
A1
Overall
39%
61%
AUD
A2
Layer 1
Layer 2/3
Layer 4
Layer 5
Layer 6a
Layer 6b
AUD
Number of neurons
B
Thalamus
PT/CT
B1
Thalamus vs Brainstem
Indirect Percent Occupation
Direct Percent Occupation
B2
Normalized Proportion
Thalamus
Brainstem
B3
Δ Indirect-Direct Fraction Occupation
****
****
Thalamus
Brainstem
C
Thalamus
MGv
1 mm
C1
FO Thalamus vs HO Thalamus
C2
FO Thalamus
HO Thalamus
C3
n.s
****
FO
HO
D
NLLv
D1
Lemniscal
D2
Lemniscal
D3
****
Lemniscal
E
Colliculus
Inferior Colliculus
E1
Midbrain
E2
Midbrain
E3
****
Midbrain
F
PONS
F1
PONS
F2
PONS
F3
****
PONS
G
Cochlear Nucleus
G1
Medulla
G2
Medulla
G3
****
Medulla
H
*
**
Δ Indirect-Direct Fraction Occupation
Thalamus
Brainstem
Midbrain
PONS
Medulla
Lemniscal
I
AUD Normalized Fraction Occupation (all regions)
Ms1 Direct
Ms1 Indirect
Ms2 Direct
Ms2 Indirect
Pearson Correlation Coefficient (r)

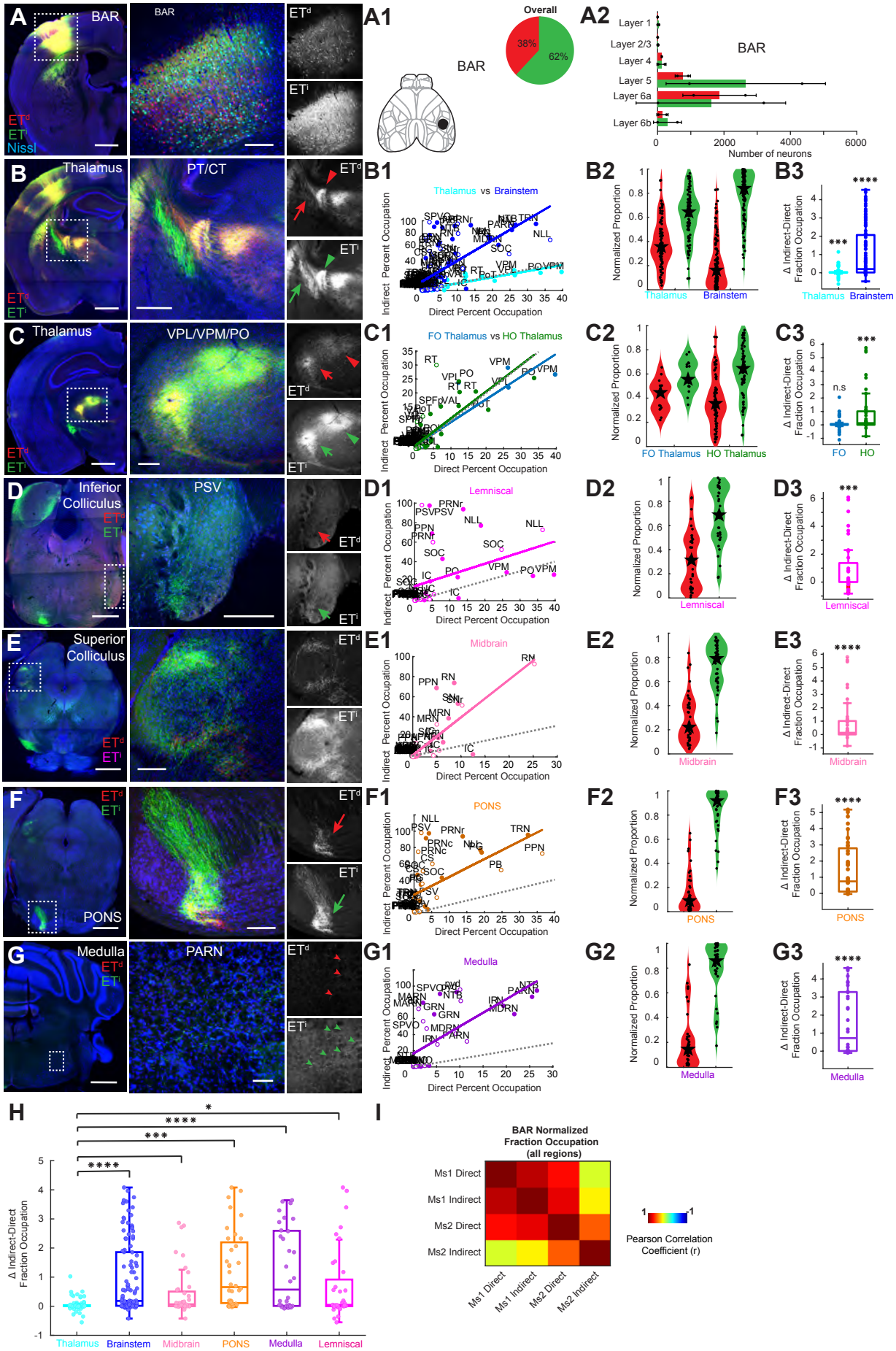
A
BAR
ETd
ETi
Nissl
A1
Overall
38%
62%
BAR
A2
Layer 1
Layer 2/3
Layer 4
Layer 5
Layer 6a
Layer 6b
Number of neurons
B
Thalamus
PT/CT
B1
Thalamus vs Brainstem
Percent Occupation
Direct Percent Occupation
B2
Normalized Proportion
Thalamus
Brainstem
B3
Δ Indirect-Direct Fraction Occupation
C
VPL/VPM/PO
C1
FO Thalamus vs HO Thalamus
C2
FO Thalamus
HO Thalamus
C3
n.s
FO
HO
D
Inferior Colliculus
PSV
D1
Lemniscal
D2
D3
E
Superior Colliculus
E1
Midbrain
E2
E3
F
PONS
F1
F2
F3
G
Medulla
PARN
G1
G2
G3
H
Thalamus
Brainstem
Midbrain
PONS
Medulla
Lemniscal
I
BAR Normalized Fraction Occupation (all regions)
Ms1 Direct
Ms1 Indirect
Ms2 Direct
Ms2 Indirect
Pearson Correlation Coefficient (r)

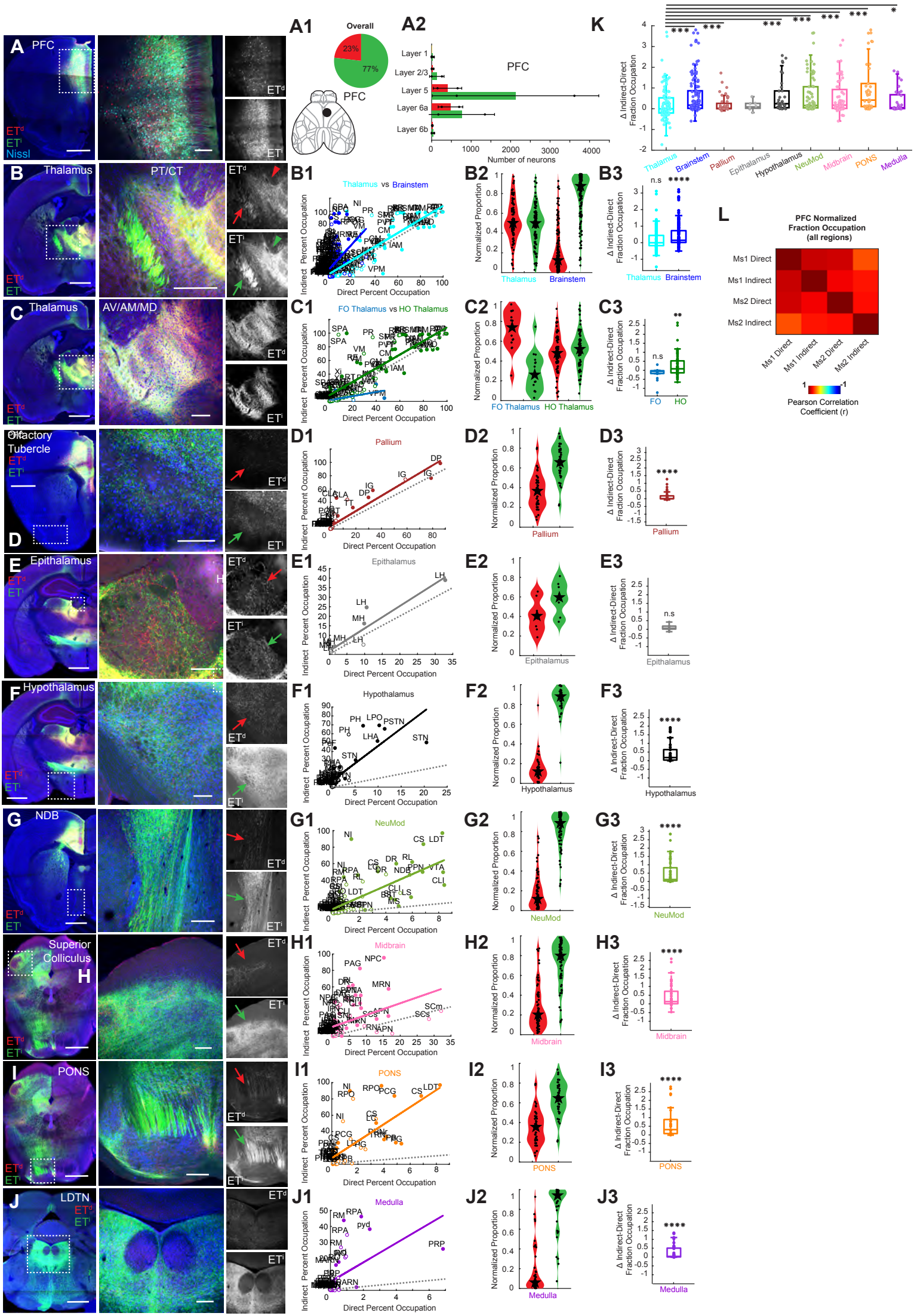
A PFC
ET^d
ET^i
Nissl
B Thalamus
PT/CT
C Thalamus
AV/AM/MD
D Olfactory Tubercle
E Epithalamus
F Hypothalamus
G NDB
H Superior Colliculus
I PONS
J LDTN
A1
Overall
23%
77%
PFC
A2
Layer 1
Layer 2/3
Layer 5
Layer 6a
Layer 6b
Number of neurons
K
Δ Indirect-Direct Fraction Occupation
Thalamus
Brainstem
Pallium
Epithalamus
Hypothalamus
NeuMod
Midbrain
PONS
Medulla
B1
Thalamus vs Brainstem
Percent Occupation
Indirect
Direct Percent Occupation
B2
Normalized Proportion
B3
n.s
C1
FO Thalamus vs HO Thalamus
C2
C3
FO
HO
D1
Pallium
D2
D3
E1
E2
E3
F1
F2
F3
G1
G2
G3
H1
H2
H3
I1
I2
I3
J1
J2
J3
L
PFC Normalized Fraction Occupation (all regions)
Ms1 Direct
Ms1 Indirect
Ms2 Direct
Ms2 Indirect
Pearson Correlation Coefficient (r)

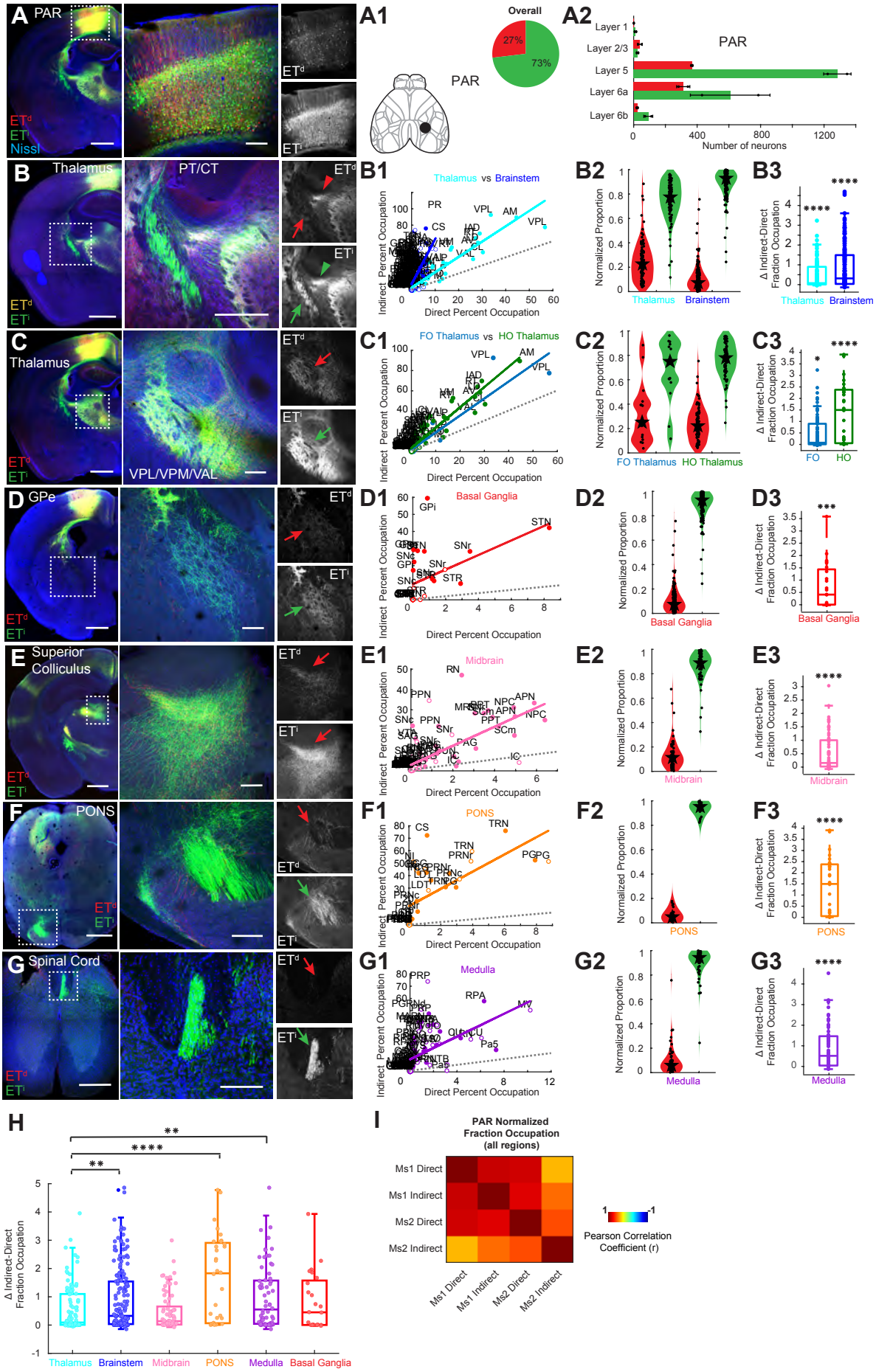
A PAR
ETd
ETi
Nissl
A1
Overall
27%
73%
PAR
A2
Layer 1
Layer 2/3
Layer 5
Layer 6a
Layer 6b
PAR
Number of neurons
B Thalamus
PT/CT
B1
Thalamus vs Brainstem
Indirect Percent Occupation
Direct Percent Occupation
B2
Normalized Proportion
Thalamus
Brainstem
B3
Δ Indirect-Direct Fraction Occupation
C Thalamus
VPL/VPM/VAL
C1
FO Thalamus vs HO Thalamus
C2
FO Thalamus
HO Thalamus
C3
FO
HO
D GPe
D1
Basal Ganglia
D2
Basal Ganglia
D3
E Superior Colliculus
E1
Midbrain
E2
Midbrain
E3
F PONS
F1
PONS
F2
PONS
F3
G Spinal Cord
G1
Medulla
G2
Medulla
G3
H
Δ Indirect-Direct Fraction Occupation
Thalamus
Brainstem
Midbrain
PONS
Medulla
Basal Ganglia
I
PAR Normalized Fraction Occupation (all regions)
Ms1 Direct
Ms1 Indirect
Ms2 Direct
Ms2 Indirect
Pearson Correlation Coefficient (r)

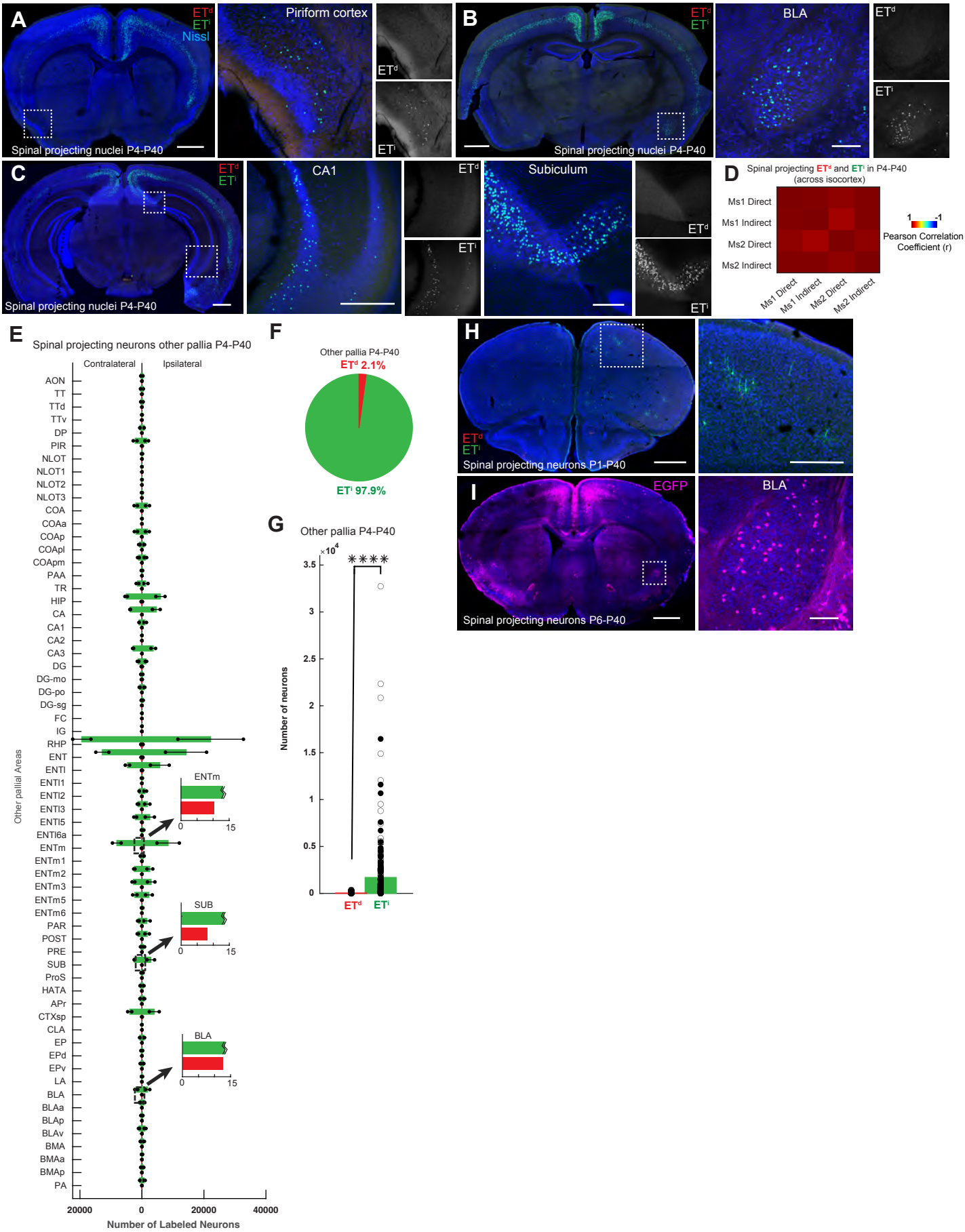
A
ETd
ETi
Nissl
Spinal projecting nuclei P4-P40
Piriform cortex
ETd
ETi
B
ETd
ETi
Spinal projecting nuclei P4-P40
BLA
ETd
ETi
C
ETd
ETi
Spinal projecting nuclei P4-P40
CA1
ETd
ETi
Subiculum
ETd
ETi
D
Spinal projecting ETd and ETi in P4-P40
(across isocortex)
Ms1 Direct
Ms1 Indirect
Ms2 Direct
Ms2 Indirect
1
-1
Pearson Correlation
Coefficient (r)
E
Spinal projecting neurons other pallia P4-P40
Contralateral
Ipsilateral
Other pallial Areas
AON
TT
TTd
TTv
DP
PIR
NLOT
NLOT1
NLOT2
NLOT3
COA
COAa
COAp
COApl
COApm
PAA
TR
HIP
CA
CA1
CA2
CA3
DG
DG-mo
DG-po
DG-sg
FC
IG
RHP
ENT
ENTl
ENTl1
ENTl2
ENTl3
ENTl5
ENTl6a
ENTm
ENTm1
ENTm2
ENTm3
ENTm5
ENTm6
PAR
POST
PRE
SUB
ProS
HATA
APr
CTXsp
CLA
EP
EPd
EPv
LA
BLA
BLAa
BLAp
BLAv
BMA
BMAa
BMAp
PA
ENTm
0
15
SUB
0
15
BLA
0
15
20000
0
20000
40000
Number of Labeled Neurons
F
Other pallia P4-P40
ETd 2.1%
ETi 97.9%
G
Other pallia P4-P40
×10^4
3.5
3
2.5
2
1.5
1
0.5
0
Number of neurons
****
ETd
ETi
H
ETd
ETi
Spinal projecting neurons P1-P40
I
EGFP
Spinal projecting neurons P6-P40
BLA